The dissertation committee for Young-Keun Park
Certifies that this is the approved version of the following dissertation:

Hybrid Particle-Finite Element Simulation of Large Deformation Dynamics in Composite Materials

Committee:

Eric P. Fahrenthold, Supervisor

Jeffrey K. Bennighof

Michael D. Bryant

Raul G. Longoria

Alfred E. Traver

Hybrid Particle-Finite Element Simulation of Large Deformation Dynamics in Composite Materials

by

Young-Keun Park, B.S., M.S.

Dissertation

Presented to the Faculty of the Graduate School of

The University of Texas at Austin

in Partial Fulfillment

of the Requirements

for the Degree of

DOCTOR OF PHILOSOPHY

The University of Texas at Austin

December 2004

To Parents and Wife.

Acknowledgments

Firstly, I want to give all the glory to God for the bless, wisdom, courage, and faith bestowed on me to achieve the fruit of this endeavor.

I would like to give my deepest thanks to my supervisor Dr. Eric P. Fahrenthold for his financial support, guidance, and encouragement throughout the study. None of the study would have been possible without his invaluable help and prudent advice. I also want to express my gratitude to the members of my dissertation committee, Dr. Jeffrey K. Bennighof, Dr. Michael D. Bryant, Dr. Raul G. Longoria, Dr. Alfred E. Traver for their advice and suggestions.

I also specially would like to give thanks to my parents, Bumho Park and Okyoung Lee, and my wife, Sungsoo Lee, who offered incessant love, support and encouragement. To them, I dedicate this thesis.

I want to thank all my colleagues and friends in Mechanical Engineering Korean Student Association (MEKSA). I'll never forget many things that we did together like playing softball games and tennis, and having many parties. It was a memorable time for me.

Finally, I would like to thank NASA Johnson Space Center (NAG 9-1244), the National Science Foundation (CMS 99-12475), the State of Texas Advanced Research Program (project number 003658-0709-1999), and Lockheed Martin Aeronautics Company for the research support and the NASA Ames Research Center, the Texas Advanced Computing Center at the University of Texas at Austin, and the Artic Region Supercomputing Center at the University of Alaska Fairbanks for their computer time support.

Young-Keun Park

The University of Texas at Austin

December 2004

Hybrid Particle-Finite Element Simulation of Large Deformation Dynamics in Composite Materials

Publication No. ____________________

Young-Keun Park, Ph.D.
The University of Texas at Austin, 2004

Supervisor: Eric P. Fahrenthold

Space structures such as satellites and the space shuttle are subject to severe damage, due to the impact of space debris and micrometeoroids. In order to prevent such damage, it is necessary to develop advanced spacecraft shield designs. Composite materials and multi-layer geometry shields play an important role in the design of spacecraft protection systems. Adequate material models and efficient numerical methods are needed to simulate hypervelocity impact phenomena in such systems. Recent research has employed numerical simulations to study hypervelocity impact phenomena, because of the high cost of advanced shielding materials, the limitations of experimental capabilities, and recent improvements in numerical methods and computing power. This research has developed an improved hybrid particle-finite element method and new composite material models for the simulation of hypervelocity impact on space structures. An anisotropic rate dependent material model has been developed to model composites, in three dimensional hypervelocity impact applications. A kernel free hybrid particle-finite element method has been formulated, that eliminates the use of density interpolation kernels, simplifying the method and reducing the computational cost of the particle dependent calculations.

It has been validated in three dimensional simulations of hypervelocity impact on spacecraft thermal protection materials.

Contents

List of Tables

List of Figures

Chapter 1

Introduction

1.1 Introduction

Many impact phenomena are of engineering interest, such as crash of a car, impact of a bullet against any target, and orbital debris impact on spacecrafts. Among those, orbital debris impact must be distinguished from the other impact phenomena due to the very high velocity of impact. Orbital debris impact, occurring at about 5-15 km/s is regarded as a hypervelocity impact (HVI). The number of orbital debris and micrometeoroid particles has been increasing in space continuously, and these debris threaten the safety of spacecraft. In order to protect spacecraft from orbital debris, new designs and new materials must be developed to provide better protection. Advanced orbital debris shield designs often incorporate a metal-composite multi-plate geometry.

Many researchers have studied HVI phenomena over the last several decades, both analytically and experimentally. The simulation of HVI effects on spacecraft shielding design is difficult, due both to their geometry and their material composition. In spite of these complications, simulation of the HVI response of multi-plate metal-composite debris shield is of strong engineering interest, due to the high cost of advanced shielding materials, the limitations of existing light gas guns, and improvements in computing power.

1.2 Motivation

Recent numerical methods research has been focused on the development of mixed particle-continuum methods that can handle problems difficult for traditional mesh based methods and meshless methods. The simulation of large deformation problems [71], including HVI, on the space shuttle or orbital debris shields is an example application demanding a mixed particle-continuum method.

In general, mesh based methods and meshless methods are commonly used for continuum dynamics problems [44]. Lagrangian mesh based methods have the advantage of solving finite deformation problems in solid mechanics. However severe mesh distortion and complex contact-impact modeling result in limitations for using this method in HVI analysis. Eulerian mesh based methods are most often used in the fluid mechanics area. The Eulerian method does not have the mesh distortion problem experienced in the Lagrangian codes, however difficulty in tracking material interfaces and system boundaries restricts the class of problems that Eulerian methods can handle. These reasons caused many researchers to consider meshless methods for HVI analysis. Most of the meshless methods make use of Smooth Particle Hydrodynamics (SPH) [78][72][63], which employs interpolation functions, although some alternative particle based methods have been proposed [9]. The SPH method has some advantages, such as no mesh distortion and the treatment of initiation and growth of cracks. However this method has some disadvantages, such as instability in tension, poor accuracy, difficult implementation of boundary conditions and ad hoc modeling procedures. Some efforts have been made to overcome these disadvantages [49][66][57][73]. Mixed methods combining the advantages of pure mesh based and meshless methods are needed, due to the aforementioned drawbacks of other methods. It appears that some mixed particle-continuum formulations are well adapted to model fragmentation and large deformations, necessary for HVI analysis [29]. A coupled SPH-finite element method [43] is the most widely accepted type of mixed particle-continuum approach. In this method, the particles and elements are not used simultaneously, which means particles are used for certain regions and elements are used for other regions of the structure. This method has problems in that it needs a special coupling algorithm (for example, a penalty based contact-impact algorithm) to couple SPH with FEM. To avoid this shortcoming, an alternative mixed particle-continuum formulation was developed by Fahrenthold and Horban [28][29]. Unlike the coupled method, it makes use of both elements and particles simultaneously, which distinguishes this method as a hybrid formulation. This hybrid particle-element method provides a capability to analyze HVI phenomena, where large strain plasticity, fragmentation, perforation, and multi-structure contact impact effects are often present. Particles model all inertia, contact-impact effect and thermomechanical response in compressed states, and elements model tension and elastic-plastic shear. Unlike the coupled SPH-finite element method, this method introduced a new kernel based density interpolation for compressed states, instead of using a penalty treatment of contact-impact effects. Fahrenthold and Horban's work [29] was later extended by Shivarama and Fahrenthold [74]. They developed an ellipsoidal particle model using a four parameter, non-singular representation of rotation based on Euler parameters. However difficulties in HVI simulation on multi-plate metal-composite debris shields encouraged development of more efficient numerical techniques.

Advanced composites are increasingly used in the aerospace, naval, and automobile industries, due to their superior mechanical and thermal properties. One important application in the aerospace industry is orbital debris shielding for spacecraft. The characteristics of those composites must be understood for use in a wide range of applications. Some examples of advanced shielding materials are Nextel, Kevlar, Graphite/epoxy, Al/epoxy, Graphite/PEEK(Poly Ether Ether Ketone) composite, Carbon fiber reinforced composite, and Reinforced Carbon-Carbon(RCC). Among those, a combination of Nextel and Kevlar has been used for the orbital debris shields deployed on the International Space Station (ISS), and RCC has been used as a thermal protection material on the wing leading edge of the space shuttle. Nextel and Kevlar are used for debris shield applications because Nextel is better at shocking projectile fragments than aluminum and Kevlar is better at slowing debris cloud expansion than aluminum. The reason for using RCC as a thermal protection material for the space shuttle is that RCC has superior mechanical and thermal properties, such as light weight, high thermal shock resistance, high strength and stiffness at high temperature, low thermal expansion, high thermal conductivity, and high fracture toughness. Although it is essential to model advanced composite materials used in spacecraft shielding, most numerical models consider only isotropic materials. Recent research [38][14] is aimed at the development of numerical models of composites, for use in space shuttle applications and orbital debris impact problems. More accurate material models must be developed to describe the characteristics of anisotropic materials.

1.3 Scope of the research

In the present work a hybrid particle finite element model [29][74] is used to simulate the impact of foam blocks on both ceramic tile and RCC components of the Space Shuttle thermal protection system, and the HVI response of aluminum-

Nextel-Kevlar debris shield deployed on the ISS. The formulation is based on energy concepts. This method avoids the stability problems of SPH techniques. It introduces both elements and particles in all material regions simultaneously. The particles model all inertia, contact-impact, and thermomechanical response in compressed states, while the elements model tension and elastic-plastic shear. Some of the simulations described here employed simple material models for the foam, tile, felt strain isolation pad (SIP), and RCC, with material properties estimated using the available experimental data. Later the HVI simulation of aluminum-Nextel-Kevlar debris shield employed a rate dependent material model developed for Kevlar and introduced nonlinear equations of state for Nextel and Kevlar, using a Mie-Gruneisen functional form.

An improved hybrid particle finite element formulation, extending the work of Shivarama and Fahrenthold [74] has been developed and validated in simulations of impact experiments. It was used for three dimensional simulations of HVI effects on RCC, with a rate dependent anisotropic material model developed for RCC. It eliminates the use of density interpolation kernels, simplifying the method and reducing the computational cost of the particle dependent calculations. The density distribution is obtained, not from a moving interpolation, but by the integration of density evolution equations. An additional advantage of this method is its simple, energy and momentum conserving accommodation of a time or orientation dependent particle contact distance.

1.4 Dissertation Organization

The remaining chapters of the dissertation are organized as follows.

Chapter 2 describes a series of three dimensional simulations using a hybrid particle-finite element method [74] and a parallel computer code [26] to model the impact of foam blocks on both ceramic tile and RCC components of the space shuttle thermal protection system.

Chapter 3 describes work on the numerical implementation of a rate dependent material model for Kevlar, and the conduct of several three dimensional simulations, performed to investigate the hypervelocity impact response of aluminum-Nextel-Kevlar debris shields like those deployed on the ISS. The simulations employed a hybrid-particle finite element method [74] and a parallel computer code [26] specifically developed to address the advanced orbital debris shielding design problem.

Chapter 4 describes an improved hybrid particle-finite element formulation, extending the work of Shivarama and Fahrenthold [74]. An alternative kernel free particle-element method has been developed, to reduce computational costs, avoid accuracy and stability problems associated with the selection of appropriate interpolation kernels (used in particle methods and mixed particle-element methods to compute the particle densities and to model particle contact-impact), and simply accommodate an orientation and time dependent contact distance.

Chapter 5 describes a series of simulations of HVI effects on RCC, using an improved hybrid particle-finite element method, including a rate dependent anisotropic material model newly developed for RCC. The material modeling work developed two specific components (a strain energy density in shear and a plasticity model) of the general numerical formulation. The material model was validated in simulations of hypervelocity impact experiments conducted at 7 km/s. Then a series of simulations was performed to estimate orbital debris impact effects at velocities beyond the range of current experimental methods.

Finally, Chapter 6 presents summary of the work completed and recommendations for future work.

Chapter 2

Simulation of Foam Impact Effects on Components of the Space Shuttle Thermal Protection System

2.1 Introduction

The report of the Columbia Accident Investigation Board [2] concluded that the effects of foam impact on the wing leading edge of the Space Shuttle were the most likely cause for the loss of the Orbiter Columbia. Strong evidence in support of this conclusion is provided by a recent series of impact experiments conducted at Southwest Research Institute (SwRI) by a NASA-SwRI-industry team [45]. The current consensus regarding the cause of the accident was not present in the early stages of the investigation, since little experimental data relevant to the accident conditions was available, and since significant lead times were required to prepare and conduct the necessary impact experiments.

Soon after the loss of Columbia an impact analysis team was assembled [77] whose purpose was to investigate analytically the effects of foam impact on components of the Space Shuttle thermal protection system, and to support the conduct of experiments designed to duplicate the impact events observed during launch of the vehicle. This group included NASA, industry, national laboratory, and university participation and employed a variety of numerical methods [20] and computer codes [36] to simulate the impact events of interest. The present work describes a series of three dimensional simulations performed using a hybrid particle-finite element method [29][74] and a parallel computer code [26] to model the impact of foam blocks on both ceramic tile and reinforced carbon-carbon (RCC) components of the Space Shuttle thermal protection system. The simulations described here were performed in advance of the aforementioned experiments and employed the best available material property data for foam, tile, and RCC. The conclusions suggested by the simulations are in general consistent with the results of later experiments, although additional material testing, material modeling, and simulation work is needed to develop a validated computational approach to impact damage assessment for future Space Shuttle applications.

The sections which follow describe the numerical method used in the simulations, the structural and material models assumed for the foam projectiles and the ceramic tile or RCC targets, the computational costs of the simulations, and the results of the numerical study, including suggestions for future research.

2.2 Numerical Method

In recent research focused on the design of orbital debris shielding, a new numerical method and parallel computer code have been developed for use in spacecraft design applications. This hybrid numerical method employs in tandem nondeforming Lagrangian particles and large strain finite element kinematics [74], to simulate impact problems involving shock loading, large deformation plasticity, and complex fragmentation dynamics. The method has been implemented in a three dimensional code and validated by comparison with published experiments at impact velocities ranging from 1 to 11 kilometers per second [32].

The hybrid method combines the general contact-impact modeling capabilities of particle methods with a true Lagrangian description of strength effects, the latter offered by finite element techniques. It avoids the tensile instability problems which have hindered the effective use of some particle techniques, as well as the mass and energy discard normally associated with Lagrangian finite element models of material failure. No particle to element mapping is required, since both particles and elements are used to represent distinct physical effects throughout the calculation. The particles model all inertia and all contact-impact as well as volumetric thermomechanical response in compressed states, while the elements model tension and elastic-plastic shear. Material failure is represented by the loss of element cohesion, after which particles not associated with any intact element are free to flow under general contact-impact loads.

In the case of spherical particles, the state space model for the particle-element system [74] consists of evolution equations for the particle translational momenta ($\mathbf{p}^{(i)}$) and center of mass position vectors ($\mathbf{c}^{(i)}$)

$$\dot{\mathbf{p}}^{(i)} = -\frac{\partial V}{\partial \mathbf{c}^{(i)}} - \mathbf{f}^{(i)} \, , \qquad \dot{\mathbf{c}}^{(i)} = m^{(i)-1} \, \mathbf{p}^{(i)} \tag{2.1}$$

augmented by evolution equations for the internal state variables

$$\begin{aligned}
\dot{S}^{(i)} &= \dot{S}^{(i)}(\mathbf{p}^{(i)}, \mathbf{c}^{(i)}, S^{(i)}, d^{(j)}, D^{(j)}, \mathbf{E}^{p(j)}) && (2.2)\\
\dot{d}^{(j)} &= \dot{d}^{(j)}(\mathbf{p}^{(i)}, \mathbf{c}^{(i)}, S^{(i)}, d^{(j)}, D^{(j)}, \mathbf{E}^{p(j)}) && (2.3)\\
\dot{D}^{(j)} &= \dot{D}^{(j)}(\mathbf{p}^{(i)}, \mathbf{c}^{(i)}, S^{(i)}, d^{(j)}, D^{(j)}, \mathbf{E}^{p(j)}) && (2.4)\\
\dot{\mathbf{E}}^{p(j)} &= \dot{\mathbf{E}}^{p(j)}(\mathbf{p}^{(i)}, \mathbf{c}^{(i)}, S^{(i)}, d^{(j)}, D^{(j)}, \mathbf{E}^{p(j)}) && (2.5)
\end{aligned}$$

where $\mathbf{f}^{(i)}$ is a damping force, $m^{(i)}$ is a particle mass, $S^{(i)}$ is a particle entropy, $d^{(j)}$ and $D^{(j)}$ are element shear and normal damage variables, $\mathbf{E}^{p(j)}$ is a plastic strain tensor, i is a particle index, j is an element index, and V is a thermomechanical potential

$$V = V(\mathbf{c}^{(i)}, S^{(i)}, d^{(j)}, D^{(j)}, \mathbf{E}^{p(j)}) \qquad (2.6)$$

The specific functional forms of the thermomechanical potential and the internal state evolution equations depend upon the constitutive assumptions as well as the adopted interpolations for the density and displacement fields. The present work investigated for the first time the application of this method to a relatively low velocity impact regime, in problems which nonetheless involved complex contact-impact, material failure, and fragmentation phenomena difficult to simulate using structural finite element codes.

2.3 Material Models

The simulations described here employed simple material models for the foam, tile, felt strain isolation pad (SIP), and RCC, with material properties estimated using the available experimental data. All materials were assumed to be isotropic elastic-perfectly plastic [55], with an accumulated plastic strain criterion applied to initiate element failure. The available material data base may be summarized as follows. In support of the Columbia accident investigation, Glenn Research Center [58] and Sandia National Laboratories (SNL) [51] performed mechanical property tests on foam, tile, and reinforced carbon-carbon. Mechanical property tests previously performed on SIP and on SIP-tile combinations are described by Sawyer [69] and Cooper and Sawyer [18] respectively. The relevant thermal properties for polyurethane, tile, SIP, and carbon-carbon materials are provided by Oertel [61], Banas et al. [7], Myers et al. [59], Ohlhorst et al. [62], and the commercial literature [19].

Table 2.1 lists estimated properties for the materials of interest. These values were used (except in the case of the SIP) to perform the simulations described in this chapter. The present analysis adopted a yield strength for the tile corresponding to the lowest experimental measurements of Lu et al. [51]. In the case of the RCC, the present analysis assumed a yield strength equal to the bending strength measured by Lu et al. [51], since the failure mode for the RCC panels was expected to be flexure of the panel surface under the foam impact load. At the time the present analysis was performed, the data available on SIP properties was very limited. As a result the SIP density was underestimated by a factor of 2.3, and the single layer of SIP elements used in the numerical model was assigned the same stiffness properties as the tile. The effect of the underestimating the SIP density was to slightly underestimate the target areal density, and in the present analysis is not considered to be significant. The experiments of Cooper and Sawyer [18] suggest that the stiff SIP elements used here would tend to overestimate the tile damage produced by the foam impact load.

More general models of the dynamic mechanical deformation and failure of the foam, tile, felt, and RCC materials are needed.

2.4 Ceramic Tile Impact

2.4.1 Tile Impact Model

Analysis of launch videos, supplemented by computational fluid dynamics studies, suggested that ceramic tiles located on the lower surface of Columbia might have been struck by a block of insulating foam shed from the vehicle's external tank. A series of experiments was therefore planned to measure the impact damage produced by highly oblique foam block impacts on tile arrays similar to those covering the lower surface of the Orbiter wing. Simulations were run in advance of these experiments, to estimate the impact damage. The simulation parameters are listed in Table 2.2.

In each simulation the target model was composed of a 2 x 4 foot array of 32 tiles, each tile having an areal extent of 6 x 6 inches. The uniform tile thickness matched that in the suspected impact areas, over the main landing gear door (MLGD) and in the nearby wing acreage. In the simulations the tile array was supported by an aluminum plate, whose lower surface was fixed along a circumferential edge strip, the latter with a width of one inch. The strain isolation pad (SIP) which separates the tile and the aluminum wing structure was modeled with a single layer of finite elements, however similar (gap filler) material often interposed between the individual tiles was not modeled. The foam projectile was modeled as a homogeneous hexahedral block. The dimensions, obliquity, and orientation of the foam block at impact were varied between simulations, due to uncertainties in the interpretation of the launch videos, a dependence of the impact obliquity on the vehicle impact location, and a desire to investigate the effect of projectile orientation (roll angle) on impact damage.

Computer resource requirements and some limitations of the research code and preprocessor used here made it necessary to introduce certain geometric approximations. Since available commercial preprocessors do not generate hybrid particle-finite element models, a special preprocessor was employed. The latter code generates solid models composed of uniform hexahedra, and associated ellipsoidal particles, so that an element and particle deletion process was used to introduce the gaps between the tiles. As a result the width of these gaps was overestimated. Combined with the aforementioned neglect of gap fillers, the assumed geometric model approximates conservatively the structural strength of the actual tile array. A second approximation was introduced in modeling the individual tiles, whose external surfaces are coated in a borosilicate layer, to a depth of approximately 5 percent of the tile thickness. Computer resource requirements precluded modeling of features with such small dimensions, so the tiles were taken to be monolithic with material properties derived from the published strength and stiffness properties of an individual tile.

2.4.2 Tile Impact Simulations

The four tile impact simulations were performed at the University of Texas on systems operated by NASA Ames Research Center, and required between three and five wall clock days on 128 or 192 processors of an SGI Origin. The models were composed of over one million particles, with the simulations extending over five or six milliseconds of physical time.

The first two simulations differed only with respect to projectile orientation (roll angle), and modeled the impact of a 1.06 pound block of foam, at a velocity of 700 feet per second, on a tile array similar to those which cover the main landing gear doors. Impact obliquity was five degrees. The simulations showed 12.0 cubic inches of material (0.178 tile volumes) eroded by the long edge impact and 19.6

cubic inches of material (0.290 tile volumes) eroded by the short edge impact. Figures 2.1 and 2.2 show the simulation results, including views of the predicted tile erosion. In both these simulations the maximum predicted depth of penetration was approximately one half of the tile thickness. Since the short edge impact appeared to be more damaging under the postulated impact conditions, subsequent simulations (and later experiments) involved foam blocks rotated so as to strike the tile array along the projectile's short edge. Experiments which approximately correspond to these two simulations were later performed by Kerr et al. [45]. The first experiment produced three craters with a total volume of approximately 0.1 cubic inches, although much of this damage may have been caused by the unintended impact of a Mylar burst disc used in the compressed air gun which launched the projectile. The second experiment produced no impact craters. Since the aforementioned numerical modeling assumptions minimized both tile strength and tile lateral support while maximizing the stiffness of the SIP layer, the tile impact damage was overestimated. However the eroded volume error was less than one third of one tile volume, with the damage distributed among several tiles.

The third and fourth simulations considered somewhat more severe impact conditions. The third case assumed a 2.24 pound projectile and a slightly reduced tile thickness (tile thickness varies with position over the lower surface of the Orbiter). The result was an increase in eroded material, to 48.2 cubic inches (0.789 tile volumes) and an increase in the maximum depth of penetration, to three quarters of the tile thickness. These simulation results are depicted in Figure 2.3. Finally the fourth case considered a lower mass projectile (1.53 pounds), but a slightly higher impact velocity (720 fps) and a more direct impact, with the impact obliquity taken to be 13 degrees. The tile thickness in the target was increased in order to represent a wing acreage area away from the main landing gear door. The simulation results, shown in Figure 2.4, predicted erosion of 70.6 cubic inches of material (0.785 tile volumes) and a maximum depth of penetration to the level of the SIP, in one small area. Experiments which approximately correspond to these two simulations were later performed by Kerr et al. [45]. The first experiment produced no impact craters. The second experiment produced four craters, each with an areal extent of less than 1.0 square inches (depth not provided). It appears that the aforementioned numerical modeling assumptions again caused the tile impact damage to be overestimated. The eroded volume error was less than one tile volume, with the damage distributed among multiple tiles.

In summary the pretest simulations predicted in the worst case the removal of less than one tile volume of ceramic material, under modeling assumptions which conservatively approximated tile strength properties, the lateral support provided in the tile gap region, and the compliance of the SIP layer. Subsequent testing showed that none of the impact configurations considered here produced significant damage to the target tile array.

2.5 Reinforced Carbon-Carbon (RCC) Impact

2.5.1 RCC Impact Model

As in the case of the underwing tiles, analysis of launch videos and complimentary computational fluid dynamics work suggested the possibility that wing leading edge of Columbia was subjected to a highly oblique foam block impact. A series of experiments on RCC panels was therefore planned to investigate the effects of such impacts, for panel geometries representative of the leading edge region most likely involved. Prior to these experiments, two simulations were run to estimate the impact damage. The simulation parameters are listed in Table 2.3.

The target model used in the simulations represented the geometry of wing leading edge panel number six. The limitations of the preprocessor used here again led to certain approximations. A profile for the model cross section was obtained by fitting coordinate data extracted from a CAD model of the actual panel, and assuming a constant RCC wall thickness. This cross section was then extended an axial distance equal to the total panel length, with stiffening ribs added at both ends, similar to those found on the actual part. The upper and lower edges of the panel were held fixed in the simulations. This target model was considered to be generally representative of the strength and stiffness of the actual structure. The simulations assumed that in the RCC elements failure would occur at a plastic strain of 0.01, a relatively brittle failure criterion. The thin silicon carbide coating present on the actual part was not modeled, again due to the high computational cost of simulations which resolve very small scale features. As discussed in a preceding section, the particle-element preprocessor used here produced models composed of uniform hexahedra, so that the curved surface of the RCC panel model was represented with a stairstep geometry.

The starting conditions for the two simulations differed only with respect to projectile orientation (roll angle), one objective of the analysis being to determine the relative severity of impact damage caused by edge and corner impacts. The specified impact point was located a distance of 18.1 inches from the panel edge, measured along the panel arc, and the impact obliquity (14.6 degrees) was specified as the angle between the target surface normal at the impact point and the projectile velocity vector, the latter aligned with the long axis of the foam block. The pitch, roll, and yaw of the projectile were computed so as to match these specifications.

2.5.2 RCC Impact Simulations

The RCC panel impact simulations were performed on SGI Origin systems at NASA Ames Research Center, and required between three and four wall clock days on 128 or 256 processors. The models were composed of approximately two million particles, with the simulations extending over no more than two milliseconds of physical time. The simulation results are depicted in Figure 2.5 (corner impact case) and Figure 2.6 (edge impact case). The first simulation modeled a corner impact and resulted in failure of the panel, with a crack approximately 6 inches in length developing along the panel surface, normal to the leading edge stagnation line. The second simulation modeled an edge impact and showed greater panel damage, in this case multiple cracks, the largest extending along half the length of the panel and aligned parallel to the stagnation line.

Although the scope of the RCC impact simulation work described here was limited, the results indicate failure of the panel under the postulated foam impact loads. These results are in general consistent with later experiments conducted on Space Shuttle wing leading edge panels. Experiments which approximately correspond to these two simulations were performed by Kerr et al. [45]. In the first experiment, a corner impact test conducted on a panel six target at a 21 degree obliquity resulted in a crack of length 5.5 inches located at the panel edge and oriented parallel to the stagnation line. In the second experiment, an edge impact test conducted on a panel eight target at a 25 degree obliquity resulted in gross failure of the panel surface, producing a 17 inch by 16 inch hole in the panel surface. Comparison of the experiments and simulations is complicated by differences in target geometry and impact obliquity. Since the experiments involved higher impact obliquities, they would be expected to produce more damage than is depicted in the simulations. The first simulation showed a crack similar in size to that observed in the first experiment, although the predicted location and orientation were not correct. The second simulation showed large cracks in the panel surface, at an impact obliquity 10 degrees less than that which resulted in gross panel failure in the second experiment. In general the numerical modeling work, which incorporated best case assumptions with regard to RCC strength and ductility, appears to provide good estimates of panel impact damage.

2.6 Conclusions

The present work has described a series of pre-test simulations performed to estimate damage produced by external foam strikes on thermal protection system components of the Space Shuttle. The simulations employed a hybrid particle-finite element technique and a parallel computer code developed for use in spacecraft design applications. The simulation results are in general consistent with experimental results available for this class of problems, and indicate that the numerical method used here is suitable for application in a relatively low velocity regime. The application of this numerical technique to future impact problems would be facilitated by further methods and interface development work, aimed at accommodating complex structural geometries described by a standard CAD data base or a commercial finite element preprocessor. The interface development work will allow the hybrid particle-finite element technique used here to model impact on any structural geometry described by a general hexahedral finite element mesh.

Several conclusions specific to the operation of the Space Shuttle and the design of future aerospace planes are suggested: (1) additional material testing and constitutive modeling research describing the deformation and failure of thermal protection system materials is needed, (2) numerical methods and code development work is needed to provide a validated computer simulation capability for impact damage assessment, (3) additional, higher resolution simulations should be performed, to investigate the effects of any simplifying assumptions made in the areas of material modeling and structural geometry, and (4) additional impact testing should be conducted, over a wider range of impact conditions, to validate proposed computational analysis techniques.

Material property	Foam	Tile	SIP	RCC
Young's modulus,				
MPa	9.4	62.2	1.5	15.2×10^{3}
(psi)	(1,360)	(9,022)	(220)	(2.21×10^{6})
Shear modulus,				
MPa	3.6	24.2	0.76	7.2×10^{3}
(psi)	(529)	(3,510)	(110)	(1.04×10^{6})
Reference density,				
g/cm^{3}	0.0344	0.1442	0.197	1.5794
(lb/ft^{3})	(2.15)	(9.00)	(12.3)	(98.6)
Yield stress,				
MPa	0.29	0.16	0.19	96.53
(psi)	(42.2)	(23.9)	(27.4)	(14.0×10^{3})
Specific heat,				
J/kg-degree K	1900.81	632.21	1318.84	715.94
(Btu/lbm-degree F)	(0.454)	(0.151)	(0.315)	(0.171)
Thermal expansion coefficient,				
1/degree K	0	4.05×10^{-7}	1.8×10^{-5}	1.31×10^{-6}
(1/degree F)	(0)	(2.25×10^{-7})	(1.00×10^{-5})	(7.28×10^{-7})
Plastic failure strain	1.0	1.0	1.0	0.01

Table 2.1: Material properties

Parameter	MLDG 1	MLGD 2	MLGD 3	Wing Acreage
Projectile velocity (fps)	700	700	700	720
Impact obliquity (degrees)	5	5	5	13
Projectile roll (degrees)	90	0	0	0
Projectile cross section (in)	3.5 x 11.5	3.5 x 11.5	5.5 x 11.5	5.5 x 11.5
Projectile length (in)	21.25	21.25	28.5	19.0
Tile thickness (in)	1.875	1.875	1.700	2.450
Aluminum plate thickness (in)	0.1875	0.1875	0.2689	0.2720
Simulation time (milliseconds)	5.0	5.0	6.0	5.0
Number of particles (millions)	1.10	1.10	1.42	1.48
Number of processors (SGI Origin)	128	128	192	192
Wall clock time (hours)	76.5	90.1	127	102

Table 2.2: Parameters of the tile impact simulations

Parameter	Corner impact case	Edge impact case
Projectile velocity (fps)	775	775
Projectile dimensions (in)	5.5 x 11.5 x 22.8	5.5 x 11.5 x 22.8
Projectile roll, pitch, yaw (degrees)	0.0, 17.5, 6.32	30.0, 17.5, 6.32
Impact obliquity (degrees)	14.6	14.6
Panel dimensions (in)	20.5 x 38.4 x 21.3	20.5 x 38.4 x 21.3
Panel thickness (in)	0.25	0.25
Simulation time (milliseconds)	1.635	2.000
Number of particles (millions)	1.90	1.90
Number of processors (SGI Origin)	128	256
Wall clock time (hours)	96	74

Table 2.3: Parameters of the wing leading edge impact simulations

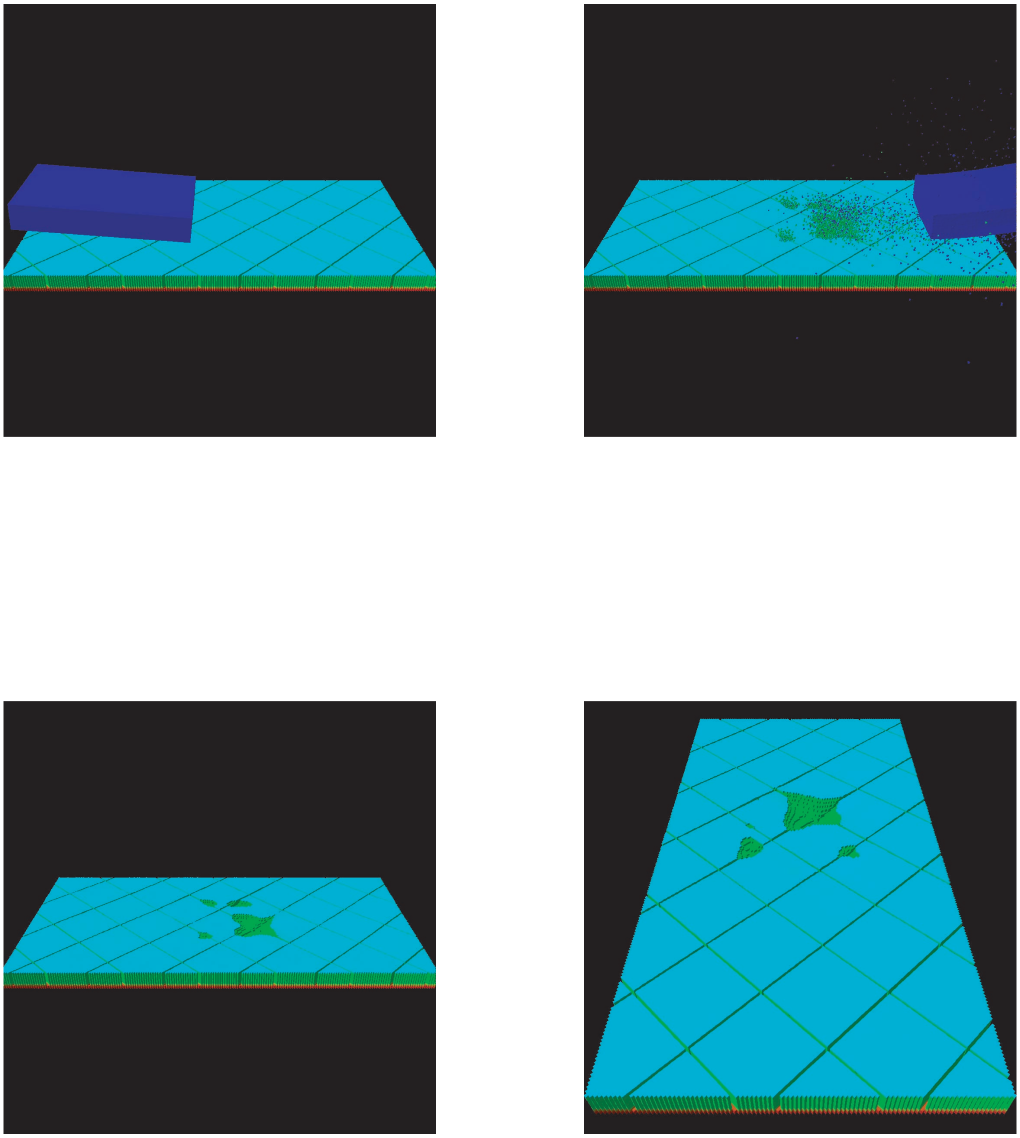

Figure 2.1: Simulation results for case MLGD 1

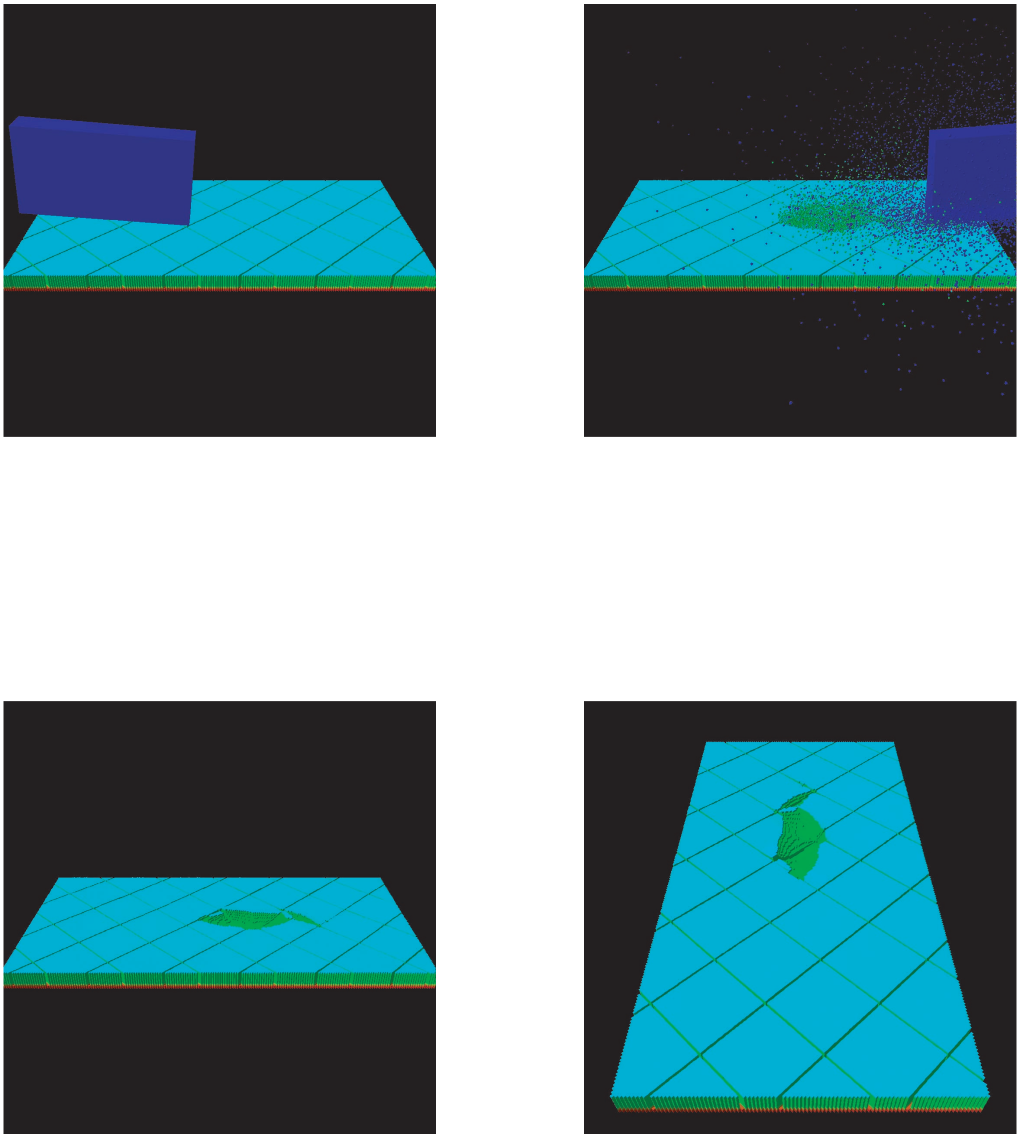

Figure 2.2: Simulation results for case MLGD 2

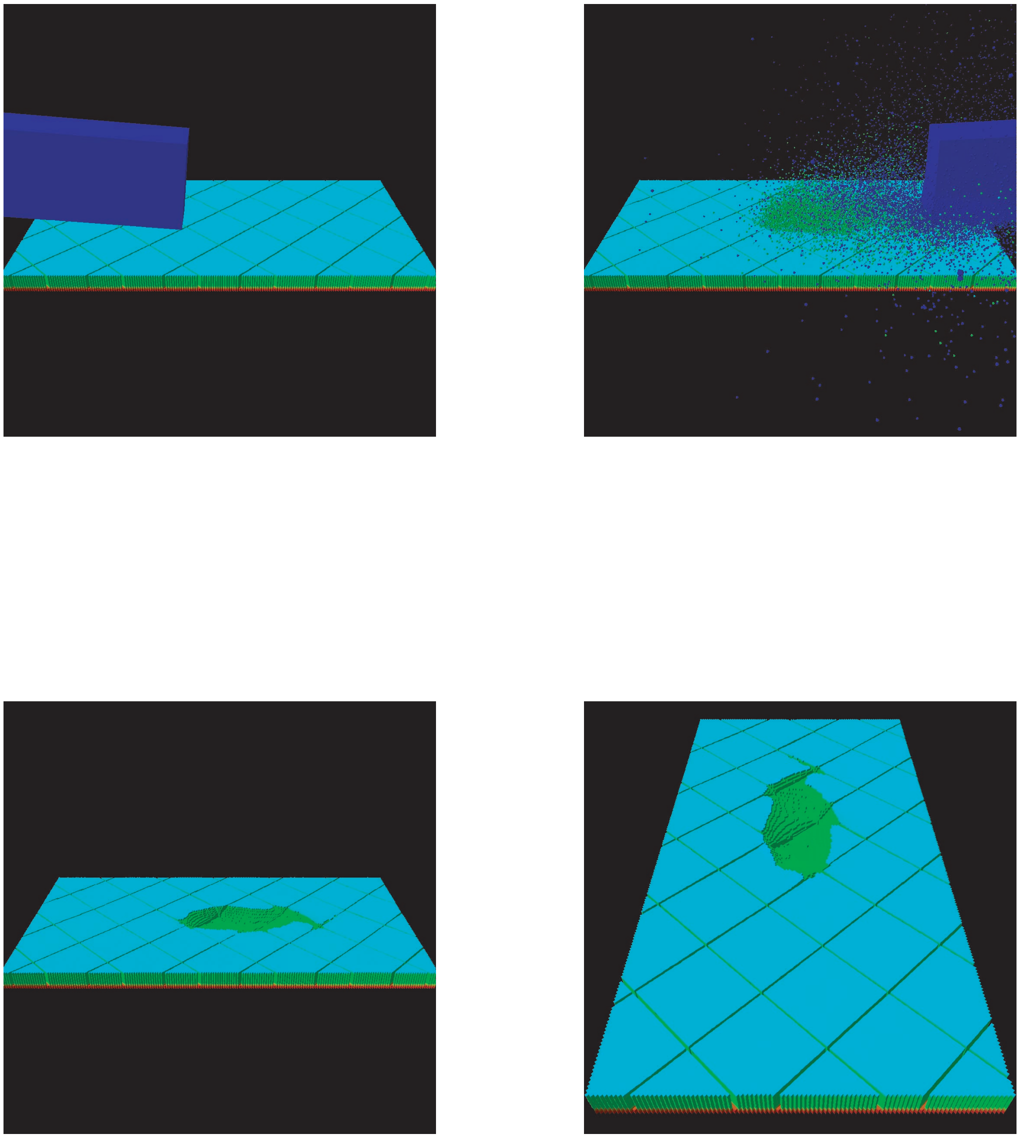

Figure 2.3: Simulation results for case MLGD 3

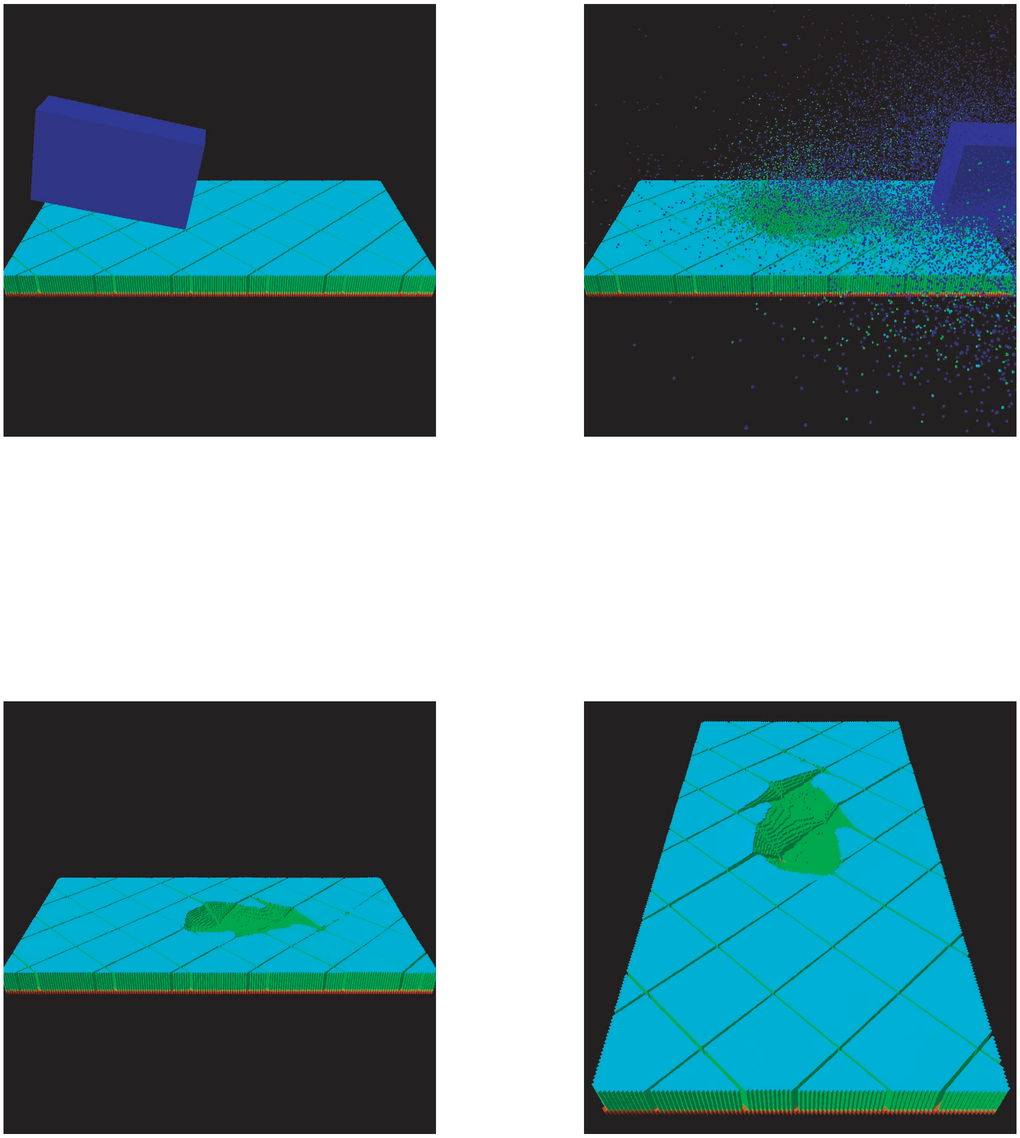

Figure 2.4: Simulation results for the wing acreage impact case

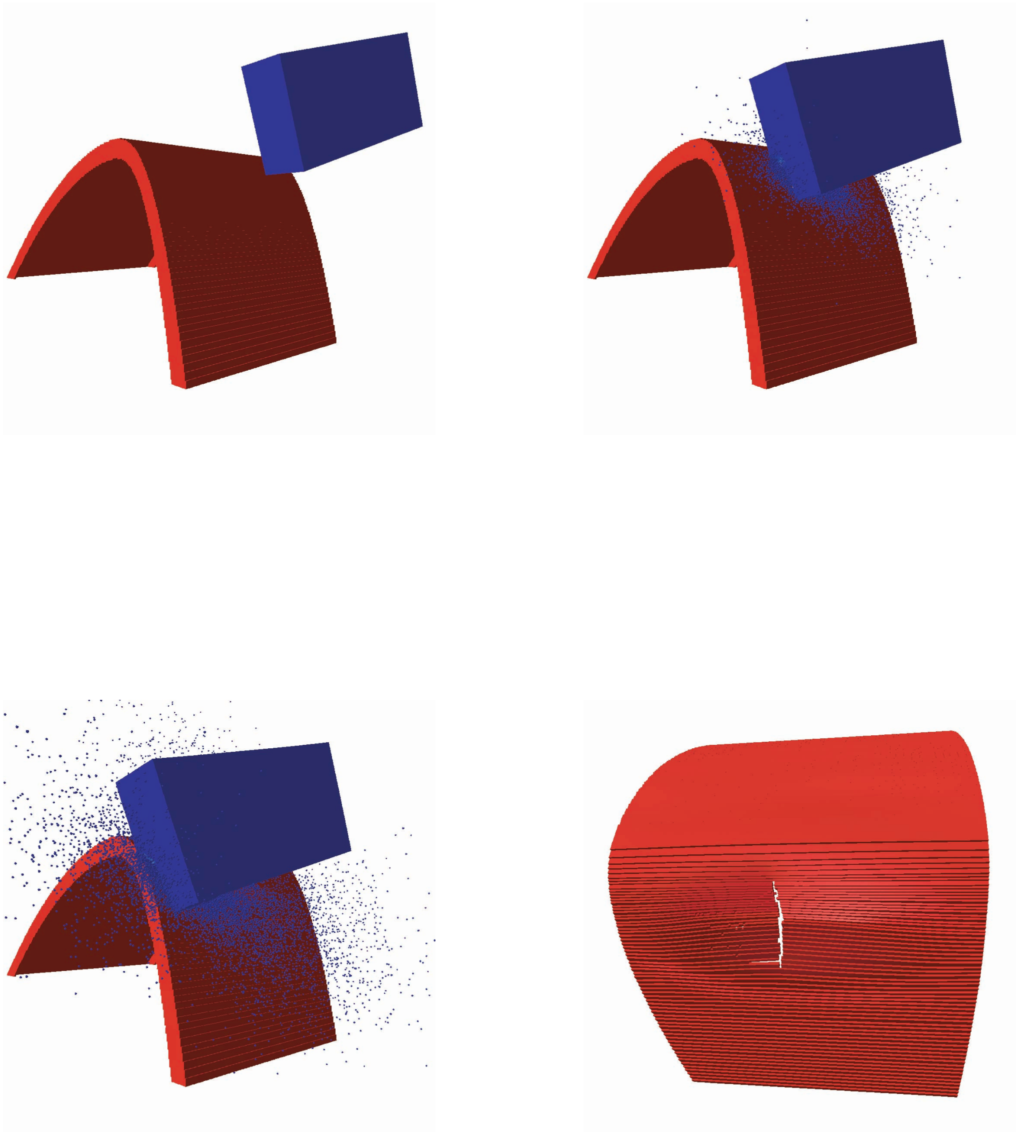

Figure 2.5: Simulation results for the RCC corner impact case

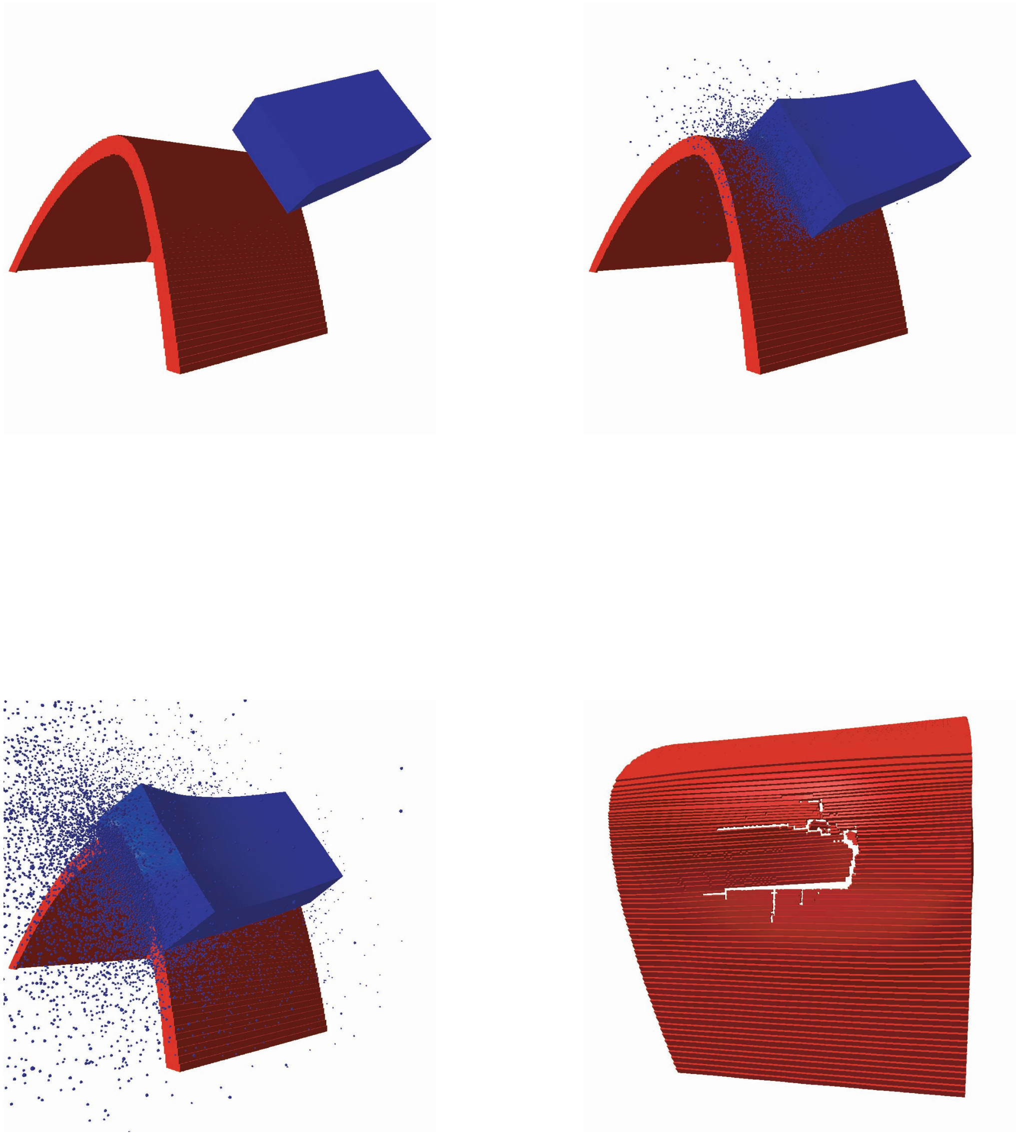

Figure 2.6: Simulation results for the RCC edge impact case

Chapter 3

Simulation of Hypervelocity Impact on Aluminum-Nextel-Kevlar Orbital Debris Shields

3.1 Introduction

Advanced orbital debris shield designs often incorporate a multi-plate geometry and are fabricated of composite materials. An example is the aluminum-Nextel-Kevlar shields developed by NASA [15] for application on the International Space Station (ISS). Simulation of hypervelocity impact effects on these shielding designs is difficult, due both to their geometry and their material composition. Since multi-plate shields distribute the allocated shielding mass over more than one bumper, they reduce the minimum bumper thickness and in general increase the computational cost of the simulation. The extensive use of composite materials in advanced shielding designs complicates the simulation problem for two basic reasons: (a) the requirement to consider nonhomogeneous or anisotropic media increases the number of internal state variables which must be evolved in any numerical simulation, and (b) the thermomechanical response of such materials, generally more complex than that of aluminum or other metals, may be only partially described by the existing material property data base. In spite of these complications, simulation of the hypervelocity impact response of multi-plate metal-composite debris shields is of strong engineering interest, due to their proven effectiveness as components of spacecraft protection systems [11]. The present work describes numerical implementation of a rate dependent material model for Kevlar [80][81], and the conduct of several three dimensional simulations, performed to investigate the hypervelocity impact response of aluminum-Nextel-Kevlar debris shields like those deployed on the ISS. The simulations employed a hybrid-particle finite element method [29][74] and a parallel computer code [26] specifically developed to address the orbital debris shielding design problem. Simulation work appears to conservatively estimate the protection afforded by multi-layered aluminum-Nextel-Kevlar shielding.

3.2 Composite Shielding Materials

Kevlar aramid fiber, introduced by the Du Pont Company in 1972, has been used in a variety of impact protection applications. The woven cloth Nextel (manufactured by 3M corporation) is made from alumina, a ceramic shown to provide effective impact protection when applied as a component of composite armor systems. These materials are used in the design of the multiplate orbital debris shielding deployed on some modules of the ISS. The latter shielding consists of three material layers, arranged in the sequence: aluminum, Nextel, Kevlar. The outer aluminum bumper is located approximately eleven centimeters from the pressurized module, a multilayer stack of Nextel cloth is located approximately halfway between the aluminum bumper and the pressure wall, and a multilayer stack of Kevlar cloth is located directly behind the Nextel. Nextel is manufactured in various grades [3]. A number of different grades of Kevlar are also manufactured, with Kevlar 29 (all purpose yarn), Kevlar 49 (high modulus yarn), and Kevlar 129 (high tenacity yarn) used in composite armor applications [83]. Table 3.1 lists mechanical properties of these three grades of Kevlar, while Table 3.2 compares some important material properties of high performance Nextel and Kevlar fibers.

3.3 Impact Simulations

Experimental work has demonstrated that aluminum-Nextel-Kevlar shields perform much better than weight equivalent Whipple shield designs. Hence the development of a validated computer aided design tool for use in future composite shielding design studies is of considerable interest. Fahrenthold and Shivarama [31] described some initial work on the use of a hybrid particle-finite element method for composite shield impact simulations. The previous work [31] used a rather coarse three dimensional model of less than 0.5 million particles, and a simulation time of less than 55 microseconds. The simulations discussed here involved an order of magnitude increase in particle count and a three-fold increase in simulation time. Related work using SPH and finite element methods has been reported by Hiermaier et al. [41] and Palmieri [64], although the latter efforts have focused on the use of Kevlar-epoxy plates [21], in lieu of the cloth Kevlar material modeled here. Three of the four simulations described in the present chapter modeled an experiment performed by Grosch [35], test number SwRI 7139-24, in which a 1.07 gram inhibited shaped charge (ISC) projectile struck a two-thirds scale model composite orbital debris shield similar to that deployed on the ISS. Parameters of the experiment are detailed in Table 3.3. The impact velocity is 11 kilometers per second, and the impact obliquity is 45 degrees. The first simulation reported here modeled the ISC projectile used in the experiment. A second simulation was performed using a spherical projectile with the same mass as the experimental (ISC) projectile, in order to investigate the effect of projectile shape [17] on the simulation results. A concern in the conduct of any hypervelocity impact simulation is the use of an appropriate equation of state. However there is no validated Mie-Gruneisen or tabular equation of state data for either Nextel cloth or Kevlar cloth. The aforementioned work of Hiermaier et al. [41] developed an equation of state and an orthotropic elastic model for Kevlar-epoxy, as well as a compaction equation of state for Nextel. The Kevlar layer modeled here does not include epoxy, and a compaction model for Nextel may not be appropriate for use in the present application [64]. Hence the first and second simulations presented here used a linear equation of state and the material properties listed in Table 3.4 [31][76]. The first simulation represented the ISC projectile as a hollow aluminum cylinder, with dimensions estimated from the experimental radiographs. The exact mass and geometry of ISC projectiles is somewhat uncertain. Both simulations employed approximately 6 million particles, and required approximately 252 wall clock hours to complete, in parallel execution on 16 processors of an IBM Regatta. Figures 3.1 and 3.2 show respectively an element plot of the first case at the simulation start time, and a particle plot of the simulation results at 100 microseconds after impact. Figures 3.3 and 3.4 show element plots of the damage at each level of the multi-plate structure, again at 100 microseconds. The simulation results underestimate the composite shield performance, since the experimental results showed a bulged but not perforated wall plate. A comparison of the first and second simulations, involving mass equivalent spherical and ISC projectiles, is provided by the wall plate plot of Figure 3.5, showing the results of the spherical projectile impact simulation, at 150 microseconds after impact. The results suggest that projectile geometry effects are significant even at the upper end of the orbital debris velocity regime.

3.4 Composite Material Models

The preceding simulation results underestimate the protection afforded by composite shielding materials. To investigate the effects of changes in the composite material models on the predicted shielding performance, both the Nextel and Kevlar equations of state were modified, and a rate-dependent strength model was introduced for the Kevlar. Two additional simulations were then conducted using the modified composite material models. The modified equations of state for Nextel and Kevlar used a Mie-Gruneisen functional form [85]

$$P = P_H \left(1 - \frac{\Gamma \mu}{2}\right) + \Gamma_\rho \left(E - E_0\right) \tag{3.1}$$

$$\begin{aligned} P_H &= K_1\mu + K_2\mu^2 + K_3\mu^3 \qquad && if \quad \mu \geq 0 \\ &= K_1\mu && if \quad \mu < 0 \end{aligned} \tag{3.2}$$

where

$$\mu = \frac{\rho}{\rho_0} - 1 \tag{3.3}$$

and Γ is Gruneisen parameter, ρ is current density, ρ_0 is initial density, E is internal energy per unit mass, E_0 is internal energy per unit mass at ambient density and pressure, and K_1, K_2, K_3 are constants, and the estimated material properties listed in Table 3.4, with the Gruneisen gamma for Nextel and Kevlar approximated using the formula [44]

$$\Gamma = \beta\kappa/\rho C \tag{3.4}$$

where β is the thermal expansion coefficient, κ is the bulk modulus, C is the specific heat, and ρ is the density. The engineering application discussed here involves very high strain rate loading, hence any variation of material properties with strain rate is of considerable interest. Two recent papers [80][81] describe a significant strain rate dependence in the measured mechanical response of Kevlar 49, as summarized in Table 3.5, for experiments conducted over a large strain rate regime. The parameters listed in Table 3.5 refer to the (apparent) Young's modulus, the maximum engineering stress, and the engineering strain at maximum engineering stress, as measured under uniaxial loading conditions. There is no data showing a similar strain rate dependence for Nextel. For use in later impact simulation work, the maximum stress versus strain rate data of Table 3.5 were fit to the function

$$\frac{\sigma}{\sigma_0} = g(\dot{\varepsilon}) \tag{3.5}$$

where σ is the maximum engineering stress at a strain rate $\dot{\varepsilon}$, and

$$g(\dot{\varepsilon}) = 1 \qquad \dot{\varepsilon} \leq \dot{\varepsilon}_0 \tag{3.6}$$

and

$$g(\dot{\varepsilon}) \quad = \quad 1 + a\left[ln\frac{\dot{\varepsilon}}{\dot{\varepsilon}_0}\right]^m \qquad \dot{\varepsilon} > \dot{\varepsilon}_0 \tag{3.7}$$

As indicated in Figure 3.6, for Kevlar 49

$$a = 0.0064, \quad m = 1.4 \tag{3.8}$$

where the reference values of stress and strain rate are

$$\sigma_0 = 2340 \ MPa, \quad \dot{\varepsilon}_0 = 0.0001 \ s^{-1} \tag{3.9}$$

To investigate the effects of rate dependence on predicted Kevlar impact response, the plasticity model of reference [29] was modified, as described in the equations which follow, and used in the two simulations discussed next. Note that the plasticity model outlined here incorporates large strain kinematics and an isochoric plastic deformation constraint. The nonassociated flow rule for the plastic strain rate ($\dot{\mathbf{E}}^p$) is

$$\dot{\mathbf{E}}^p = \dot{\lambda}\left(\mathbf{C}^p\mathbf{W} + \mathbf{W}\mathbf{C}^p\right) \tag{3.10}$$

where $\dot{\lambda}$ is a scalar multiplier and

$$\mathbf{W} = \mathbf{C}^p\mathbf{S}^{eff} + \mathbf{S}^{eff}\mathbf{C}^p - \frac{1}{3}tr\left[\mathbf{C}^p\mathbf{S}^{eff} + \mathbf{S}^{eff}\mathbf{C}^p\right]\mathbf{I} \tag{3.11}$$

with the effective stress tensor and plastic Cauchy-Green strain tensor defined by

$$\mathbf{S}^{eff} = \frac{(1-d)2\mu_0\mathbf{E}^e}{g(\dot{\varepsilon})}, \quad \mathbf{C}^p = \mathbf{I} + 2\mathbf{E}^p \tag{3.12}$$

where $\dot{\varepsilon}$ is the effective strain rate, $\mathbf{E}^e$ is the elastic deviatoric strain, d is the deviatoric damage, and μ_0 is the shear modulus. The yield condition is

$$f = \tau - Y, \quad \tau = \left\{ \frac{1}{2} tr \left[\mathbf{S}^{eff^T} \mathbf{S}^{eff} \right] \right\}^{1/2} \tag{3.13}$$

where τ is the second invariant of the effective stress. The yield stress Y is

$$Y = \frac{1}{2} \left(1-d\right) Y_0 \ \left\{1 - \gamma\theta\right\} \tag{3.14}$$

where Y_0 is the reference yield stress, γ is a thermal softening modulus, and θ is the homologous temperature. The plastic strain increment at each time step is determined using a one step iteration procedure with

$$\Delta\lambda = \frac{\left(\tau - Y\right) \Lambda \left(\tau - Y\right)}{\left(1-d\right) 2\mu_0 \, \omega \, g(\dot{\varepsilon})} \tag{3.15}$$

where Λ denotes the unit step function and

$$\omega = \left\{ \frac{1}{2} tr \left[\mathbf{W}^T \mathbf{W} \right] \right\}^{1/2} \tag{3.16}$$

The preceding modified material models were used in two additional three dimensional simulations of hypervelocity impact effects on aluminum-Nextel-Kevlar shielding. The first simulated a published light gas gun experiment [15], while the second again considered the ISC experiment discussed in the last section. The light gas gun experiment was JSC test B536 [15], and involved the oblique (15 degree) impact of a 1.0 gram aluminum sphere on a full scale aluminum-Nextel-Kevlar shield, at a velocity of 6.86 km/s. Parameters of the experiment are listed in Table 3.6. The simulation employed 1.18 million particles and required 63.2 wall clock hours to complete on 16 processors of an IBM Regatta. The simulation results (Figures 3.7 and 3.8) indicate at 150 microseconds a slightly deformed but not perforated wall plate. The experiment showed a "slight dish," indicating that the simulation results provide an accurate estimate of the wall plate damage. Since simulation of this light gas gun test showed good agreement with the corresponding experiment, simulation of the ISC projectile test SwRI 7139-24 was repeated with a relatively high resolution model and the modified material models discussed in this section. The simulation employed 15.6 million particles and required 305 wall clock hours to complete on 512 processors of an SGI Origin. The simulation results (Figures 3.9 and 3.10) indicate at 75 microseconds a perforated wall plate. The effect of introducing nonlinear equations of state for the composites and a rate dependent Kevlar model appears in this case to be rather small, with the simulation again overestimating the wall plate damage. The results reported here suggest that the hybrid particle-element method used in the simulations is numerically robust and captures important basic features of multi-plate impact experiments. For example, the intermediate composite shields are perforated, not fluidized, by the debris cloud impact. However the results also suggest that modeling improvements are needed, in order to better represent the available experimental impact data. The present study suggests possibilities for future work in both the modeling and experimental areas. First, the modeling of damage induced anisotropy [24], commonly encountered for example in ceramic media, may be investigated to determine its effect on predicted shield performance. Second, impact experiments using a simpler target geometry might be conducted, with a primary goal of materials characterization in mind.

3.5 Conclusions

The hybrid numerical method utilized here has been applied with some success to model the impact of metal projectiles and targets, over a wide range of velocities. The present work has described development of a rate dependent material model for Kevlar and three dimensional simulation work aimed at extending the formulation, for use in the computer aided design of multi-plate composite orbital debris shields. Both the geometry and the material composition of such shields complicate the simulation problem. The simulation results conservatively estimate the protection afforded by multi-layered aluminum-Nextel-Kevlar shielding. Additional material modeling work, guided by impact tests focused on materials characterization issues, is expected to improve upon current simulation capabilities. The rather high computational cost of three dimensional multi-plate shield impact simulations emphasizes the importance of developing efficient parallel numerical implementations.

Yarn properties	Kevlar 29	Kevlar 49	Kevlar 129
Tensile Strength, GPa (Kpsi)	2.9 (420)	2.9 (420)	3.4 (485)
Initial Modulus, GPa (Mpsi)	71 (10.3)	120 (17.4)	97 (14)
Elongation (%)	3.6	2.8	3.3
Density, g/cm^3 (lb/ft^3)	1.44 (89.9)	1.45 (90.5)	1.45 (90.5)

Table 3.1: Mechanical properties of Kevlar aramid fibers

Fiber type	Density, g/cm^3 (lb/ft^3)	Strength, GPa (Kpsi)	Modulus, GPa (Mpsi)	Elongation %	Fiber diameter μm (in)
Kevlar 129	1.45 (90.5)	3.4 (485)	97 (14)	3.3	12 (4.7e-4)
Nextel	2.5 (156)	1.72 (249.5)	152 (22)	2	13 (5.1e-4)

Table 3.2: Comparison of mechanical properties for Kevlar 129 and Nextel

Projectile mass (aluminum, L/D = 1)	1.07 g
Bumper thickness (aluminum)	0.127 cm
Nextel areal density	0.400 g/cm^2
Kevlar areal density	0.128 g/cm^2
Wall plate thickness (aluminum)	0.3175 cm
Total standoff	7.62 cm
Projectile velocity	11.25 km/s
Impact obliquity	45 degrees

Table 3.3: Parameters of SwRI test number 7139-24

Material property	Aluminum	Nextel	Kevlar
Shear modulus, Mbar (Mpsi)	0.271 (3.93)	0.164 (2.38)	0.100 (1.45)
Reference density, g/cm^3 (lb/ft^3)	2.7 (168.6)	2.7 (168.6)	1.45 (90.5)
Reference sound speed, cm/μsec (in/μsec)	0.524 (0.206)	0.4968 (0.196)	0.5352 (0.211)
Reference yield stress, Mbar (Kpsi)	0.0029 (42.1)	0.0172 (116.0)	0.034 (116.0)
Strain hardening exponent	0.1	0.0	0.0
Strain hardening modulus	125.0	0.0	0.0
Melt temperature, degrees Kelvin (degree F)	1,220 (1736.3)	1,220 (1736.3)	700 (800.3)
Specific heat, Mbar-cm^3/g-kilodegrees Kelvin	0.00884	0.00884	0.00142
(Btu/lb-degree F)	0.211	0.211	0.034
Spall stress, Mbar (Kpsi)	0.012 (174.05)	0.100 (1450.4)	0.100 (1450.4)
Plastic failure strain	1.0	1.0	1.0
Thermal expansion coefficient, per kilodegrees Kelvin (per degree F)	0.0216 (1.2e-5)	0.009 (0.5e-5)	0.038 (2.13e-5)
Mie-Gruneisen gamma	1.97	0.2513	0.7666
Mie-Gruneisen slope coefficient	1.4	1.0	1.0

Table 3.4: Material properties used in the simulation

Strain rate	0.0001 s^{-1}	0.01 s^{-1}	140 s^{-1}	440 s^{-1}	1350 s^{-1}
E, GPa (Mpsi)	97 (14.1)	100 (14.5)	112 (16.2)	119 (17.3)	125 (18.1)
σ_{max}, GPa (Kpsi)	2.34 (339.4)	2.47 (358.2)	2.94 (426.4)	3.02 (438.0)	3.08 (446.7)
ε_m (%)	3.29	3.33	3.54	3.64	3.86

Table 3.5: Mechanical properties of Kevlar 49 versus strain rate

Projectile mass (aluminum sphere)	1.0 g
Bumper thickness (aluminum)	0.16 cm
Nextel areal density	0.600 g/cm^2
Kevlar areal density	0.192 g/cm^2
Wall plate thickness (aluminum)	0.48 cm
Total standoff	11.4 cm
Projectile velocity	6.86 km/s
Impact obliquity	15 degrees

Table 3.6: Parameters of JSC test number B536

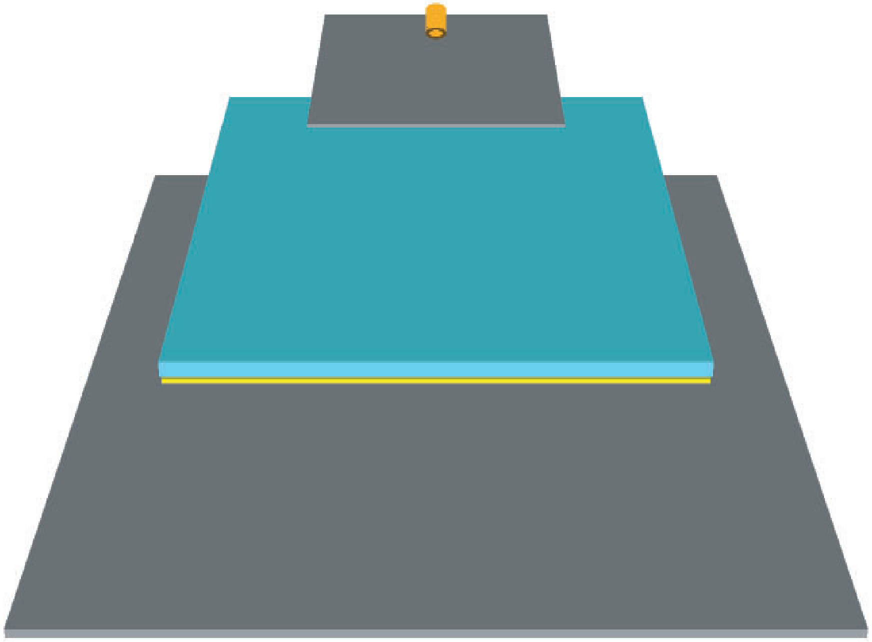

Figure 3.1: Element plot of the initial configuration

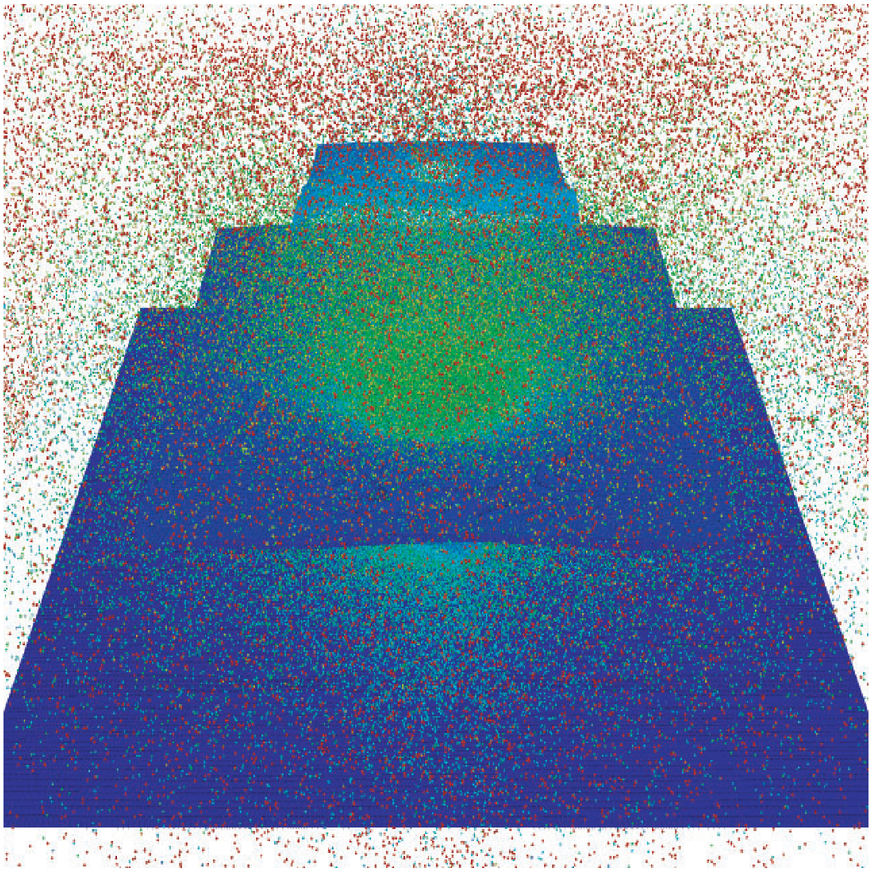

Figure 3.2: Particle plot of the simulation results at 100 microseconds after impact

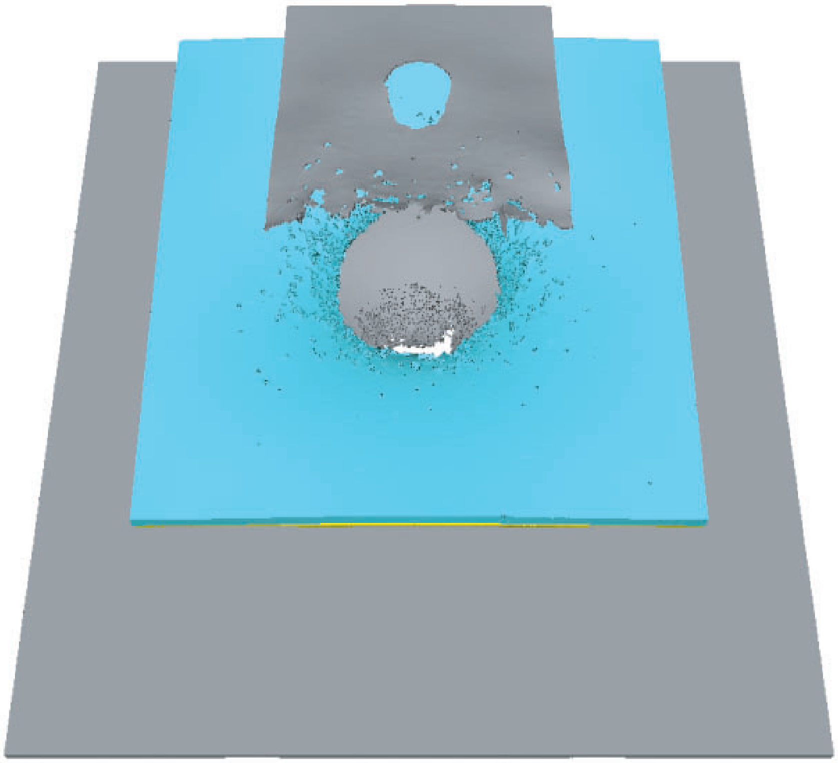

Figure 3.3: Element plot of the simulation results at 100 microseconds after impact

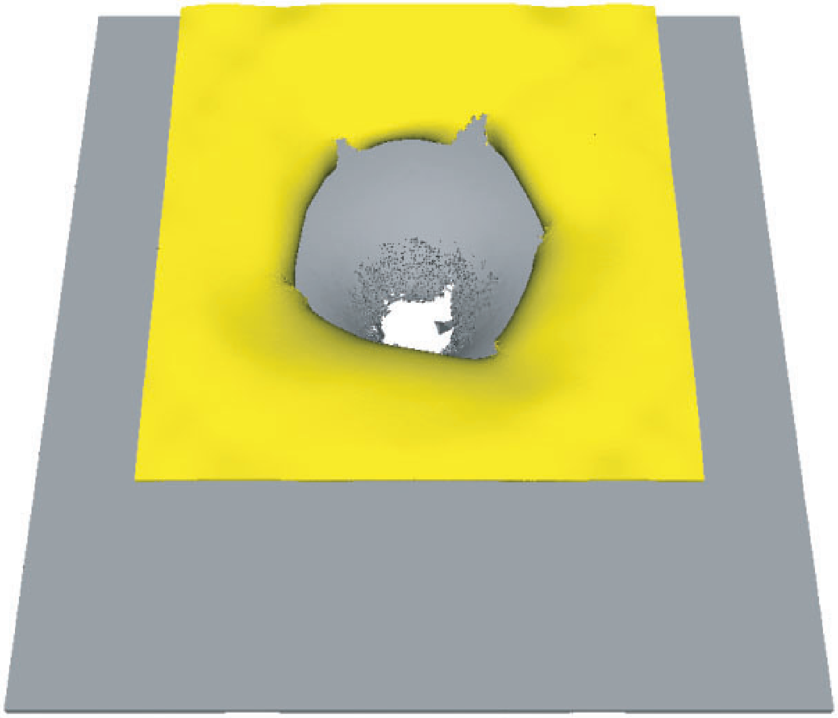

Figure 3.4: Element plot of the Kevlar shield and wall plate at 100 microseconds after impact

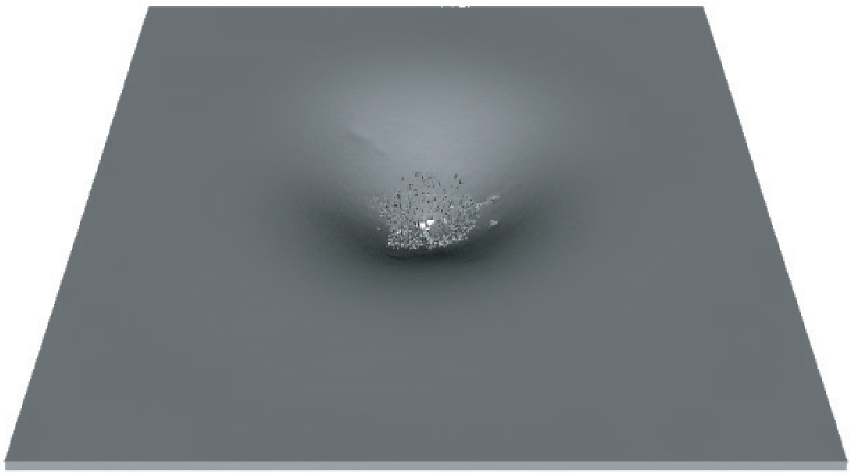

Figure 3.5: Element plot of the wall plate damage, spherical projectile

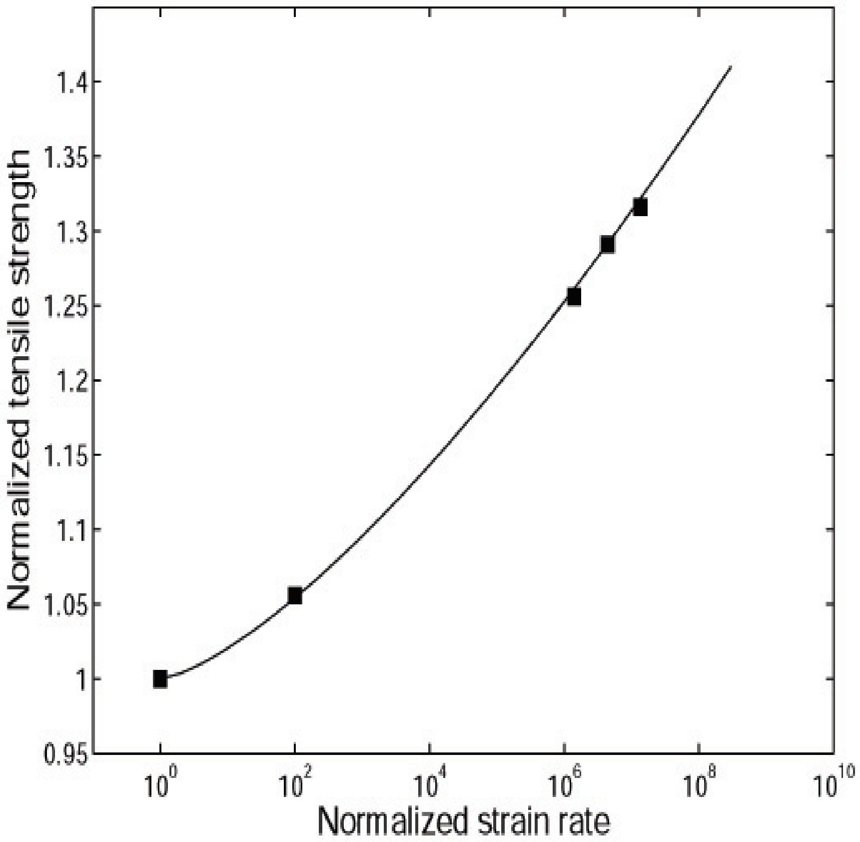

Figure 3.6: Strain rate dependence of tensile strength of Kevlar 49

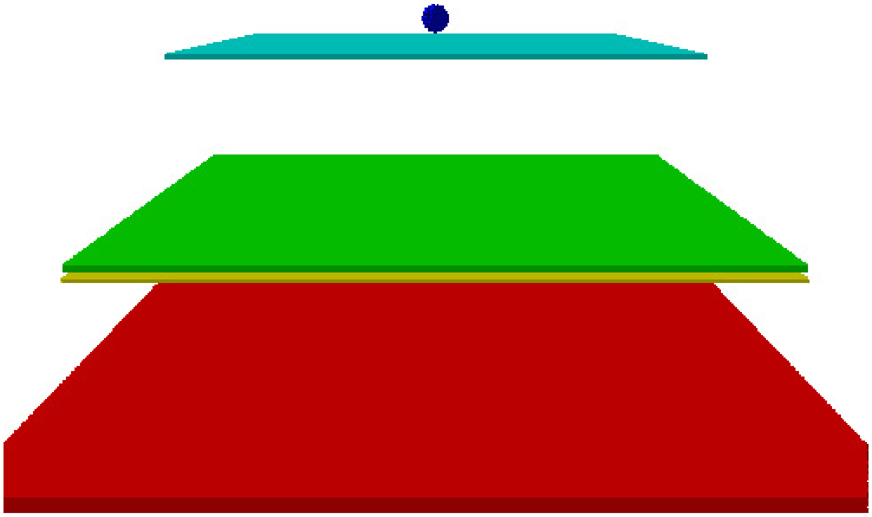

Figure 3.7: Element plot of the initial configuration

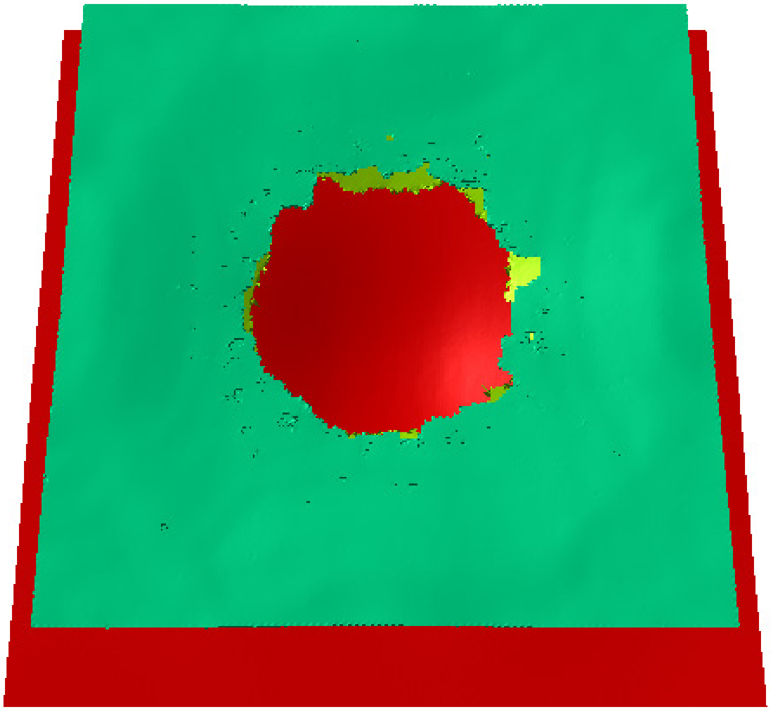

Figure 3.8: Element plot of the Kevlar shield and wall plate at 150 microseconds after impact

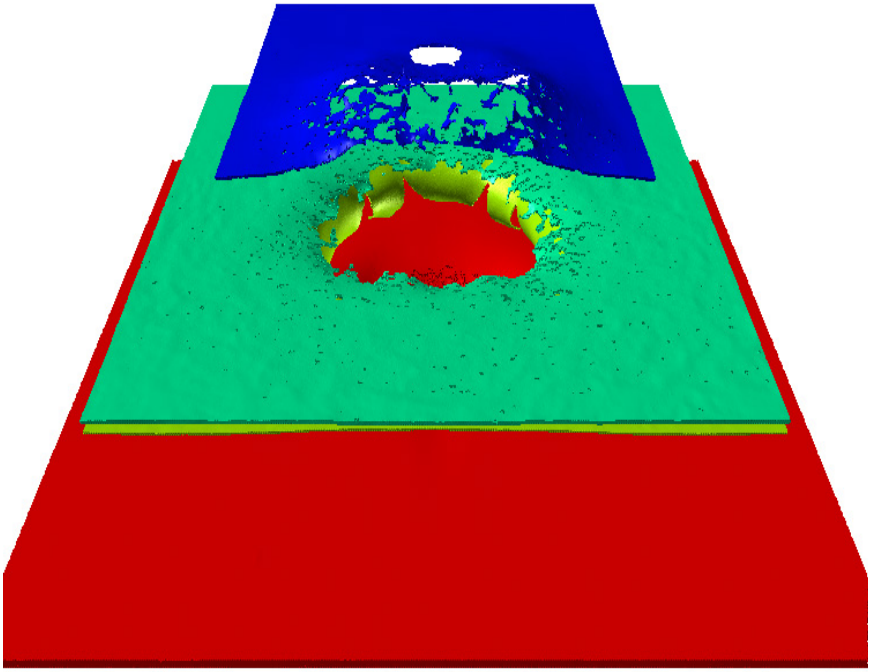

Figure 3.9: Element plot of the simulation results at 75 microseconds after impact (front view)

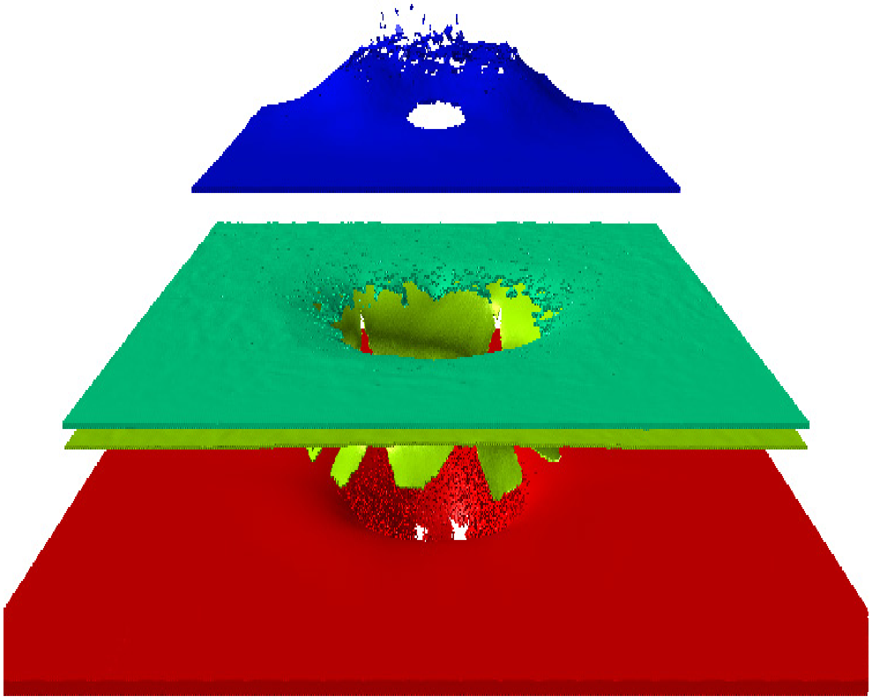

Figure 3.10: Element plot of the simulation results at 75 microseconds after impact (rear view)

Chapter 4

A Kernel Free Particle-Finite Element Method for Hypervelocity Impact Simulation

4.1 Nomenclature

Nomenclature is presented at the end of this chapter.

4.2 Introduction

Studies of hypervelocity impact phenomena are motivated by a variety of science and engineering applications [23]. Examples include scientific research on planetary impacts [34] and equations of state [46] and engineering research on the design of spacecraft shielding [39] and kinetic energy penetrators [84]. The proceedings of a recent international symposium [23] show that the use of computer simulation in this field is increasing, as improvements in numerical methods and computing power make it possible to address problems of greater complexity and larger scale. Simulation is of particular importance, as an adjunct to experimental work, when material costs are high [16] or when impact velocities beyond the range of light gas guns are of interest [17].

Simulation work in this field has applied a number of different numerical methods, based on continuum mechanics, particle dynamics, or mixed kinematic schemes. Continuum methods [10] employ either an Eulerian hydrodynamic [56][40] or a Lagrangian finite element [37] approach, or some Arbitrary Lagrangian-Eulerian (ALE) based generalization of these techniques [13][79]. A large majority of particle codes employ a Smooth Particle Hydrodynamics (SPH) technique [78][72][63], although some alternative particle based methods have been proposed [9]. Some disadvantages of pure continuum or pure particle based methods [25] have motivated the development of mixed continuum-particle formulations [39][29]. The most widely used mixed method is a coupled particle-finite element technique [43]. This technique initializes distinct material regions with either SPH particles or Lagrangian finite elements, or maps failed elements into particles, then quantifies subsequent material interactions using a particle-to-surface contact-impact algorithm.

In recent research an alternative mixed method has been developed, one based on a hybrid particle-finite element interpolation [74]. This method avoids some well known stability problems with SPH techniques, eliminates the requirement for special treatment of particle-to-surface contact-impact, and avoids the mass and energy discard associated with Lagrangian element erosion algorithms. It introduces both elements and particles in all material regions, then employs the elements and particles to represent distinct physics. The particles model all inertia, contact-impact, and thermomechanical response in compressed states, while the elements model tension and elastic-plastic shear. The resulting formulation combines a true Lagrangian description of material strength effects with a general particle based model of contact-impact dynamics, and has been validated in simulations of impact experiments conducted at velocities ranging from one to ten kilometers per second [32]. In the hypervelocity impact regime, where large strain plasticity, perforation, fragmentation, melting, and multi-structure contact-impact effects are often present, this formulation provides a particular combination of advantageous features not offered by alternative numerical methods.

The present work describes an improved hybrid particle-finite element formulation, extending the work of Shivarama and Fahrenthold [74]. In particular it eliminates the use of density interpolation kernels, simplifying the method and reducing the computational cost of the particle dependent calculations. Here the density distribution is obtained, not from a moving interpolation, but by the integration of density evolution equations, the latter developed by direct reference to large deformation kinematics. In the terminology of the energy based modeling approach used here, the density state variables are determined by nonholonomic constraints imposed on the system level thermomechanical model. This avoids the requirement to specify the functional dependence of an interaction potential on the particle coordinates, a task which has proven to be quite difficult in an SPH context and which is a principal focus of the particle dynamics literature.

An additional advantage of the present method is its simple, energy and momentum conserving accommodation of a time or orientation dependent particle contact distance. The present work employs both an orientation dependent (ellipsoidal) and time varying contact distance and as a result can represent large density variations with relatively small neighbor counts. In alternative methods based on density interpolation kernels, the chosen kernels define both the contact distance and the particle interaction potential. As a result the evolution of complex kernels has proven difficult [72][63], and SPH methods normally represent high densities using a fixed contact length and relatively large neighbor sets.

The present chapter is organized as follows. In sections 4.2 and 4.3 the particle and element kinematics are defined, followed by the kinetic co-energy and thermomechanical potential energy functions for the particle-element system. In sections 4.4 and 4.5 the evolution equations for the density are developed, followed by the evolution equations for the plastic and damage variables, all of these relations representing nonholonomic constraints on the system level model. In sections 4.6 and 4.7 the numerical viscosity and numerical heat diffusion models are introduced, and evolution equations for the entropy state variables are described, the latter states serving as generalized coordinates in a thermomechanical Lagrangian formulation. In section 4.8 the discrete Lagrange equations for the particle-element system are derived, taking an explicit state space form convenient for numerical implementation. In section 4.9 application of the method is illustrated in three dimensional simulations which show good agreement with the results of published hypervelocity impact experiments. Finally, in section 4.10 conclusions are presented.

4.3 Kinematics

4.3.1 Particle Kinematics

The inertia of the modeled system is represented by a collection of n ellipsoidal particles, with $m^{(i)}$ the mass of particle i and $h_1^{(i)}, h_2^{(i)}, h_3^{(i)}$ the half-lengths of its major axes. The position and orientation of each particle is determined by its center of mass position vector ($\mathbf{c}^{(i)}$) and an Euler parameter [8][67] vector ($\mathbf{e}^{(i)}$)

$$\mathbf{c}^{(i)} = [\, c_1^{(i)}\; c_2^{(i)}\; c_3^{(i)} \,]^T, \qquad \mathbf{e}^{(i)} = [\, e_0^{(i)}\; e_1^{(i)}\; e_2^{(i)}\; e_3^{(i)} \,]^T \tag{4.1}$$

where a superscript T denotes the transpose. The four parameters $e_0^{(i)}$, $e_1^{(i)}$, $e_2^{(i)}$, and $e_3^{(i)}$ describe a finite rotation about an arbitrary axis.

It is convenient to note here certain properties of Euler parameters, and to cite a number of well known [8] kinematic relations associated with their use. The Euler parameters provide a singularity free description of arbitrary particle rotations. They define a rotation matrix ($\mathbf{R}^{(i)}$) for each particle

$$\mathbf{R}^{(i)} = \mathbf{A}^{(i)}\, \mathbf{G}^{(i)T} \tag{4.2}$$

where

$$\mathbf{A}^{(i)} = \begin{bmatrix} -e_1^{(i)} & e_0^{(i)} & -e_3^{(i)} & e_2^{(i)} \\ -e_2^{(i)} & e_3^{(i)} & e_0^{(i)} & -e_1^{(i)} \\ -e_3^{(i)} & -e_2^{(i)} & e_1^{(i)} & e_0^{(i)} \end{bmatrix} \tag{4.3}$$

and

$$\mathbf{G}^{(i)} = \begin{bmatrix} -e_1^{(i)} & e_0^{(i)} & e_3^{(i)} & -e_2^{(i)} \\ -e_2^{(i)} & -e_3^{(i)} & e_0^{(i)} & e_1^{(i)} \\ -e_3^{(i)} & e_2^{(i)} & -e_1^{(i)} & e_0^{(i)} \end{bmatrix} \tag{4.4}$$

which relates vector components $\mathbf{v}$ described in a fixed global Cartesian coordinate system to corresponding components $\hat{\mathbf{v}}$ described in a co-rotating system aligned with the particle major axes, using

$$\mathbf{v} = \mathbf{R}^{(i)}\, \hat{\mathbf{v}} \tag{4.5}$$

The Euler parameters and their time derivatives are related to the angular velocity vector of the particle ($\boldsymbol{\omega}^{(i)}$), described in the co-rotating frame, by

$$\dot{\mathbf{e}}^{(i)} = \frac{1}{2}\, \mathbf{G}^{(i)T}\, \boldsymbol{\omega}^{(i)} \tag{4.6}$$

Similarly the antisymmetric matrix $\boldsymbol{\Omega}^{(i)}$ with axial vector $\boldsymbol{\omega}^{(i)}$, which satisfies

$$\boldsymbol{\Omega}^{(i)}\mathbf{v} = \boldsymbol{\omega}^{(i)} \times \mathbf{v} \tag{4.7}$$

for all vectors $\mathbf{v}$, is related to the Euler parameters and their time derivatives by the relations

$$\boldsymbol{\Omega}^{(i)} = 2\, \mathbf{G}^{(i)}\, \dot{\mathbf{G}}^{(i)T} = -2\, \dot{\mathbf{G}}^{(i)}\mathbf{G}^{(i)T} = \mathbf{R}^{(i)T}\, \dot{\mathbf{R}}^{(i)} \tag{4.8}$$

As noted in the last section, for ellipsoidal particles the particle separation distance at initial contact is orientation dependent. Hence it is convenient to describe the separation distance of the mass centers for particles i and j using the ellipsoidal coordinate

$$\zeta^{(i,j)} \quad = \quad \left[\left(\mathbf{c}^{(i)} - \mathbf{c}^{(j)}\right)^T \hat{\mathbf{H}}^{(j)} \left(\mathbf{c}^{(i)} - \mathbf{c}^{(j)}\right) \right]^{\frac{1}{2}} \tag{4.9}$$

defined in the co-rotating system of particle j using

$$\hat{\mathbf{H}}^{(j)} = \mathbf{R}^{(j)}\mathbf{H}^{(j)}\mathbf{R}^{(j)T} \tag{4.10}$$

with

$$\mathbf{H}^{(j)} = \begin{bmatrix} 2\beta h_1^{(j)} & 0 & 0 \\ 0 & 2\beta h_2^{(j)} & 0 \\ 0 & 0 & 2\beta h_3^{(j)} \end{bmatrix}^{-2} \tag{4.11}$$

where the constant β allows for close packing at the reference density. The time derivative of this ellipsoidal coordinate , defined for $i \neq j$, is

$$\dot{\zeta}^{(i,j)} = \frac{1}{\zeta^{(i,j)}} \left[\left(\hat{\mathbf{H}}^{(j)} \mathbf{r}^{(i,j)} \right)^T \dot{\mathbf{r}}^{(i,j)} + \left(\mathbf{H}^{(j)} \hat{\mathbf{r}}^{(i,j)} \times \hat{\mathbf{r}}^{(i,j)} \right)^T \boldsymbol{\omega}^{(j)} \right] \tag{4.12}$$

where

$$\mathbf{r}^{(i,j)} = \mathbf{c}^{(i)} - \mathbf{c}^{(j)}, \qquad \hat{\mathbf{r}}^{(i,j)} = \mathbf{R}^{(j)T} \mathbf{r}^{(i,j)} \tag{4.13}$$

and may be used to quantify the rate of compression for an array of ellipsoidal particles.

The preceding results will be used in later sections to account for rotational inertia and orientation dependent contact-impact effects not present in the vast majority of particle models, which assume a spherical particle geometry.

4.3.2 Finite Element Kinematics

This section describes the finite element kinematics employed in the present chapter. The elements used here are eight noded hexahedra, well known and described in detail by Hallquist [37] and others. Since all inertia effects are represented by the particles, no mass matrix is defined.

Each structure in the model is subdivided into uniform hexahedra with orthogonal faces, with ellipsoidal particles located at each node and at the centroid of each element. The center of mass coordinates for particles located at element vertices are also nodal coordinates for the hexahedra, and are used to compute the shearing strain. The center of mass coordinates for particles located at the element centroid are used, in combination with the nodal coordinates, to define six subelements for each hexahedron. The volumes of these subelements are used to compute interparticle tension forces.

The following Lagrangian finite strain deformation measures [52] are used in the stored energy functions for the elements, associated with tension and shear, and in the plastic constitutive relations. The shear strain for element j is

$$\overline{\mathbf{E}}^{(j)} = \frac{1}{2}\left(\overline{\mathbf{C}}^{(j)} - \mathbf{I}\right) \tag{4.14}$$

where

$$\overline{\mathbf{C}}^{(j)} = \overline{\mathbf{F}}^{(j)T}\overline{\mathbf{F}}^{(j)}, \qquad \overline{\mathbf{F}}^{(j)} = \left(det\,\mathbf{F}^{(j)}\right)^{-\frac{1}{3}}\mathbf{F}^{(j)} \tag{4.15}$$

and $\mathbf{F}^{(j)}$ is an element deformation gradient computed using one point integration [37]. The elastic shear strain is defined as

$$\mathbf{E}^{e(j)} = \overline{\mathbf{E}}^{(j)} - \mathbf{E}^{p(j)} \tag{4.16}$$

where $(\mathbf{E}^{p(j)})$ is a plastic stain tensor whose flow rule satisfies the isochoric plastic deformation constraint

$$tr\left(\mathbf{C}^{p(j)^{-T}}\dot{\mathbf{C}}^{p(j)}\right) = 0, \qquad \mathbf{E}^{p(j)} = \frac{1}{2}\left(\mathbf{C}^{p(j)} - \mathbf{I}\right) \tag{4.17}$$

The subelement Jacobians are denoted by $J^{(j,k)}$, where the index k designates one of six subelements for the jth hexahedron.

4.4 Kinematic Co-energy and Potential Energy

An energy method (Lagrange's equations) is adopted here, to facilitate the systematic integration of diverse particle and element based modeling concepts. The stored energy functions considered here are a kinetic co-energy function for the particles, an internal energy function for the particles, and element potential energy functions which account for tension and shear. Damage variables are introduced to model element failure in a thermodynamically consistent fashion. Constitutive assumptions different from those adopted here may be introduced without change to the underlying methodology.

The system kinetic co-energy is the sum of the particle co-energies

$$T^* \;=\; \sum_{i\,=\,1}^{n} T^{*(i)} \tag{4.18}$$

where $T^{*(i)}$ is the co-energy for particle i, due to translation and rotation

$$T^{*(i)} = \frac{1}{2}\, m^{(i)}\, \dot{\mathbf{c}}^{(i)\,T} \dot{\mathbf{c}}^{(i)} \;+\; \frac{1}{2}\, \boldsymbol{\omega}^{(i)\,T}\, \mathbf{J}^{(i)}\, \boldsymbol{\omega}^{(i)} \tag{4.19}$$

with $\mathbf{J}^{(i)}$ a constant moment of inertia matrix described in the co-rotating particle frame. The system kinetic co-energy function defines the generalized momenta

$$\mathbf{p}^{(i)} = \frac{\partial T^*}{\partial \dot{\mathbf{c}}^{(i)}} = m^{(i)}\, \dot{\mathbf{c}}^{(i)}\,, \qquad\qquad \mathbf{h}^{(i)} = \frac{\partial T^*}{\partial \boldsymbol{\omega}^{(i)}} = \mathbf{J}^{(i)}\, \boldsymbol{\omega}^{(i)} \tag{4.20}$$

where $\mathbf{p}^{(i)}$ and $\mathbf{h}^{(i)}$ are translational and angular momentum vectors for the ith particle.

The system potential energy has the general form

$$V = \sum_{i=1}^{n} m^{(i)}\, u^{(i)} \left(\rho^{(i)}, s^{(i)}\right) + \sum_{j=1}^{n_e} V_o^{e(j)}\, \psi^{(j)} + \sum_{j=1}^{n_e} \sum_{k=1}^{n_s} V_o^{e(j,k)}\, \psi^{(j,k)} \tag{4.21}$$

The first term depends on the particle internal energy per unit mass ($u^{(i)}$), density ($\rho^{(i)}$), and entropy density ($s^{(i)}$)

$$s^{(i)} = \frac{S^{(i)}}{m^{(i)}} \tag{4.22}$$

where $S^{(i)}$ is a total particle entropy and any thermodynamically consistent functional form, including tabular data [53], may be introduced for the equation of state. In the formulation, two scalar damage variables 'D' and 'd' are used to model the stiffness degradation and loss of cohesive strength of the material, in tension and shear respectively. The second term depends on the number of elements (n_e), the reference volume ($V_o^{e(j)}$) for element j, and the strain energy per unit volume in shear ($\psi^{(j)}$), here assumed to be

$$\psi^{(j)} = (1 - d^{(j)})\, \mu^{(j)}\, tr\left(\mathbf{E}^{e(j)^T} \mathbf{E}^{e(j)}\right) \tag{4.23}$$

where $d^{(j)}$ is a shear damage variable and $\mu^{(j)}$ is a shear modulus. The third term depends on the number of subelements per element (n_s), the subelement reference volumes ($V_o^{e(j,k)}$), and the strain energy per unit volume in tension ($\psi^{(j,k)}$), here assumed to be

$$\psi^{(j,k)} = \frac{1}{2}\, (1 - D^{(j)})\, K^{(j)}\, < J^{(j,k)} - 1 >^2 \tag{4.24}$$

where $D^{(j)}$ is a normal damage variable, $K^{(j)}$ is a bulk modulus, $< x >$ denotes the bracket function

$$< x > = \; x\, \hat{u}(x) \tag{4.25}$$

and $\hat{u}$ denotes the unit step function. Since the subelement Jacobians and the shear strain tensor depend on the particle center of mass coordinates

$$J^{(j,k)} = J^{(j,k)} \left(\mathbf{c}^{(i)} \right) \tag{4.26}$$

and

$$\mathbf{E}^{e(j)} = \overline{\mathbf{E}}^{(j)} - \mathbf{E}^{p(j)} \tag{4.27}$$

since

$$\overline{\mathbf{E}} = \overline{\mathbf{E}}^{(j)} \left(\mathbf{c}^{(i)} \right) \tag{4.28}$$

it follows that

$$\mathbf{E}^{e(j)} = \mathbf{E}^{e(j)} \left(\mathbf{c}^{(i)}, \mathbf{E}^{p(j)} \right) \tag{4.29}$$

It follows that the system potential energy has the general functional form

$$V = V \left(\rho^{(i)}, S^{(i)}, \mathbf{c}^{(i)}, d^{(j)}, D^{(j)}, \mathbf{E}^{p(j)} \right) \tag{4.30}$$

The system potential energy defines the generalized conservative forces

$$m^{(i)} \frac{P^{(i)}}{\rho^{(i)2}} = \frac{\partial V}{\partial \rho^{(i)}}, \qquad \mathbf{g}^{(i)} = \frac{\partial V}{\partial \mathbf{c}^{(i)}}, \qquad \theta^{(i)} = \frac{\partial V}{\partial S^{(i)}} \tag{4.31}$$

where $P^{(i)}$ and $\theta^{(i)}$ are the thermodynamic pressure and temperature, as well as the deviatoric stress

$$\mathbf{S}^{(j)} = -\frac{1}{V_o^{e(j)}} \frac{\partial V}{\partial \mathbf{E}^{p(j)}} \tag{4.32}$$

and the strain energy release rates

$$\Gamma^{D(j)} = -\frac{\partial V}{\partial D^{(j)}}, \qquad \Gamma^{d(j)} = -\frac{\partial V}{\partial d^{(j)}} \tag{4.33}$$

associated with damage evolution.

With the system Lagrangian now defined, the next four sections describe evolution equations for the internal state variables.

4.5 Density Evolution Relations

The density evolution relations are obtained by noting that for uniform compression of ellipsoidal particles, arranged in the packing scheme previously described, the density satisfies

$$\frac{\rho}{\rho_o} \sim \frac{1}{\zeta^3} \tag{4.34}$$

where ρ_o is a reference density. It follows that in general

$$\frac{\dot{\rho}^{(i)}}{{\rho_o}^{(i)}} = -\frac{3}{8} \sum_{j=1}^{n} \frac{\dot{\zeta}^{(i,j)}}{\zeta^{(i,j)4}} \, W^{(i,j)} \tag{4.35}$$

where the factor of $\frac{1}{8}$ is due to the presence of eight nearest neighbors in the reference configuration (Figure 4.1). The coefficient $W^{(i,j)}$ reduces the contact distance as the local density increases (Figure 4.2)

$$W^{(i,j)} = (1 - \delta_{ij})\, \hat{u} \left(1 - \zeta^{(i,j)} \left[\frac{\rho^{(i)}}{{\rho_o}^{(i)}} \right]^{1/3} \right) \tag{4.36}$$

while the Kronecker delta δ_{ij} excludes from the sum the term for which $i = j$. Note that $W^{(i,j)}$ is a step function which allows for interaction with near neighbors only, and performs no interpolation. Introducing the kinematic relation for $\dot{\zeta}^{(i,j)}$ (Equation 4.12), developed in an earlier section, yields

$$\dot{\rho}^{(i)} = -\frac{3}{8} \sum_{j\,=\,1}^{n} {\rho_o}^{(i)} \frac{W^{(i,j)}}{\zeta^{(i,j)5}} \left[\left(\hat{\mathbf{H}}^{(j)} \mathbf{r}^{(i,j)} \right)^T \dot{\mathbf{r}}^{(i,j)} + \left(\mathbf{H}^{(j)} \hat{\mathbf{r}}^{(i,j)} \times \hat{\mathbf{r}}^{(i,j)} \right)^T \boldsymbol{\omega}^{(j)} \right] \tag{4.37}$$

which is the constraint form of the density evolution relations. The coefficients of the particle translational velocities and angular velocities in this expression will determine generalized forces in the momentum balance (Lagrange) equations derived in a later section. When the particle velocities in this expression are eliminated in favor of the particle momenta

$$\dot{\mathbf{c}}^{(i)} = m^{(i)-1} \mathbf{p}^{(i)}, \qquad \boldsymbol{\omega}^{(i)} = \mathbf{J}^{(i)-1} \mathbf{h}^{(i)} \tag{4.38}$$

the density evolution equations take an explicit state space form convenient for use in numerical simulation.

4.6 Plasticity and Damage Models

This section introduces evolution equations for the plastic and damage variables. As in the case of the potential energy, alternative constitutive assumptions may be introduced without change to the basic modeling methodology. The plastic flow rule used here is adapted from reference [27], and represents the simplest possible accommodation of the aforementioned isochoric plastic deformation constraint. The flow rule is

$$\dot{\mathbf{E}}^{p(j)} = \frac{\dot{\lambda}^{(j)}}{||S^{p(j)}||} \underline{\underline{\mathbf{N}}}^{p(j)} \, \underline{\underline{\mathbf{N}}} \, \mathbf{S}^{p(j)} \tag{4.39}$$

where $\dot{\lambda}^{(j)}$ is a positive proportionality coefficient, $\mathbf{S}^{p(j)}$ is an effective deviatoric stress, the stress which appears in the yield condition and flow rule. It is defined by

$$\mathbf{S}^{p(j)} = \underline{\underline{\mathbf{N}}}^{T} \, \underline{\underline{\mathbf{N}}}^{p(j)T} \, \mathbf{S}^{(j)} \tag{4.40}$$

and the invariant operator is defined by

$$||\mathbf{T}|| = \left[\frac{1}{2} \, tr \left(\mathbf{T}^{T}\mathbf{T}\right)\right]^{1/2} \tag{4.41}$$

for any second order tensor $\mathbf{T}$. The fourth order tensor operators in the flow rule are defined by

$$\underline{\underline{\mathbf{N}}}^{p(j)} \, \mathbf{T} = \frac{1}{2 \, ||C^{p(j)}||} (\mathbf{C}^{p(j)} \, \mathbf{T} + \mathbf{T} \, \mathbf{C}^{p(j)}) \tag{4.42}$$

$$\underline{\underline{\mathbf{N}}} \, \mathbf{T} = \mathbf{T} - \frac{1}{3} tr(\mathbf{T}) \, \mathbf{I} \tag{4.43}$$

for any symmetric second order tensor $\mathbf{T}$. The yield function is

$$f^{(j)} = ||S^{p(j)}|| - Y^{(j)} \tag{4.44}$$

where $Y^{(j)}$ is the yield stress

$$Y^{(j)} = \frac{1}{2}\,(1 - d^{(j)})\,Y_o^{(j)}\,(1 + \kappa^{(j)}\epsilon^{p(j)})^{\alpha^{(j)}}\,\left(1 - \eta^{(j)}\theta^{H(j)}\right) \tag{4.45}$$

with $\epsilon^{p(j)}$ the effective plastic strain, $\kappa^{(j)}$ a strain hardening coefficient, $\alpha^{(j)}$ a strain hardening exponent, $\eta^{(j)}$ a thermal softening coefficient, and $\theta^{H(j)}$ the homologous temperature

$$\theta^H = \frac{\theta - \theta_o}{\theta_m - \theta_o} \tag{4.46}$$

where θ_o and θ_m are reference and melt temperatures. The effective plastic strain is determined by integrating the rate relation

$$\dot{\epsilon}^{p(j)} = ||\dot{\mathbf{E}}^{p(j)}|| \tag{4.47}$$

while the incremental plastic strain for a time step Δt is computed using

$$\Delta\lambda^{(j)} = \frac{< ||S^{p(j)}|| - Y^{(j)} >}{(1 - d^{(j)})\,2\,\mu^{(j)}} \tag{4.48}$$

The damage evolution equations applied here are adapted from reference [75], and dissipate the strain energy stored in tension and shear over $\hat{n}$ time steps, once an element meets any stipulated material failure criteria. The evolution equations are

$$\dot{D}^{(j)} = \frac{\Lambda^{(j)}}{\hat{n}\,\Delta t}\,\hat{u}(1 - D^{(j)}), \qquad \dot{d}^{(j)} = \frac{\Lambda^{(j)}}{\hat{n}\,\Delta t}\,\hat{u}(1 - d^{(j)}) \tag{4.49}$$

where $\Lambda^{(j)}$ is initialized to zero, and is set to a value of one when the accumulated plastic strain, temperature, or element compression reach corresponding critical values for the plastic failure strain ($\epsilon_f^{p(j)}$), melt temperature ($\theta_m^{(j)}$), or maximum compression ($J_c^{(j)}$). Other failure criteria may of course be specified.

In general terms, the plastic and damage evolution equations are nonholonomic constraints of the form

$$\begin{aligned}
\dot{\mathbf{E}}^{p(j)} &= \dot{\mathbf{E}}^{p(j)}\left(\rho^{(i)}, S^{(i)}, \mathbf{c}^{(i)}, d^{(j)}, D^{(j)}, \epsilon^{p(j)}, \mathbf{E}^{p(j)}\right) && (4.50)\\
\dot{d}^{(j)} &= \dot{d}^{(j)}\left(\rho^{(i)}, S^{(i)}, \mathbf{c}^{(i)}, d^{(j)}, D^{(j)}, \epsilon^{p(j)}, \mathbf{E}^{p(j)}\right) && (4.51)\\
\dot{D}^{(j)} &= \dot{D}^{(j)}\left(\rho^{(i)}, S^{(i)}, \mathbf{c}^{(i)}, d^{(j)}, D^{(j)}, \epsilon^{p(j)}, \mathbf{E}^{p(j)}\right) && (4.52)
\end{aligned}$$

on the system level Lagrangian model.

4.7 Artificial Viscosity and Heat Diffusion

Shock physics codes of the continuum or particle type incorporate a numerical viscosity and artificial heat diffusion. A numerical viscosity is used to model shocks and damp the translational and rotational mode of the particles, and an artificial heat diffusion is used to allow heat to diffuse through the material. The forms used here are typical of particle codes, with one exception. Since the ellipsoidal particles used here admit rotational degrees of freedom, a viscous torque has been added which damps the relative rotation of neighboring particles.

A viscous force is introduced for converging particles only

$$\mathbf{f}^{(i)} = \sum_{j=1}^{n} \nu^{(i,j)}\, max\left(0, v^{(i,j)}\right) \frac{\left(\,\mathbf{c}^{(i)} - \mathbf{c}^{(j)}\,\right)}{\mid \mathbf{c}^{(i)} - \mathbf{c}^{(j)} \mid}\; \hat{u}(1 - \zeta^{(i,j)}) \tag{4.53}$$

where the step function, which depends on the ellipsoidal coordinate of equation (4.9), allows for viscous interaction with near neighbors only, and the relative normal velocity is

$$v^{(i,j)} = -\left(\dot{\mathbf{c}}^{(i)} - \dot{\mathbf{c}}^{(j)} \right) \cdot \frac{\left(\mathbf{c}^{(i)} - \mathbf{c}^{(j)} \right)}{\mid \mathbf{c}^{(i)} - \mathbf{c}^{(j)} \mid} \tag{4.54}$$

and the viscosity coefficient [60] is

$$\nu^{(i,j)} = \frac{c_o}{2} \left(\rho_o^{(i)}\, c_s^{(i)} V_o^{(i)\,\frac{2}{3}} + \rho_o^{(j)}\, c_s^{(j)} V_o^{(j)\,\frac{2}{3}} \right) \left[1 + \frac{2\, c_1 |v^{(i,j)}|}{(c_s^{(i)} + c_s^{(j)})} \right] \tag{4.55}$$

with $c_s^{(i)}$ and $V_o^{(i)}$ a soundspeed and particle reference volume. The parameters c_o and c_1 are nondimensional linear and quadratic numerical viscosity coefficients.

Similarly the viscous torque is

$$\mathbf{M}^{(i)} = \sum_{j\,=\,1}^{n} \sigma^{(i,j)}\, \mathbf{R}^{(i)T} \left(\mathbf{R}^{(i)} \boldsymbol{\omega}^{(i)} - \mathbf{R}^{(j)} \boldsymbol{\omega}^{(j)} \right)\, \hat{u}(1 - \zeta^{(i,j)}) \tag{4.56}$$

where the torsional damping coefficient is

$$\sigma^{(i,j)} = \frac{c_o}{2} \left(\rho_o^{(i)}\, c_s^{(i)} V_o^{(i)\,\frac{4}{3}} + \rho_o^{(j)}\, c_s^{(j)} V_o^{(j)\,\frac{4}{3}} \right) \tag{4.57}$$

Finally the thermal power flow due to artificial heat diffusion is taken to be

$$\dot{Q}^{con(i)} = \sum_{j\,=\,1}^{n} R^{(i,j)}\, (\, \theta^{(i)} - \theta^{(j)} \,)\, \hat{u}(1 - \zeta^{(i,j)}) \tag{4.58}$$

where the heat transfer coefficient is

$$R^{(i,j)} = \frac{k_o}{2} \left(\rho_o^{(i)}\, c_s^{(i)} c_v^{(i)} V_o^{(i)\,\frac{2}{3}} + \rho_o^{(j)}\, c_s^{(j)} c_v^{(j)} V_o^{(j)\,\frac{2}{3}} \right) \tag{4.59}$$

with $c_v^{(i)}$ a specific heat and k_o a numerical heat diffusion coefficient.

4.8 Entropy Evolution Equations

The last internal state variable to be considered is the entropy. The introduction of entropy states as generalized coordinates allows the thermomechanical problem of interest here to be solved using energy methods. The entropy evolution equations developed in this section take the place of the energy balance equations which appear in typical weighted residual or finite difference formulations.

The entropy evolution equations for particle i are

$$\dot{S}^{(i)} = \dot{S}^{irr(i)} - \dot{S}^{con(i)} \tag{4.60}$$

where the first term represents irreversible entropy production and the second term represents entropy flow due to heat diffusion.

The irreversible entropy production for particle i depends on the viscous forces and torques, which act on the particles, and on the dissipation in the elements

$$\dot{S}^{irr(i)} = \theta^{(i)-1} \left(\mathbf{f}^{(i)^T} \dot{\mathbf{c}}^{(i)} + \mathbf{M}^{(i)T} \boldsymbol{\omega}^{(i)} + \sum_{j=1}^{n_e} \phi^{(i,j)} \, \dot{Q}^{irr(j)} \right) \tag{4.61}$$

where $\dot{Q}^{irr(j)}$ is a power flow due to damage evolution and plastic deformation in element j

$$\dot{Q}^{irr(j)} = \Gamma^{D(j)} \dot{D}^{(j)} + \Gamma^{d(j)} \dot{d}^{(j)} + V_o^{e(j)} \, tr \left(\mathbf{S}^{(j)T} \dot{\mathbf{E}}^{p(j)} \right) \tag{4.62}$$

and $\phi^{(i,j)}$ is the fraction of the dissipation in element j associated with particle i.

Finally the conduction entropy flows for the particles are obtained by scaling the associated thermal power flows with the particle temperatures

$$\dot{S}^{con(i)} = \theta^{(i)-1}\,\dot{Q}^{con(i)} = \sum_{j\,=\,1}^{n} R^{(i,j)}\,(\,1 - \frac{\theta^{(j)}}{\theta^{(i)}}\,) \tag{4.63}$$

As in the case of the density evolution equations, a constraint form of the entropy evolution relations is used to identify the generalized forces which appear in the Lagrange equations developed in the next section. For numerical implementation of the method, the generalized velocities are eliminated by introducing the momentum states and the plastic and damage evolution relations. The resulting entropy evolution relations take an explicit state space form.

4.9 Lagrange's Equations

The preceding sections defined stored energy functions and nonholonomic constraints for the thermomechanical particle-element system. This section develops the final ODE model. In the interest of brevity this section applies certain results from Shivarama and Fahrenthold [74], which allow in the present case Lagrange's equations to take the canonical form

$$\dot{\mathbf{p}}^{(i)} = -\mathbf{g}^{(i)} + \mathbf{Q}^{c(i)}, \qquad \dot{\mathbf{c}}^{(i)} = m^{(i)-1}\,\mathbf{p}^{(i)} \tag{4.64}$$

$$\dot{\mathbf{h}}^{(i)} = -\boldsymbol{\Omega}^{(i)}\mathbf{h}^{(i)} + \mathbf{Q}^{(i)}, \qquad \dot{\mathbf{e}}^{(i)} = \frac{1}{2}\mathbf{G}^{(i)T}\mathbf{J}^{(i)-1}\mathbf{h}^{(i)} \tag{4.65}$$

$$\frac{\partial V}{\partial \rho^{(i)}} = Q^{\rho(i)}, \qquad \frac{\partial V}{\partial S^{(i)}} = Q^{S(i)} \tag{4.66}$$

$$\frac{\partial V}{\partial d^{(j)}} = Q^{d(j)}, \qquad \frac{\partial V}{\partial D^{(j)}} = Q^{D(j)}, \qquad \frac{\partial V}{\partial \mathbf{E}^{p(j)}} = \mathbf{Q}^{p(j)} \tag{4.67}$$

where $\mathbf{Q}^{c(i)}$, $\mathbf{Q}^{(i)}$, $\mathbf{Q}^{\rho(i)}$, $Q^{S(i)}$, $Q^{d(i)}$, $Q^{D(i)}$, and $\mathbf{Q}^{p(j)}$ are generalized forces determined by the nonholonomic constraints. The degenerate forms of the Lagrange equations for the internal state variables are due to the fact that those variables are not associated with any generalized momenta. Introducing Lagrange multipliers $\gamma^{\rho(i)}$, $\gamma^{S(i)}$, $\gamma^{d(j)}$, $\gamma^{D(j)}$, and $\mathbf{X}^{p(j)}$ for the constraints, the generalized forces are found to be

$$\begin{aligned}\mathbf{Q}^{c(i)} &= -\frac{\gamma^{S(i)}}{\theta^{(i)}}\,\mathbf{f}^{(i)} \\ &\quad +\frac{3}{8}\sum_{j=1}^{n}\left[\gamma^{\rho(i)}\rho_o^{(i)}\frac{W^{(i,j)}}{\zeta^{(i,j)5}}\hat{\mathbf{H}}^{(j)}\mathbf{r}^{(i,j)} - \gamma^{\rho(j)}\rho_o^{(j)}\frac{W^{(j,i)}}{\zeta^{(j,i)5}}\hat{\mathbf{H}}^{(i)}\mathbf{r}^{(j,i)}\right]\end{aligned} \tag{4.68}$$

$$\mathbf{Q}^{(i)} = -\frac{\gamma^{S(i)}}{\theta^{(i)}}\,\mathbf{M}^{(i)} + \frac{3}{8}\sum_{j=1}^{n}\gamma^{\rho(j)}\rho_o^{(j)}\frac{W^{(j,i)}}{\zeta^{(j,i)5}}\left(\mathbf{H}^{(i)}\hat{\mathbf{r}}^{(j,i)} \times \hat{\mathbf{r}}^{(j,i)}\right) \tag{4.69}$$

$$Q^{\rho(i)} = \gamma^{\rho(i)} \tag{4.70}$$

$$Q^{s(i)} = \gamma^{S(i)} \tag{4.71}$$

$$Q^{d(j)} = \gamma^{d(j)} - \sum_{i=1}^{n}\frac{\gamma^{S(i)}}{\theta^{(i)}}\,\phi^{(i,j)}\,\Gamma^{d(j)} \tag{4.72}$$

$$Q^{D(j)} = \gamma^{D(j)} - \sum_{i=1}^{n}\frac{\gamma^{S(i)}}{\theta^{(i)}}\,\phi^{(i,j)}\,\Gamma^{D(j)} \tag{4.73}$$

$$\mathbf{Q}^{p(j)} = \mathbf{X}^{p(j)} - \sum_{i=1}^{n}\frac{\gamma^{S(i)}}{\theta^{(i)}}\,\phi^{(i,j)}\,V_o^{(j)}\,\mathbf{S}^{(j)} \tag{4.74}$$

These results allow the unknown Lagrange multipliers to be determined in closed form, so that the final Lagrange equations are

$$\begin{aligned} \dot{\mathbf{p}}^{(i)} &= -\mathbf{g}^{(i)} - \mathbf{f}^{(i)} + \mathbf{q}^{c(i)} & (4.75) \\ \dot{\mathbf{h}}^{(i)} &= -\mathbf{\Omega}^{(i)}\mathbf{h}^{(i)} - \mathbf{M}^{(i)} + \mathbf{q}^{(i)} & (4.76) \\ \dot{\mathbf{c}}^{(i)} &= m^{(i)-1}\,\mathbf{p}^{(i)} & (4.77) \\ \dot{\mathbf{e}}^{(i)} &= \frac{1}{2}\mathbf{G}^{(i)T}\mathbf{J}^{(i)-1}\mathbf{h}^{(i)} & (4.78) \end{aligned}$$

where the generalized forces and torques due to particle interactions are

$$\mathbf{q}^{c(i)} = \frac{3}{8}\sum_{j\,=\,1}^{n}\left(\rho_o^{(i)}\,m^{(i)}\,\frac{P^{(i)}}{\rho^{(i)2}}\,\frac{W^{(i,j)}}{\zeta^{(i,j)5}}\,\hat{\mathbf{H}}^{(j)} + \rho_o^{(j)}\,m^{(j)}\,\frac{P^{(j)}}{\rho^{(j)2}}\,\frac{W^{(j,i)}}{\zeta^{(j,i)5}}\,\hat{\mathbf{H}}^{(i)}\right)\,\mathbf{r}^{(i,j)} \tag{4.79}$$

$$\mathbf{q}^{(i)} = \frac{3}{8}\sum_{j\,=\,1}^{n}\rho_o^{(j)}\,m^{(j)}\,\frac{P^{(j)}}{\rho^{(j)2}}\,\frac{W^{(j,i)}}{\zeta^{(j,i)5}}\left(\mathbf{H}^{(i)}\hat{\mathbf{r}}^{(j,i)} \times \hat{\mathbf{r}}^{(j,i)}\right) \tag{4.80}$$

supplemented by the evolution equations for density, entropy, shear damage, normal damage, and plastic strain, the result is an explicit first order ODE model for the thermomechanical particle-element system.

4.10 Final explicit first order ODE

$$\dot{\mathbf{p}}^{(i)} = -\mathbf{g}^{(i)} - \mathbf{f}^{(i)} + \mathbf{q}^{c(i)} \tag{4.81}$$

$$\dot{\mathbf{h}}^{(i)} = -\boldsymbol{\Omega}^{(i)}\mathbf{h}^{(i)} - \mathbf{M}^{(i)} + \mathbf{q}^{(i)} \tag{4.82}$$

$$\dot{\mathbf{c}}^{(i)} = m^{(i)-1}\,\mathbf{p}^{(i)} \tag{4.83}$$

$$\dot{\mathbf{e}}^{(i)} = \frac{1}{2}\mathbf{G}^{(i)T}\mathbf{J}^{(i)-1}\mathbf{h}^{(i)} \tag{4.84}$$

$$\begin{aligned}\dot{\rho}^{(i)} = {} & -\frac{3}{8}\sum_{j\,=\,1}^{n} {\rho_o}^{(i)}\frac{W^{(i,j)}}{\zeta^{(i,j)5}} \\ & \left[\,\left(\hat{\mathbf{H}}^{(j)}\mathbf{r}^{(i,j)}\right)^{T}\dot{\mathbf{r}}^{(i,j)} + \left(\mathbf{H}^{(j)}\hat{\mathbf{r}}^{(i,j)} \times \hat{\mathbf{r}}^{(i,j)}\right)^{T}\boldsymbol{\omega}^{(j)}\,\right]\end{aligned} \tag{4.85}$$

$$\dot{S}^{(i)} = \dot{S}^{irr(i)} - \dot{S}^{con(i)} \tag{4.86}$$

$$\dot{d}^{(j)} = \frac{\Lambda^{(j)}}{\hat{n}\,\Delta t}\,\hat{u}(1-d^{(j)}) \tag{4.87}$$

$$\dot{D}^{(j)} = \frac{\Lambda^{(j)}}{\hat{n}\,\Delta t}\,\hat{u}(1-D^{(j)}) \tag{4.88}$$

$$\dot{\mathbf{E}}^{p(j)} = \frac{\dot{\lambda}^{(j)}}{||S^{p(j)}||}\,\underline{\underline{\mathbf{N}}}^{p(j)}\,\underline{\underline{\mathbf{N}}}\,\mathbf{S}^{p(j)} \tag{4.89}$$

where

$$\begin{aligned}\mathbf{g}^{(i)} = {} & \sum_{j=1}^{ne}\kappa^{(j)}{V_0}^{(j)}\left(J^{(j)}-1\right)H\left[J^{(j)}-1\right]\frac{\partial J^{(j)}}{\partial\mathbf{c}^{(i)}} \\ & +\sum_{j=1}^{ne}2\mu^{(j)}{V_0}^{(j)}\mathbf{E}^{(j)} : \frac{\partial\mathbf{E}^{(j)}}{\partial\mathbf{c}^{(i)}}\end{aligned} \tag{4.90}$$

$$\mathbf{f}^{(i)} = \sum_{j\,=\,1}^{n}\nu^{(i,j)}\,max\left(0, v^{(i,j)}\right)\,\frac{\left(\,\mathbf{c}^{(i)}-\mathbf{c}^{(j)}\,\right)}{|\,\mathbf{c}^{(i)}-\mathbf{c}^{(j)}\,|}\;\hat{u}(1-\zeta^{(i,j)}) \tag{4.91}$$

and

$$\mathbf{\Omega}^{(i)} = 2\,\mathbf{G}^{(i)}\,\dot{\mathbf{G}}^{(i)T} = -2\,\dot{\mathbf{G}}^{(i)}\mathbf{G}^{(i)T} \tag{4.92}$$

$$\mathbf{M}^{(i)} = \sum_{j\,=\,1}^{n} \sigma^{(i,j)}\,\mathbf{R}^{(i)T}\,\left(\mathbf{R}^{(i)}\boldsymbol{\omega}^{(i)} - \mathbf{R}^{(j)}\boldsymbol{\omega}^{(j)}\right)\,\hat{u}(1-\zeta^{(i,j)}) \tag{4.93}$$

and where the generalized forces and torques due to particle interactions are

$$\mathbf{q}^{c(i)} = \frac{3}{8}\sum_{j\,=\,1}^{n}\left(\rho_o^{(i)}\,m^{(i)}\,\frac{P^{(i)}}{\rho^{(i)2}}\,\frac{W^{(i,j)}}{\zeta^{(i,j)5}}\,\hat{\mathbf{H}}^{(j)} + \rho_o^{(j)}\,m^{(j)}\,\frac{P^{(j)}}{\rho^{(j)2}}\,\frac{W^{(j,i)}}{\zeta^{(j,i)5}}\,\hat{\mathbf{H}}^{(i)}\right)\,\mathbf{r}^{(i,j)} \tag{4.94}$$

$$\mathbf{q}^{(i)} = \frac{3}{8}\sum_{j\,=\,1}^{n}\rho_o^{(j)}\,m^{(j)}\,\frac{P^{(j)}}{\rho^{(j)2}}\,\frac{W^{(j,i)}}{\zeta^{(j,i)5}}\left(\mathbf{H}^{(i)}\hat{\mathbf{r}}^{(j,i)} \times \hat{\mathbf{r}}^{(j,i)}\right) \tag{4.95}$$

4.11 Example Simulations

This section describes two example simulations performed to illustrate application of the particle-element method developed in this chapter. The example problems involve the oblique impact of tungsten alloy (DX2HCMF) rods on steel (SIS 2541) plates, and model experiments described in references [50] and [48]. The simulations employed a parallel code [26], a Mie-Gruneisen equation of state [76], the material properties [48][76] listed in Table 4.1, and the following artificial viscosity and heat diffusion coefficients

$$c_o = 0.001, \qquad c_1 = 0.0, \qquad k_o = 0.1 \tag{4.96}$$

The cylindrical projectiles have a diameter of 0.5 cm and a length of 7.5 cm (L/D = 15). The first simulation models a 1.5 km/s impact on a 0.5 cm thick plate at a sixty degree obliquity, using 92,498 particles. Figures 4.3 and 4.4 show the initial configuration and the simulation results at 60 microseconds after impact, while Figures 4.5 and 4.6 show sectioned views at 20 and 40 microseconds after impact, with color on temperature. The simulation results for residual rod length (0.626 cm) and residual rod velocity (1.41 km/s) show good agreement with the corresponding experimental values (0.638 cm and 1.46 km/s). The second simulation models a 2.5 km/s impact on a 0.313 cm thick plate at an eighty degree obliquity, using 90,824 particles. Figures 4.7 and 4.8 show the initial configuration and the simulation results at 60 microseconds after impact, while Figures 4.9 and 4.10 show sectioned views at 20 and 40 microseconds after impact, with color on temperature. The simulation results for residual rod length (0.427 cm) and residual rod velocity (2.35 km/s) show good agreement with the corresponding experimental values (0.465 cm and 2.45 km/s).

These simulations illustrate that with the present method all material fragments are retained, and are free to translate and rotate under contact-impact loads.

4.12 Conclusions

The present work has formulated a kernel free particle-finite element method and demonstrated application of the method in three dimensional simulations of published hypervelocity experiments. The method described here avoids the difficult task of formulating accurate and stable kernel functions for use in interpolating the density field and quantifying contact-impact loads. Integration of the state equations derived here involves one loop over the particle neighbor sets, to calculate the particle interaction forces, instead of one loop each to determine the particle density and then the particle interaction forces. The method simply accommodates an orientation and time dependent particle contact distance, while conserving momentum and energy in the nonspherical particle case. Applications work will be focused on the simulation of orbital debris impact effects on spacecraft thermal protection materials [16] in Chapter 5.

NOMENCLATURE

$\mathbf{c}$, center of mass position vector

d, shear damage variable

D, normal damage variable

$\mathbf{e}$, Euler parameter vector

$\overline{\mathbf{E}}$, deviatoric strain tensor

$\mathbf{E}^e$, elastic strain tensor

$\mathbf{E}^p$, plastic strain tensor

$\dot{\varepsilon}$, deviatoric strain rate

$\mathbf{f}$, a viscous force

$\mathbf{F}$, deformation gradient tensor

$\mathbf{h}$, angular momentum vectors

$\mathbf{J}$, a constant moment of inertia

J, element jacobian

m, mass of particles

$\mathbf{M}$, a viscous torque

$\mathbf{N}_e$, number of elements

ε^p, effective plastic strain

$\mathbf{S}$, deviatoric stress tensor

$\mathbf{S}^p$, effective stress tensor

$\mathbf{R}$, rotation matrix

s, entropy density

u, internal energy of particles

v, impact velocity

Y, yield stress

ψ, strain energy density

θ, temperature

ϕ, impact obliquity

ζ, ellipsoidal coordinate

δ_{ij}, Kronecker delta

ρ, density of particles

Material property	Projectile	Target
Reference density, g/cm^3 (lb/ft^3)	17.6 (1098.7)	7.87 (491.3)
Shear modulus, Mbar (Mpsi)	1.45 (21.03)	0.801 (11.6)
Reference yield stress, Mbar (Kpsi)	0.0075 (108.8)	0.0105 (152.3)
Strain hardening coefficient	1.15	0.177
Strain hardening exponent	0.49	0.12
Thermal softening coefficient	1.0	1.0
Melt temperature, deg K (deg F)	1,700 (2600.33)	1,723 (2641.73)
Specific heat, Mbar-cm^3/g-deg K (Btu/lb-deg F)	0.143e-5 (0.0342)	0.448e-5 (0.107)
Plastic failure strain	1.0	1.0

Table 4.1: Material properties used in the simulations

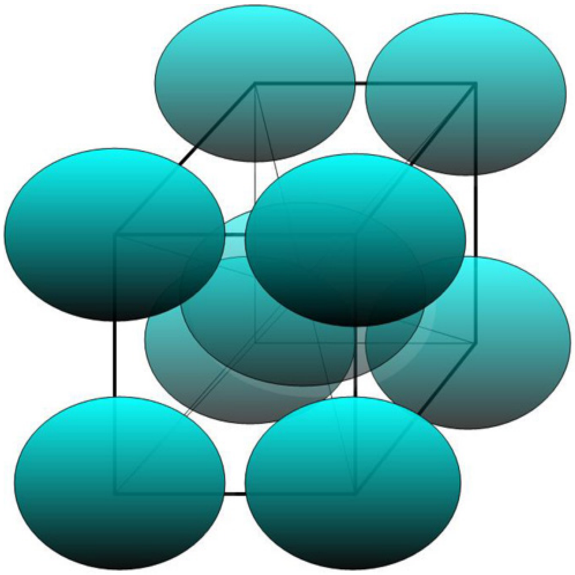

Figure 4.1: Configuration of a unit hexahedral element with 9 nodes

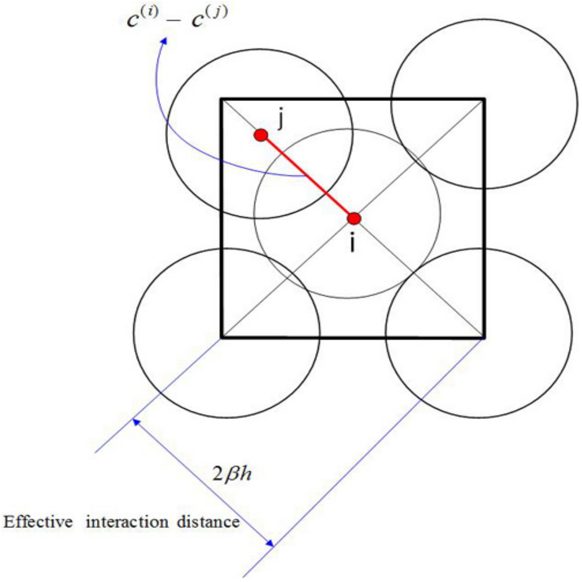

Figure 4.2: 2-D configuration of particle separation and contact distance

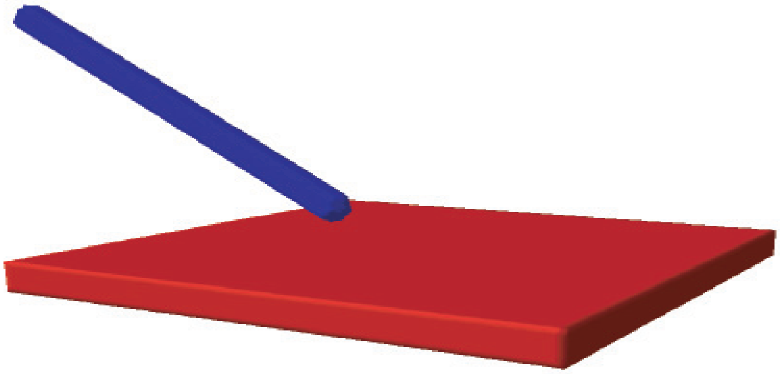

Figure 4.3: Tungsten alloy long rod impact on a steel plate at 1.5 km/s and 60 degree obliquity, element plot of the initial configuration

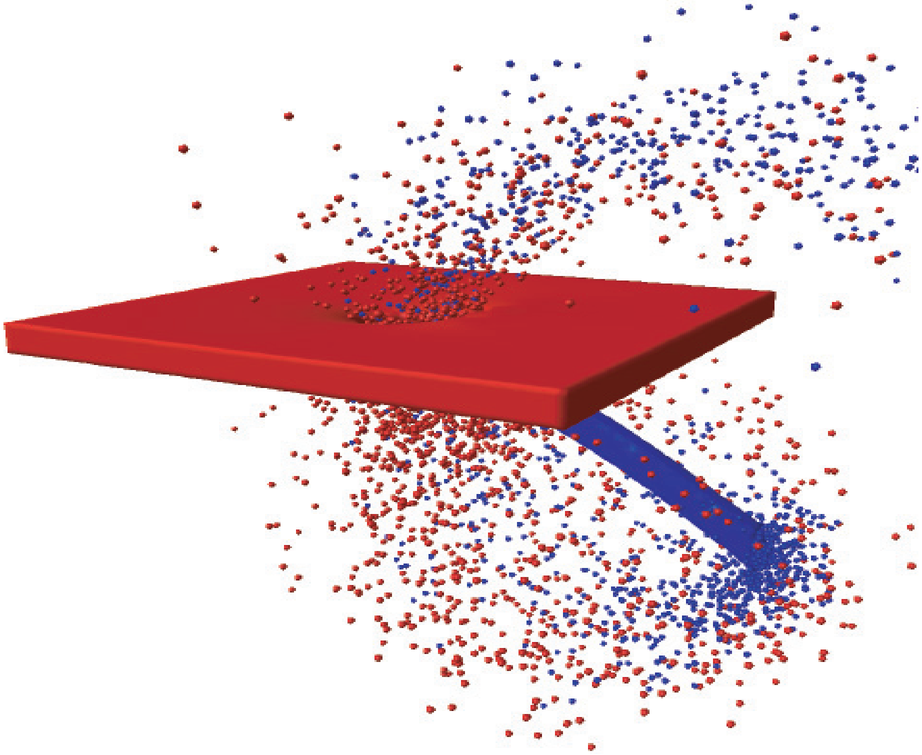

Figure 4.4: Tungsten alloy long rod impact on a steel plate at 1.5 km/s and 60 degree obliquity, particle-element plot at 60 microseconds after impact

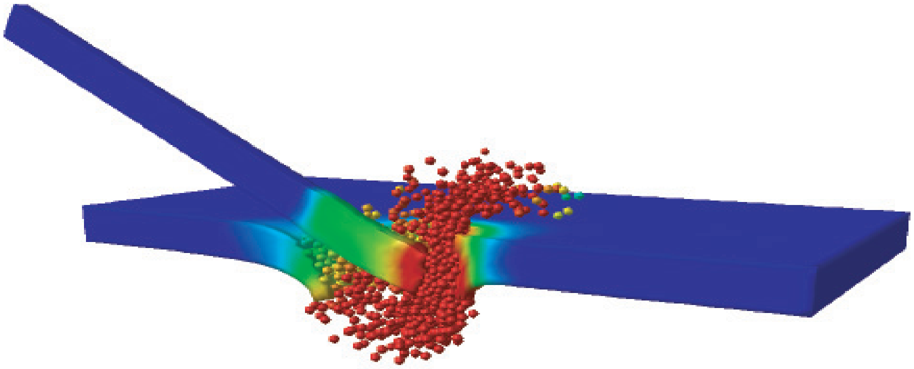

Figure 4.5: Tungsten alloy long rod impact on a steel plate at 1.5 km/s and 60 degree obliquity, sectioned particle-element plot at 20 microseconds after impact with color on temperature

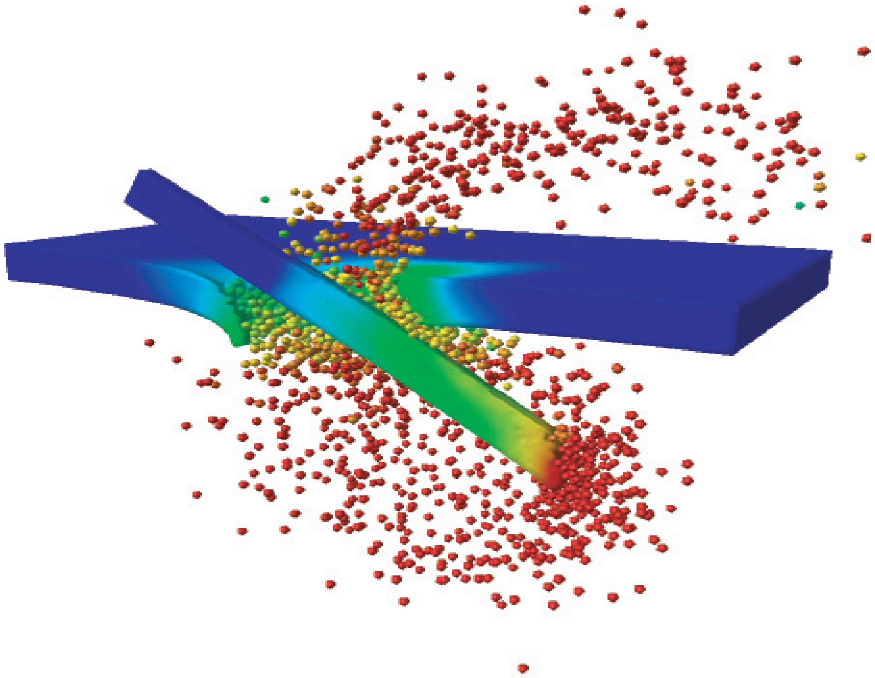

Figure 4.6: Tungsten alloy long rod impact on a steel plate at 1.5 km/s and 60 degree obliquity, sectioned particle-element plot at 40 microseconds after impact with color on temperature

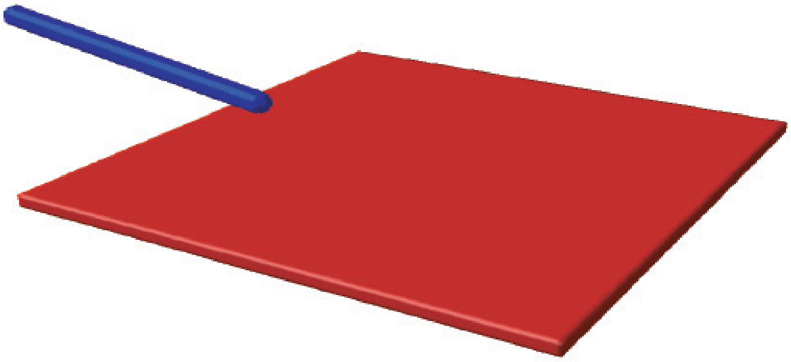

Figure 4.7: Tungsten alloy long rod impact on a steel plate at 2.5 km/s and 80 degree obliquity, element plot of the initial configuration

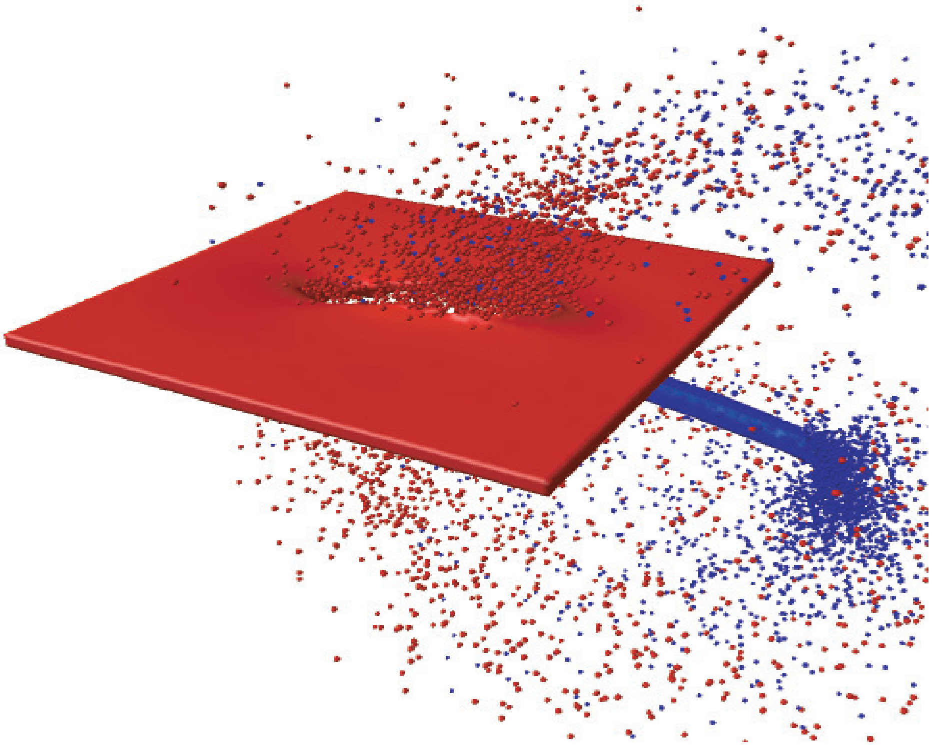

Figure 4.8: Tungsten alloy long rod impact on a steel plate at 2.5 km/s and 80 degree obliquity, particle-element plot at 60 microseconds after impact

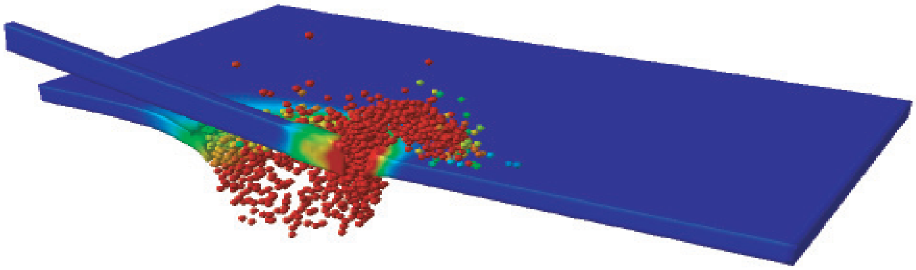

Figure 4.9: Tungsten alloy long rod impact on a steel plate at 2.5 km/s and 80 degree obliquity, sectioned particle-element plot at 20 microseconds after impact with color on temperature

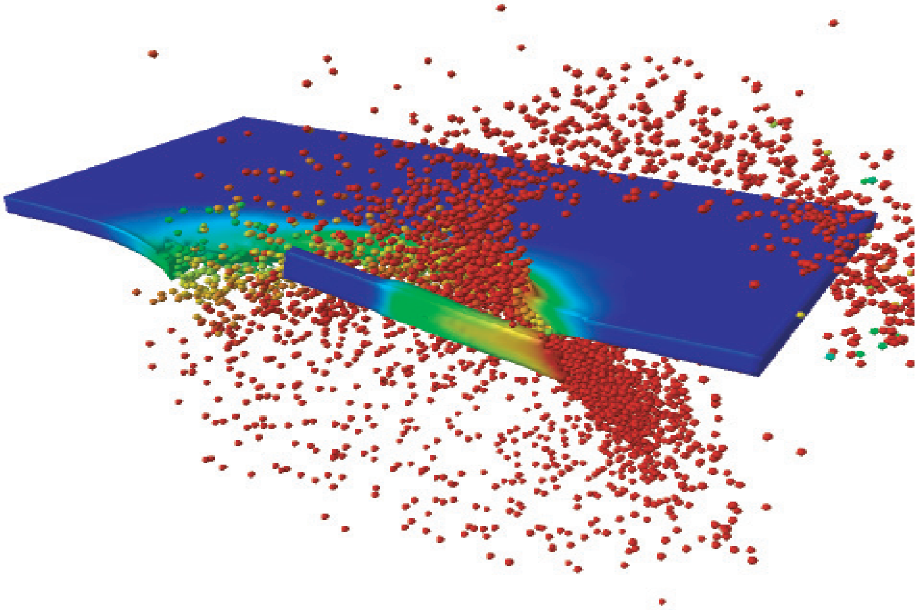

Figure 4.10: Tungsten alloy long rod impact on a steel plate at 2.5 km/s and 80 degree obliquity, sectioned particle-element plot at 40 microseconds after impact with color on temperature

Chapter 5

Simulation of Orbital Debris Impact Effects on Reinforced Carbon-Carbon

5.1 Introduction

Carbon-carbon composites offer an unusual combination of thermal and mechanical properties [82]. Their light weight and high temperature strength satisfy some very stringent design requirements for reusable orbital vehicles [70]. The wing leading edge of the Space Shuttle, subject to severe thermal re-entry loads, is constructed of reinforced carbon-carbon (RCC) panels, coated in silicon carbide to prevent oxidation [68]. Although the thermal properties of RCC composites are well understood [62], much less is known about their dynamic mechanical properties. The loss of the Space Shuttle Columbia [2], apparently due to impact damage on the wing leading edge, has motivated recent experimental [51] and computational [36] work aimed at developing a better understanding of the impact response of thermal protection materials.

The wing leading edge damage to Columbia was unexpected, the result of a relatively low velocity impact by a relatively low density projectile [45]. Another impact damage hazard, due to space debris in low earth orbit, has long been recognized. This threat involves projectiles of very low mass, but much higher density, and impact velocities as high 15 km/s. The debris shielding on the International Space Station is designed to defeat centimeter sized aluminum projectiles. Although the likelihood of such a projectile striking the Space Shuttle is quite low, orbital debris damage by much smaller projectiles is routinely observed during post-mission inspections of the vehicle. As a result previous experimental research has investigated the response of Space Shuttle thermal protection materials to orbital debris impact by spherical aluminum projectiles as large as 0.628 cm in diameter [16].

Due to the high cost of carbon-carbon composites and the long fabrication lead times associated with the preparation of test samples, impact testing of RCC materials has been limited. In addition, the limitations of current experimental technology preclude hypervelocity impact testing over the entire projectile mass and kinetic energy range of interest. As a result, numerical simulation can serve as an important complement to experimental studies of the impact response of RCC materials. Numerical models validated by comparison with experiment at velocities below 8 km/s can be used to extrapolate results into a higher velocity impact regime. The computational work of RCC response to insulating foam impacts described in chapter 2 was extended to projectiles and impact velocities associated with orbital debris impact. In particular it develops a new anisotropic, rate-dependent material model for reinforced carbon-carbon, validates that model in three dimensional simulations of published hypervelocity impact experiments, and applies the validated formulation in simulations of impacts at velocities beyond the experimental range.

The results indicate that a momentum scaling approach used to correlate the available experimental impact data may be extrapolated to describe RCC perforation by hypervelocity projectiles at velocities as high as 13 km/s.

This chapter is organized as follows. Section 5.2 outlines the hybrid particle-finite element method, including the embedded large deformation kinematics and general functional forms for the associated constitutive relations. Section 5.3 discusses published experimental results on the properties of RCC. Section 5.4 develops an RCC constitutive model, formulated for use in hypervelocity impact applications and reflecting important mechanical characteristics described in the material testing literature. Section 5.5 validates and applies the developed model in a series of three dimensional impact simulations. Section 5.6 presents conclusions and suggestions for related future work.

5.2 Numerical Method

The material model described in this chapter was developed for application in a specific numerical framework, the hybrid particle-finite element formulation of references [29] and [74]. In order to provide appropriate context, this section summarizes the latter numerical formulation, details certain element level kinematics, and provides functional forms for the required constitutive relations. The kinematic and constitutive modeling framework assumed here has wide scope, so that the material model described in this chapter may be adapted for use in shock physics codes which are based on alternative numerical modeling schemes [56].

The hybrid particle-finite element model employed here takes an explicit state space form. The state equations consist of evolution equations for the following variables:

- translational and rotational momentum vectors for the three dimensional motion of ellipsoidal particles,

- center of mass position vectors and Euler parameter vectors for the particles, the latter providing a singularity free description of particle rotations,
- density and entropy for each particle, and
- damage and plastic internal state variables for each finite element.

The state equations are derived using a thermomechanical formulation of the Lagrange equations. All inertia effects are modeled using the particles, whose mass centers are also nodal coordinates for the finite elements. The volumetric thermomechanical response of the modeled medium is described by an equation of state for the particles, which may take either an analytic or tabular form.

The material modeling work described in this chapter develops two specific components of the general numerical formulation:

- a strain energy density in shear, one part of the thermomechanical Lagrangian for the modeled particle-element system, and
- a plasticity model which specifies evolution equations for the plastic internal state variables, equations which serve as nonholonomic constraints on the system level model.

The strain energy density in shear takes the general functional form

$$\psi = \psi(d, \mathbf{e}, \overline{\mathbf{E}}, \mathbf{E}^p) \tag{5.1}$$

where d is a shear damage variable, $\overline{\mathbf{E}}$ is the total deviatoric strain, $\mathbf{E}^p$ is the plastic strain, and $\mathbf{e}$ is a vector of Euler parameters which relates the material reference frame for each element to a single global Cartesian reference frame.

The evolution equations for the plastic strain components take the general functional form

$$\dot{\mathbf{E}}^p \quad = \quad \dot{\mathbf{E}}^p(s, d, \varepsilon^p, \dot{\varepsilon}, J, \mathbf{e}, \overline{\mathbf{E}}, \mathbf{E}^p) \tag{5.2}$$

where s is an entropy density, ε^p is the effective plastic strain, $\dot{\varepsilon}$ is a deviatoric strain rate, and

$$J = det(\mathbf{F}) \tag{5.3}$$

where $\mathbf{F}$ is the deformation gradient tensor.

The strain and strain rate variables which appear in the preceding functional forms are defined by the following large deformation kinematics [55]. The deviatoric strain is

$$\overline{\mathbf{E}} = \frac{1}{2}\left(\overline{\mathbf{C}} - \mathbf{I}\right) \tag{5.4}$$

where

$$\overline{\mathbf{C}} = \overline{\mathbf{F}}^T\overline{\mathbf{F}}, \qquad \overline{\mathbf{F}} = (det\,\mathbf{F})^{-\frac{1}{3}}\,\mathbf{F} \tag{5.5}$$

The elastic shear strain is defined as

$$\mathbf{E}^e = \overline{\mathbf{E}} - \mathbf{E}^p \tag{5.6}$$

where the flow rule for the plastic stain tensor must satisfy the isochoric plastic deformation constraint

$$tr\left(\mathbf{C}^{p-T}\dot{\mathbf{C}}^p\right) = 0, \qquad \mathbf{C}^p = \mathbf{I}\, + 2\,\mathbf{E}^p \tag{5.7}$$

The effective plastic strain is determined by integrating the rate relation

$$\dot{\varepsilon}^p = ||\dot{\mathbf{E}}^p|| \tag{5.8}$$

with the indicated invariant operator defined by

$$||\mathbf{T}|| = \left[\frac{1}{2}\, tr\left(\mathbf{T}^T\mathbf{T}\right)\right]^{1/2} \tag{5.9}$$

for any second order tensor $\mathbf{T}$. The deviatoric strain rate is

$$\dot{\varepsilon} = ||\mathbf{D}'||, \qquad \mathbf{D}' = \mathbf{D} - \frac{1}{3}tr(\mathbf{D})\,\mathbf{I} \tag{5.10}$$

where $\mathbf{D}$ is the rate of deformation tensor

$$\mathbf{D} = \frac{1}{2}\left(\mathbf{L} + \mathbf{L}^T\right), \qquad \mathbf{L} = \dot{\mathbf{F}}\,\mathbf{F}^{-1} \tag{5.11}$$

with $\mathbf{L}$ the velocity gradient tensor.

In the case of anisotropic materials, the constitutive response is described in a material reference frame. Here an Euler parameter vector

$$\mathbf{e} = [e_0\; e_1\; e_2\; e_3]^T, \qquad \mathbf{e}^T\mathbf{e} = 1 \tag{5.12}$$

is used to define a rotation matrix ($\mathbf{R}$) for each element

$$\mathbf{R} = \mathbf{A}\,\mathbf{G}^T \tag{5.13}$$

with

$$\mathbf{A} = \begin{bmatrix} -e_1 & e_0 & -e_3 & e_2 \\ -e_2 & e_3 & e_0 & -e_1 \\ -e_3 & -e_2 & e_1 & e_0 \end{bmatrix} \tag{5.14}$$

and

$$\mathbf{G} = \begin{bmatrix} -e_1 & e_0 & e_3 & -e_2 \\ -e_2 & -e_3 & e_0 & e_1 \\ -e_3 & e_2 & -e_1 & e_0 \end{bmatrix} \tag{5.15}$$

which relates a material coordinate system in each element to the global Cartesian system used in the numerical simulations. The rotation matrix relates vector components **p** in the global coordinate system to corresponding components **q** described in the material frame, using

$$\mathbf{p} = \mathbf{R}\,\mathbf{q} \tag{5.16}$$

The corresponding transformation relation for second order tensors is

$$\mathbf{P} = \mathbf{R}\,\mathbf{Q}\,\mathbf{R}^T \tag{5.17}$$

where **P** and **Q** refer respectively to the global and material coordinate systems.

5.3 Reinforced Carbon-Carbon

Carbon-Carbon composites (CCs) have been used in aerospace applications, including in thermal protection materials for the space shuttle. CCs have a lot of exceptional mechanical and thermal properties such as light weight, high strength at high temperatures, high thermal shock resistance, high stiffness, a low thermal expansion, high thermal conductivity, and high fracture toughness [33][22][68][82][12].

Reinforced Carbon-Carbon (RCC) panels manufactured by Lockheed-Martin's Missile and Fire Control Facilities are used as a thermal protection material on the wing leading edges of the space shuttle. Structural strength over the excessive range of temperatures (from 6600^{o}C to -143 ^{o}C) confronted during flight missions is provided by the RCC panels [1][70]. The work of Lu et al. [51], determined some important material characteristics: 1) strain rate dependence of the tensile strength, observing a 15 % increase in strength as the loading rate increased from 1 to 200 sec^{-1}. 2) compressive strength is about double the tensile strength. 3) Aging effect: after 19 missions of the Columbia, ultimate tensile strength was reduced about 15 %. The properties of CCs are dependent on the initial parameters (fiber type, fiber orientation, matrix microstructure, etc.), manufacturing processes and additional treatments [82][33]. CCs have a lot of advantages; however, applications have been limited by some drawbacks shown in the literature [82][6][65][4][47] including: 1) special process requirement, 2) high cost, 3) susceptibility to oxidation, 4) low interlaminar shear strength.

Some notable characteristics of CCs are described in the published literature [82][5][33][12][51]. Structural stability of graphitic carbon affects the mechanical properties of CCs at high temperatures. The mechanical properties of CCs are improved due to annealing of flaws such as microcracks at high temperatures [33]. As a result, the CCs show a 10 - 60 % increment in strength and stiffness at a temperature above 1000 ^{o}C. Oxidation of CCs is a serious problem at high temperatures if not protected [5][12][51]. Therefore, for reliable performance it is necessary to protect the CCs from the oxidation. Silicon carbide coating has been used for oxidation protection at high temperatures because of its thermal expansion compatibility with CCs and low oxidation rate [33]. As an environmental issue, it is necessary to recycle wasted material created during the manufacturing process, however there is no method to recycle CCs [82].

Due to the material cost and proprietary concerns, research on RCC materials have been only briefly described in the published literature. Some papers can be found in the space shuttle impact analysis area. In the work of Christiansen et al. (1997) [16], penetration correlations and ballistic limit equations were developed based on the hypervelocity impact data base. Kerr et al. (2004) [45] conducted foam impact tests on RCC panels using Southwest Research Institute's large compressed gas gun. Gwinn et al. (2004) [36] described an impact analysis with Pronto3D, using a Smooth Particle Hydrodynamics (SPH) technique.

5.4 Material Model

In the case of an orthotropic material, with distinct elastic moduli in tension and compression, the shear strain energy density is

$$\begin{aligned} \psi \;=\; & (1-d)\,\mu_o\,\frac{1}{2}\sum_{i=1}^{3}\mu_{ii}\left[(1+\gamma_i)+(1-\gamma_i)\,sgn(E_{ii}^{em})\right](E_{ii}^{em})^2 + \\ & (1-d)\,\mu_o\sum_{i=1}^{3}\sum_{j=1}^{3}(1-\delta_{ij})\,\mu_{ij}\,(E_{ij}^{em})^2 \end{aligned} \tag{5.18}$$

where δ_{ij} is the Kronecker delta, μ_o is a reference elastic modulus, and the parameters $\mu_{ij} = \mu_{ji}$ are dimensionless constants. The parameters γ_i are the ratios of the elastic moduli in compression to those in tension, while the E_{ij}^{em} are the components of the elastic shearing strain, expressed in a material coordinate system. Note that this function is analytic, since a change in modulus from tension to compression occurs when the corresponding material strain component is zero.

A plastic flow rule for an anisotropic, rate dependent material, which satisfies the aforementioned isochoric plastic deformation constraint, may be obtained by extending the large strain Lagrangian formulation previously developed for use in hypervelocity impact applications [27][30]. The flow rule is

$$\dot{\mathbf{E}}^p = \frac{\dot{\lambda}}{||\mathbf{S}^p||}\,\underline{\underline{\mathbf{N}}}^p\,\underline{\underline{\mathbf{N}}}\,\underline{\underline{\mathbf{M}}}\,\underline{\underline{\mathbf{M}}}^p\,\mathbf{S}^p \tag{5.19}$$

where $\dot{\lambda}$ is a positive proportionality coefficient, $\mathbf{S}^p$ is the effective stress,

$$\mathbf{S}^p = \underline{\underline{\mathbf{M}}}^{pT}\,\underline{\underline{\mathbf{M}}}^{T}\,\underline{\underline{\mathbf{N}}}^{T}\,\underline{\underline{\mathbf{N}}}^{pT}\,\mathbf{S} \tag{5.20}$$

and $\mathbf{S}$ is the deviatoric stress tensor

$$\mathbf{S} = \frac{\partial \psi}{\partial \mathbf{E}^e} \tag{5.21}$$

The first two coefficients in the flow rule impose the isochoric plastic deformation constraint, and are defined by

$$\underline{\underline{\mathbf{N}}}^p\,\mathbf{T} = \frac{1}{2\,||\mathbf{C}^p||}(\mathbf{C}^p\,\mathbf{T} + \mathbf{T}\,\mathbf{C}^p) \tag{5.22}$$

$$\underline{\underline{\mathbf{N}}}\,\mathbf{T} = \mathbf{T} - \frac{1}{3}tr(\mathbf{T})\,\mathbf{I} \tag{5.23}$$

for any symmetric second order tensor $\mathbf{T}$. The third coefficient performs a component transformation from a fixed global to a material reference frame, and is defined by

$$\underline{\underline{\mathbf{M}}}^{T}\,\mathbf{T} = \mathbf{R}^T\,\mathbf{T}\,\mathbf{R} \tag{5.24}$$

for any symmetric second order tensor $\mathbf{T}$. The last coefficient in the flow rule defines an effective stress in a material frame [42], using

$$\underline{\underline{\mathbf{M}}}^{pT}\,\mathbf{P} = \mathbf{Q} \tag{5.25}$$

for symmetric second order tensors **P** and **Q**, with component forms

$$Q_{ii} = \frac{2\,\alpha_{ii}\,P_{ii}}{(1+\beta_{ii}) + (1-\beta_{ii})\;sgn(E^{em}_{ii})} \quad , \qquad i = 1,2,3 \tag{5.26}$$

and

$$Q_{ij} = \frac{2\,\alpha_{ij}\,P_{ij}}{(1+\beta_{ij}) + (1-\beta_{ij})\;sgn(J-1)} \quad , \qquad i \neq j \tag{5.27}$$

The parameter $\alpha_{ij} = \alpha_{ji}$ is the ratio of a reference yield stress to the yield stress for the ijth stress component, while the parameter $\beta_{ij} = \beta_{ji}$ is the ratio of the strength in compression to that in tension for the ijth stress component.

The rate dependent, strain hardening, thermal softening yield function is

$$f = ||\mathbf{S}^p|| - Y \tag{5.28}$$

where Y is the yield stress

$$Y = \frac{1}{2}\,(1-d)\,Y_o\,\left(1-\kappa\,\theta^H\right)\,(1+\eta\,\varepsilon^p)^n\,\left[1+\zeta\,log\left(\frac{\dot{\varepsilon}}{\dot{\varepsilon}_o}\right)\right]^m \tag{5.29}$$

with Y_o the reference yield stress, η a strain hardening coefficient, n a strain hardening exponent, ζ a strain rate hardening coefficient, m a strain rate hardening exponent, $\dot{\varepsilon}_o$ a reference strain rate, κ a thermal softening coefficient, and θ^H the homologous temperature

$$\theta^H = \frac{\theta - \theta_o}{\theta_m - \theta_o} \tag{5.30}$$

where θ_o and θ_m are reference and melt temperatures.

In a numerical implementation, the aforementioned plastic flow rule is expressed in incremental form. The incremental plastic strain at each time step is computed using the incremental proportionality coefficient

$$\Delta\lambda = \frac{< ||\mathbf{S}^p|| - Y >}{(1-d)\, 2\, \mu_o} \tag{5.31}$$

The shear damage variable (d) models the transition from an intact to a failed medium, evolving from an initial value of 0 to a final value of 1 over a fixed number of time steps [75] when any stipulated element failure criterion is satisfied. The simulations discussed in the next section incorporate accumulated plastic strain, melt temperature, and maximum compression failure criteria, although other criteria may be simply accommodated.

5.5 Impact Simulations

The material model just described was applied in a series of three dimensional simulations of hypervelocity impacts on reinforced carbon-carbon. The simulations employed a hybrid particle-finite element method and the material properties listed in Tables 5.1 and 5.2. An initial set of simulations was used to validate the material model, compare results obtained using analytic (Mie-Gruneisen) and tabular equations of state [53], and check numerical convergence of the simulation results. A second series of simulations was then performed to estimate orbital debris impact effects at velocities beyond the range of current experimental methods.

The first set of seven simulations modeled NASA JSC experiments B1028 and B1040 [16], which involved oblique impacts of aluminum spheres on RCC target plates at a velocity of 7 km/s. The target plates were 0.63 cm in thickness, including upper and lower surface coatings composed of silicon carbide, each 0.08 cm in thickness. Table 5.3 lists the experimental parameters, including projectile diameter (d), impact velocity (v), impact obliquity (ϕ, with zero degrees a normal impact), number of elements spanning the target thickness (N_e), and the equation of state used to model the aluminum projectile. Tabular equation of state data was not available for the target materials.

Figures 5.1 through 5.4 show example plots for a simulation of experiment B1028. Figure 5.1 shows the initial configuration while Figures 5.2 through 5.4 show the simulation results at 50 microseconds after impact. The sectioned plot in Figure 5.4 depicts plate perforation and coating spall similar to that observed in the corresponding experiment. Table 5.3 lists the simulation results for the diameter of the RCC perforation (D_p) and the average diameter of the target region over which the silicon carbide coating was removed (D_c). The results of the validation simulations suggest the following conclusions:

- the material model developed here can provide good estimates of both the RCC perforation diameter and the extent of the spalled coating region, for oblique impacts at 7 km/s,
- accurate estimates of the RCC perforation diameter require a mesh resolution sufficient to place 8 elements across the target plate,
- accurate estimates of the diameter of the spalled coating region require a mesh resolution sufficient to place 16 elements across the target plate, and
- the simulation results are not sensitive to the choice of projectile equation of state.

Table 5.4 shows the relative computational cost of simulations of experiment B1028 run at three different mesh densities. As is well known, in three dimensional models the particle count increases with the cube of the increase in resolution, while the time step decreases linearly with the increase in resolution, so that the total computational cost of high resolution models is considerable.

A second set of twelve simulations was performed to investigate orbital debris impact effects at velocities beyond the current experimental range. The simulations involved spherical aluminum projectiles, at three different projectile diameters, an impact obliquity of 30 degrees and impact velocities of 7, 10, and 13 km/s. In the case of the largest projectile, simulations were performed using both an analytic and a tabular equation of state. The target assumed in these simulations was identical to that involved in the aforementioned experiments. In the target mesh 8 elements spanned the plate thickness, so that the resolution level was sufficient to estimate the diameter of the RCC perforations, but not the extent of the region of coating spall. Figure 5.5 shows simulation results for the diameters of the RCC perforations, as a function of projectile size, impact velocity, and projectile equation of state. In Figure 5.5, MG denotes the Mie-Gruneisen analytic equation of state, while SES denotes the SESAME tabular equation of state. The results of these simulations suggest the following conclusions, for the impact velocity range and impact obliquity considered:

- perforation diameters increase with both particle size and impact velocity, over the full range of the simulations,
- for a fixed particle size, perforation diameters increase with impact velocity at an approximately linear rate,
- for a fixed impact velocity, perforation diameters increase with particle size, but at a declining rate, and
- the simulation results are not sensitive to the choice of projectile equation of state.

Note that Figure 5.5 is not a ballistic limit plot; rather it plots perforation diameter versus impact velocity, so that the indicated trends are not unexpected.

Although the preceding results are informative, they consider only a limited rage of projectile size and obliquity. Hence the scaling of the simulation results, as compared to the available experimental data, is of considerable interest. Figure 5.6 shows a plot of perforation diameter versus normal impact momentum for the 11 different projectile size and impact velocity combinations modeled in the present computational study, as well as corresponding data for 15 published experiments [16][54]. The experiments involved projectile diameters ranging from 0.039 to 0.628 cm, impact velocities ranging from 2.49 to 7.32 km/s, and impact obliquities ranging from 0 to 80 degrees. The simulations involved a more limited range of projectile sizes (0.123 to 0.360 cm) and obliquities (30 to 45 degrees), but a much higher range of impact velocities (7 to 13 km/s). All of the simulations and experiments of course involved the same target configuration. The data in Figure 5.6 suggests that the experimental and the simulation results for the diameters of RCC perforations scale with normal impact momentum in a similar fashion. Although these results do not establish a general scaling relation for the problem of interest, they suggest that the momentum scaling observed in experiments below 8 km/s may be extrapolated to much of the velocity range of interest in orbital debris impact applications.

5.6 Conclusions

An anisotropic, rate dependent material model was formulated for use in the simulation of hypervelocity impact problems. The material model was developed to study orbital debris impact effects on reinforced carbon-carbon materials, and has been validated in simulations of hypervelocity impact experiments conducted at 7 km/s. The validated model was applied to simulate impacts at velocities beyond the experimental range. The results indicate that momentum scaling analysis, used to correlate a wide range of experiments below 8 km/s, has application in predicting perforation diameters for reinforced carbon-carbon targets at velocities as high as 13 km/s. The ability of reinforced carbon-carbon to retain its strength at high temperatures suggests that accurate strength models of this material are important in simulations of impact effects over the entire orbital debris velocity range.

Some conclusions relevant to future work are suggested:

- additional high resolution simulations are needed in order to investigate the spallation of silicon carbide coating at velocities above the current experimental range,
- additional mechanical properties testing is needed, at elevated temperatures and high strain rates, to support the development and validation of improved strength models for reinforced carbon-carbon,
- additional equation of state research is needed, to provide tabular data applicable to reinforced carbon-carbon materials over a wide range of impact velocities, and
- the development of advanced thermal protection materials should in the future include experimental work aimed at detailed characterization of their mechanical as well as their thermal properties.

Material property	Aluminum	Silicon Carbide	RCC
Reference bulk modulus, Mbar (Mpsi)	0.784 (11.4)	2.21 (32.1)	0.0576 (0.84)
Reference shear modulus, Mbar (Mpsi)	0.271 (3.93)	0.240 (3.48)	0.0718 (1.04)
Reference soundspeed, cm/μsec (in/μsec)	0.539 (0.212)	0.829 (0.326)	0.191 (0.075)
Mie-Gruneisen gamma	1.97	0.95	0.24
Mie-Gruneisen slope	1.34	1.21	1.33
Reference density, g/cm^3 (lb/ft^3)	2.70 (168.6)	3.21 (200.4)	1.58 (98.6)
Reference yield stress, kbar (Kpsi)	2.90 (42.1)	0.771 (11.2)	0.771 (11.2)
Specific heat, bar-cm^3/g-degree K (Btu/lb-degree F)	8.84 (0.211)	7.12 (0.17)	7.12 (0.17)
Strain hardening coefficient	125	10	2
Strain hardening exponent	0.1	1.0	1.0
Strain rate hardening coefficient	0.0	0.0	0.1
Strain rate hardening exponent	0.0	0.0	1.0
Reference strain rate, 1/sec	0	0	0.01
Thermal softening coefficient	0.567	0.0	-1.0
Melt temperature, degree K (degree F)	1,220 (1736.3)	3,840 (6452.3)	3,840 (6452.3)
Maximum compression	100	100	100
Plastic failure strain	1.00	0.10	0.50

Table 5.1: Material properties used in the simulations

Parameters	Silicon Carbide	Reinforced carbon-carbon
$\gamma_1 = \gamma_2 = \gamma_3$	10.0	1.00
$\mu_{11} = \mu_{22} = \mu_{33}$	0.1	1.00
μ_{13}	1.00	1.00
$\mu_{12} = \mu_{23}$	1.00	0.50
$\alpha_{11} = \alpha_{22} = \alpha_{33} = \alpha_{13}$	1.00	1.00
$\alpha_{12} = \alpha_{23}$	1.00	3.73
$\beta_{11} = \beta_{22} = \beta_{33}$	2.00	2.00
$\beta_{12} = \beta_{13} = \beta_{23}$	2.00	2.00

Table 5.2: Material model parameters

Test number	D (cm)	v (km/s)	ϕ (deg)	N_e	Equation of state	D_p (cm)	Error (%)	D_c (cm)	Error (%)
B1028	0.628	7.01	45	8	Mie Gruneisen	2.60	10.3	3.74	15.0
				8	SESAME 3715	2.65	8.6	3.60	18.2
				16	Mie Gruneisen	2.66	8.3	4.05	8.0
				24	Mie Gruneisen	2.67	7.9	4.08	7.3
B1040	0.478	6.96	30	8	Mie Gruneisen	2.12	3.6	2.95	21.3
				8	SESAME 3715	1.97	10.5	2.95	21.3
				16	Mie Gruneisen	2.00	10.0	3.38	9.9
				24	Mie Gruneisen	2.10	4.5	3.48	7.2

Table 5.3: Numerical results, simulation of NASA JSC experiments B1028 and B1040

Test number	N_e	Total particles (million)	Total elements (million)	Number of processors	Wall clock hours
B1028	8	0.078	0.036	16	14
	16	0.572	0.275	64	65
	24	1.857	0.905	64	340
B1040	8	0.078	0.036	32	5
	16	0.572	0.275	64	74
	24	1.856	0.905	64	347

Table 5.4: Computer resource requirements, simulations of NASA experiments

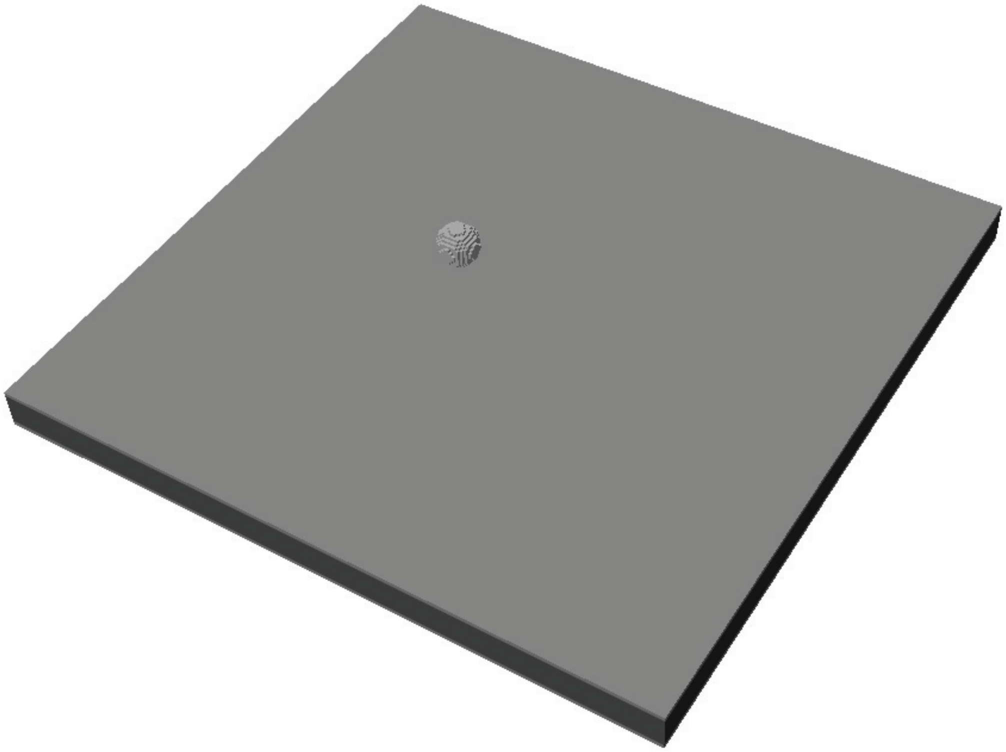

Figure 5.1: Initial configuration, simulation of NASA JSC experiment B1028

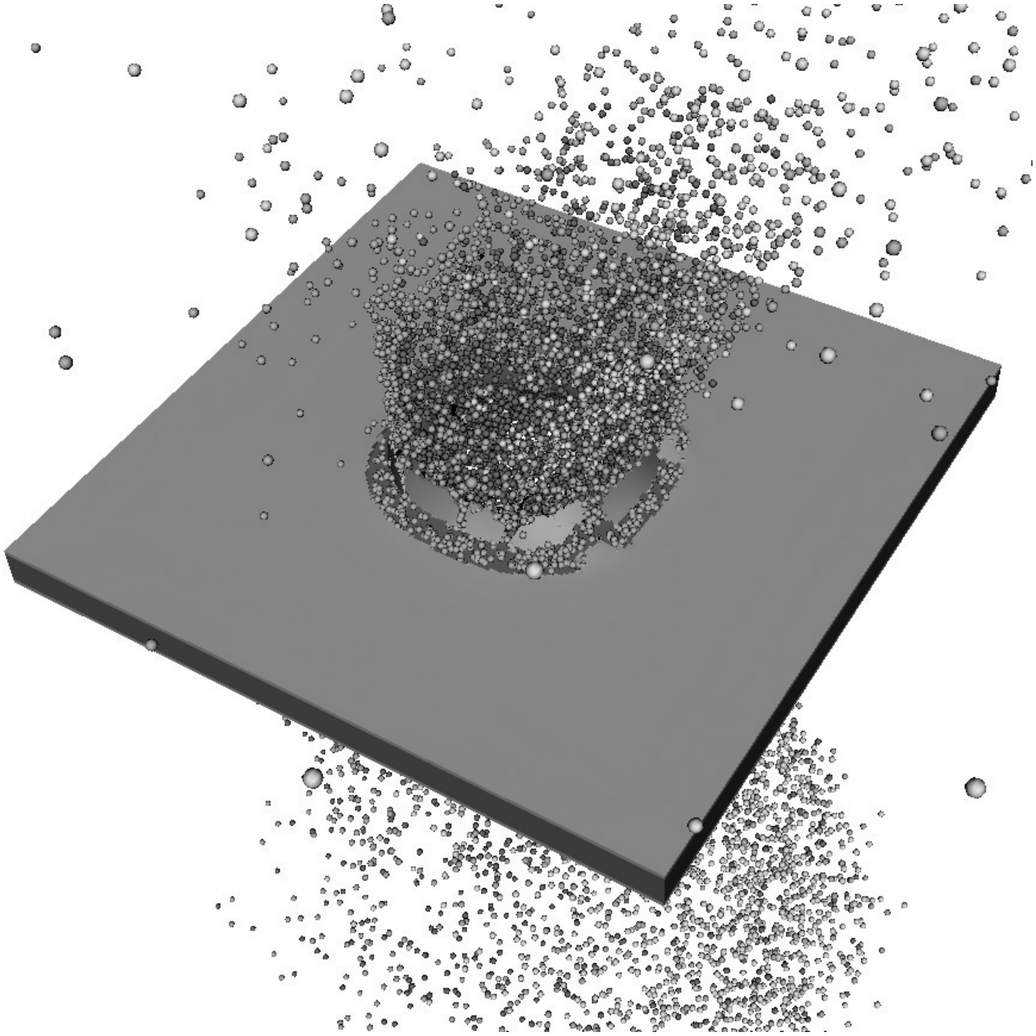

Figure 5.2: Particle-element plot of the simulation result at 50 microseconds after impact

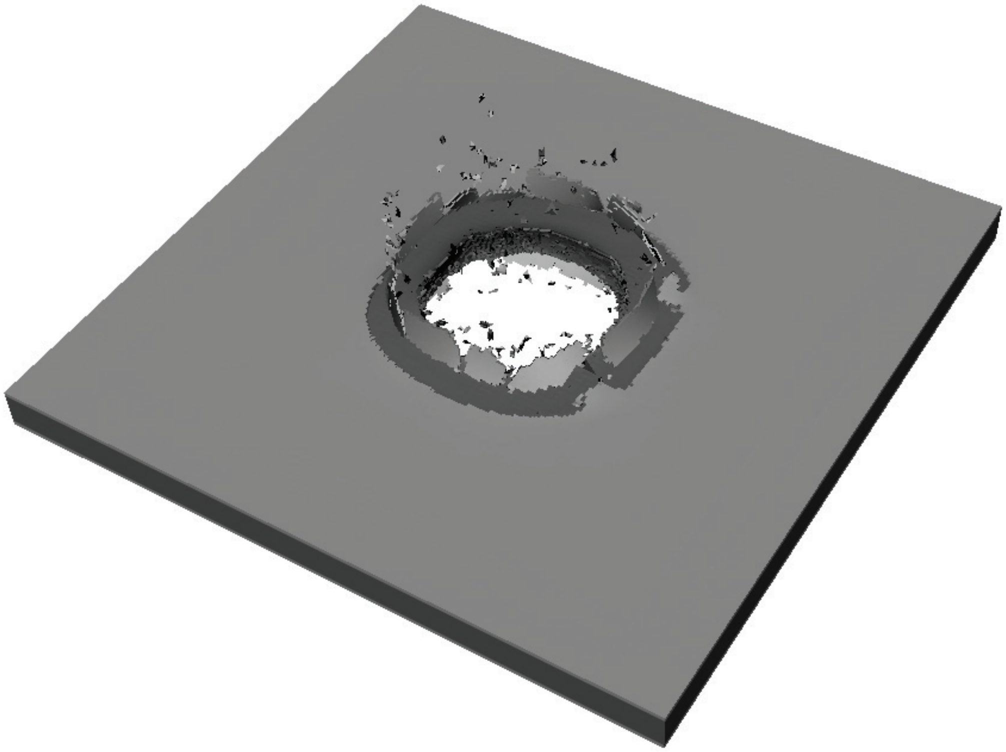

Figure 5.3: Element plot of the simulation result at 50 microseconds after impact

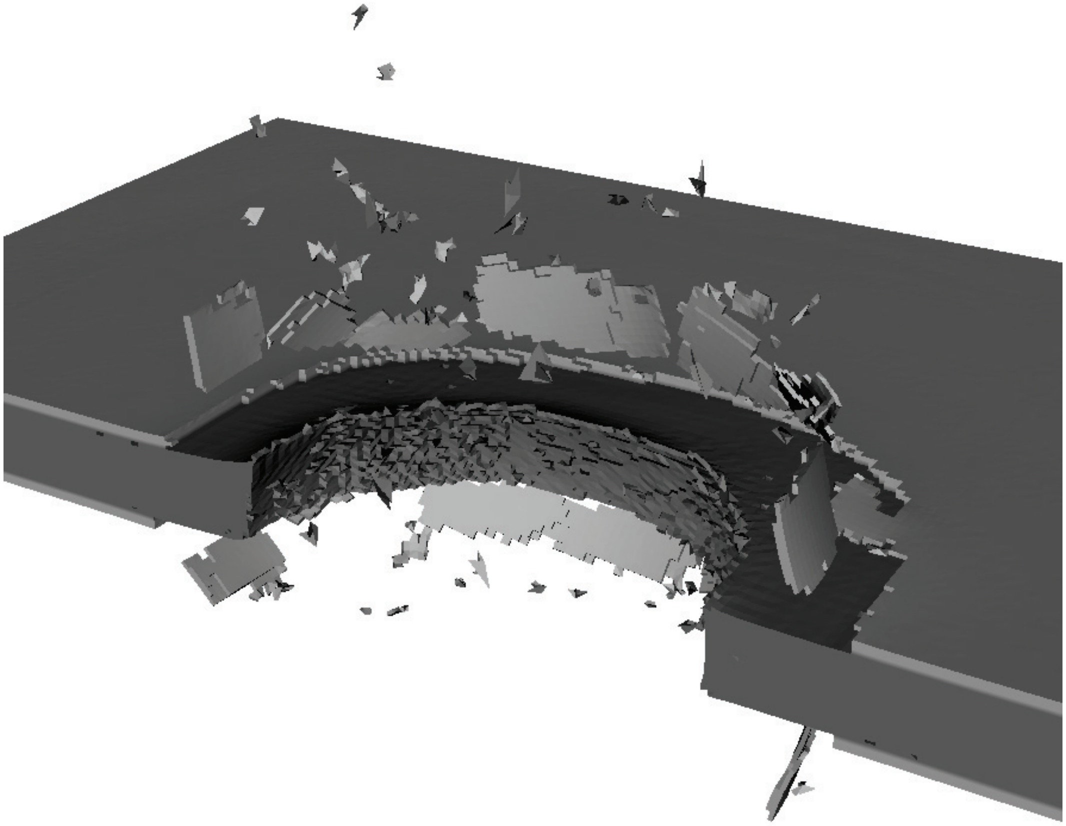

Figure 5.4: Sectioned element plot of the simulation results at 50 microseconds after impact

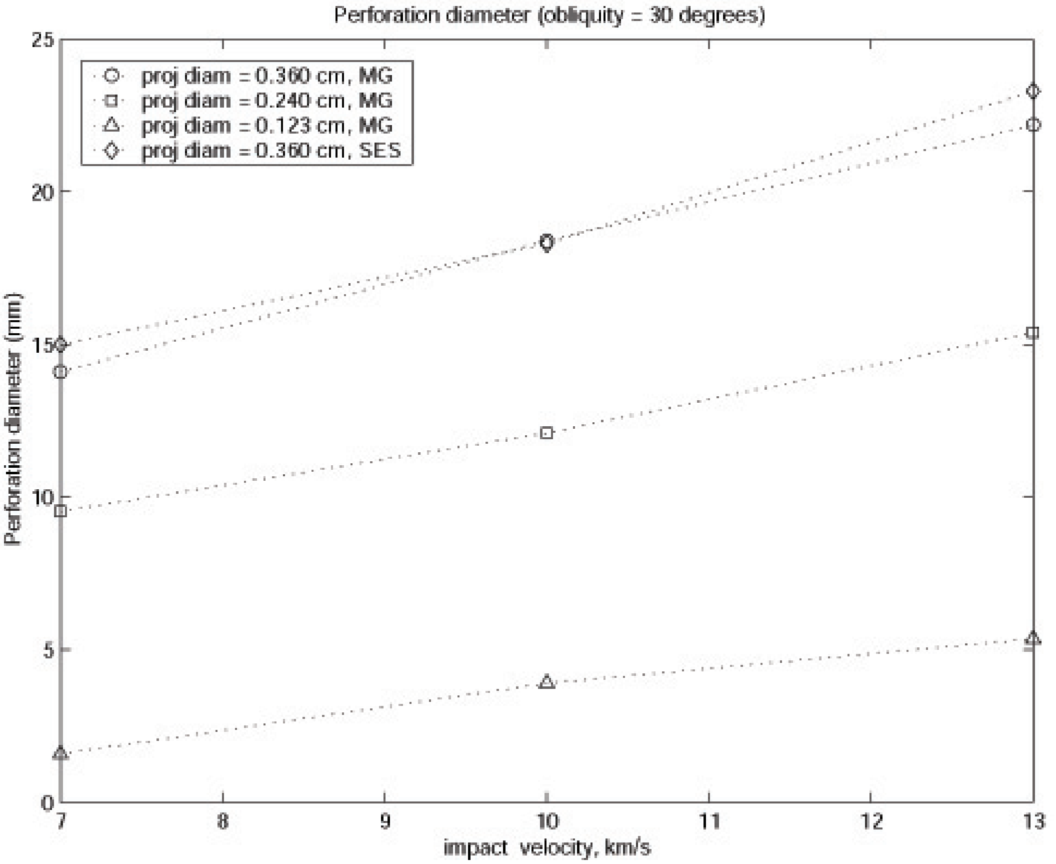

Figure 5.5: Simulation results for perforation diameter versus impact velocity

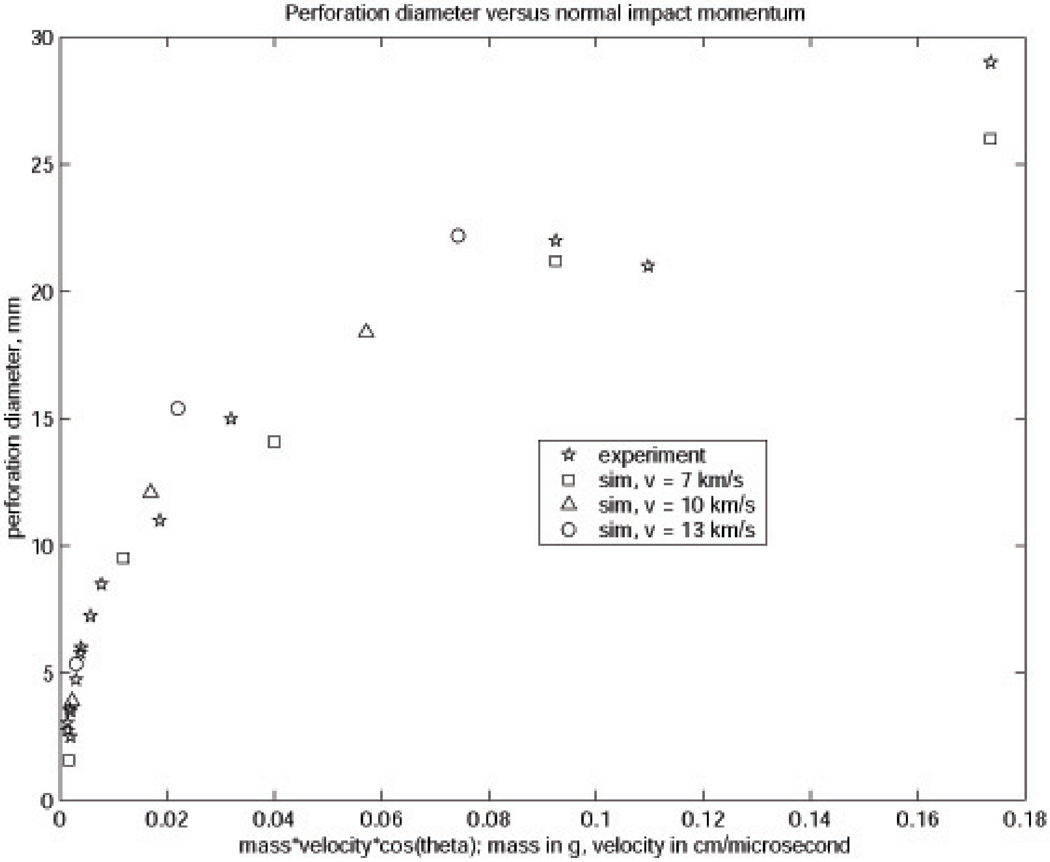

Figure 5.6: Perforation diameter versus normal impact momentum, for hypervelocity impact in reinforced carbon-carbon

Chapter 6

Conclusions

Overall conclusions of the dissertation and recommendations for future work are presented in this chapter.

In order to develop a more accurate and efficient numerical model to describe HVI phenomena, for three dimensional multi-plate metal-composite debris shield and thermal protection systems, the present work has developed a rate dependent anisotropic material model and a kernel free particle-finite element method.

In Chapter 2, a hybrid-finite element model and approximate material models for foam, tile, and RCC were used to simulate foam impacts on components of the space shuttle thermal protection system. The simulation results are in general consistent with experimental results available for this class of problems, and indicate that the numerical method used here is suitable for applications in a relatively low velocity regime.

In Chapter 3, a new rate dependent material model was formulated for use in the simulation of hypervelocity impact on aluminum-Nextel-Kevlar orbital debris shields. Simulation results show strain rate effects in composite materials are important in this hypervelocity impact problem.

In Chapter 4, an alternative kernel free particle-element method has been developed, to reduce computational costs, and avoid accuracy and stability problems associated with the selection of appropriate interpolation kernels widely used in particle methods and mixed particle-element methods. The method avoids the difficult task of formulating accurate and stable kernel functions for use in interpolating the density and quantifying contact-impact loads. Integration of the state equations derived here involves one loop over the particle neighbor sets, to calculate the particle interaction forces, instead of one loop each to determine the particle density and then the particle interaction forces. Application of the method is illustrated in three dimensional simulations which show good agreement with the results of published hypervelocity impact experiments.

In Chapter 5, a kernel free particle-finite element method and a new rate dependent anisotropic material model for Reinforced Carbon-Carbon are applied in the simulation of orbital debris impact effects. Simulation results showed that the material model can provide good estimates of Reinforced Carbon-Carbon perforation diameters and the extent of the spalled coating region, for oblique impacts at 7 km/s. This numerical model offers good accuracy, stability and low computational cost.

Some future work is suggested: (1) additional material modeling work describing the deformation and failure of advanced composite materials (foam, tile, felt, Reinforced Carbon-Carbon, Nextel, Kevlar, etc.) is needed, (2) additional high resolution simulations should be performed, to investigate the effects of any simplifying assumptions made in the areas of material modeling and structural geometry, (3) more efficient parallel numerical implementations should be developed, to reduce the rather high computational cost of three dimensional multi-plate shield impact simulations, (4) additional impact testing should be conducted, over a wider range of impact conditions, to validate proposed computational analysis techniques, and

(5) interface development work is needed to model any complex structural geometry described by a standard CAD data base or a commercial finite element preprocessor.

Bibliography

[1] Reinforced carbon-carbon (RCC) panels. Technical report, John F. Kennedy Space Center, 2004, FS-2004-01-001-KSC, NASA Facts.

[2] Report of the columbia accident investigation board, volume 1. Technical report, Government Printing Office, Washington, DC, August 2003.

[3] Technical report, 3M Corporation, web access via *http : //www.3m.com/ceramics/misc/tech_notebook.jhtml*, 2002.

[4] F. Abali, A. Pora, and K. Shivakumar. Modified short beam shear test for measurement of interlaminar sheear strength of composites. *Journal of Composite Materials*, 37:453–464, 2003.

[5] M.S. Aly-Hassan, H. Hatta, S. Wakayama, M. Watanabe, and K. Miyagawa. Comparison of 2D and 3D carbon/carbon composites with respect to damage and fracture resistance. *Carbon*, 41:1069–1078, 2003.

[6] K. Anand, V. Gupta, and D. Dartford. Failure mechanisms of laminated carbon-carbon composites - II. Under shear loads. *Materials and Design*, 42:797–809, 1994.

[7] R.P. Banas, D.E. Elgin, E.R. Cordia, K.N. Nickel, E.R. Gzowski, and L. Aguilar. Lessons learned from the development and manufacturing of ce-

ramic reusable surface insulation materials for the space shuttle orbiters. In *Shuttle Performance: Lessons Learned, NASA Conference Publication 2283*, pages 967–1008, 1983.

[8] Haim Baruh. *Analytical Dynamics.* McGraw Hill, 1999.

[9] T. Belytschko, Y. Krongauz, D. Organ, M. Fleming, and P. Krysl. Meshless methods: an overview and recent developments. *Computer Methods in Applied Mechanics and Engineering*, 139:3–47, 1996.

[10] D.J. Benson. Computational methods in lagrangian and eulerian hydrocodes. *Computer Methods in Applied Mechanics and Engineering*, 99:235–394, 1992.

[11] M.B. Boslough, J.A. Ang, W.D. Chhabildas, C.A. Reinhart, C.A. Hall, B.G. Cour-Palais, E.L. Christiansen, and J.L. Crews. Hypervelocity testing of advanced shielding concepts for spacecraft against impacts to 10 km/s. *International Journal of Impact Engineering*, 14:95–106, 1993.

[12] J.D. Buckley and D.D. Edie. *Carbon-Carbon Materials and Composites.* Noyes Publications, New Jersey, 1993.

[13] D.E Carroll, E.S Hertel, and T.G. Trucano. Simulation of armor penetration by tungsten rods: ALEGRA validation report. Technical report, Sandia National Laboratories, SAND97-2765, 1997.

[14] J.K. Chen, F.A. Allahdadi, and T.C. Carney. High-velocity impact of Graphite/Epoxy composite laminates. *Composite Science and Technology*, 57:1369–1379, 1997.

[15] E.L. Christiansen, J.L. Crews, J.H. Williamsen, J.H. Robinson, and A.M. Nolen. Enhanced meteoroid and orbital debris shielding. *International Journal of Impact Engineering*, 17:217–228, 1995.

[16] E.L. Christiansen and L. Friesen. Penetration equations for thermal protection materials. *International Journal of Impact Engineering*, 20:153–164, 1997.

[17] E.L. Christiansen and J.H. Kerr. Projectile shape effects on shielding performance at 7 km/s and 11 km/s. *International Journal of Impact Engineering*, 20:165–172, 1997.

[18] P.A. Cooper and J.W. Sawyer. Life considerations of the shuttle orbiter densified-tile. In *Shuttle Performance: Lessons Learned, NASA Conference Publication 2283*, pages 1009–1024, 1983.

[19] DuPont Corporation. Technical guide for nomex brand fiber. Technical report, H-52720, 2001.

[20] D.Crawford and B. Dodson. Computational analysis of foam impact damage on shuttle thermal protection system materials using CTH. In *2004 AIAA Aerospace Sciences Meeting*, AIAA-2004-0941, Reno, Nevada, USA, January 5-8,2004.

[21] R. Destefanis and M. Faraud. Testing of advanced materials for high resistance debris shielding. *International Journal of Impact Engineering*, 20:209–222, 1997.

[22] K.J. Dowding, J.V. Beck, and B.F. Blackwell. Estimation of directional-dependent thermal properties in a carbon-carbon composite. *International Journal of Heat Mass Transfer*, 39:3157–3164, 1996.

[23] C.E. Anderson Jr. ed. Proceedings of the 2003 hypervelocity impact symposium. In *International Journal of Impact Engineering*, 29: No. 1-10, 2003.

[24] E.P. Fahrenthold. A continuum damage model for fracture of brittle solids under dynamic loading. *Journal of Applied Mechanics*, 58:904–909, 1991.

[25] E.P. Fahrenthold. Numerical simulation of impact on hypervelocity shielding. In *Proceedings of the Hypervelocity Shielding Workshop*, pages 47–50, Galveston, Texas, 1998.

[26] E.P. Fahrenthold. User's guide for EXOS. Technical report, University of Texas, Austin, Texas, 2003.

[27] E.P. Fahrenthold and B.A. Horban. Thermodynamics of continuum damage and fragmentation models for hypervelocity impact. *International Journal of Impact Engineering*, 20:241–252, 1997.

[28] E.P. Fahrenthold and B.A. Horban. A hybrid particle-finite element method for hypervelocity impact simulation. *International Journal of Impact Engineering*, 23:237–248, 1999.

[29] E.P. Fahrenthold and B.A. Horban. An improved hybrid particle-element method for hypervelocity impact simulation. *International Journal of Impact Engineering*, 26:169–178, 2001.

[30] E.P. Fahrenthold and Young-Keun Park. Simulation of hypervelocity impact on aluminum-Nextel-Kevlar orbital debris shields. *International Journal of Impact Engineering*, 29:227–235, 2003.

[31] E.P. Fahrenthold and R. Shivarama. Orbital debris impact simulation using a parallel hybrid particle-element code. *International Journal of Impact Engineering*, 26:179–188, 2001.

[32] E.P. Fahrenthold and R. Shivarama. Extension and validation of a hybrid particle-finite element method for hypervelocity impact simulation. *International Journal of Impact Engineering*, 29:237–246, 2003.

[33] E. Fitzer and L.M. Manocha. *Carbon Reinforcements and Carbon/Carbon Composites*. Springer-Verlag, Berlin, Heidelberg, New York, 1998.

[34] G. Gisler, R. Weaver, M. Gittings, and C. Mader. Two and three dimensional asteroid ocean impact simulations. *International Journal of Impact Engineering*, 29:283–292, 2003.

[35] D.J. Grosch. Inhibited shaped charge launcher testing of spacecraft shield designs. Technical report, Southwest Research Institute, San Antonio, TX, April 1997.

[36] K.W. Gwinn and K.E. Metzinger. Analysis of foam impact onto the columbia shuttle wing leading edge panels using Pronto3D/SPH. In *2004 AIAA Aerospace Sciences Meeting*, AIAA-2004-0942, Reno, Nevada, USA, January 5-8,2004.

[37] J.O. Hallquist. Theoretical manual for DYNA3D. Technical report, Lawrence Livermore National Laboratory, Livermore, California, 1983.

[38] C.J. Hayhurst, S.J. Hiermier, R.A. Clegg, W. Riedel, and M. Lambert. Development of material models for Nextel and Kevlar-Epoxy for high pressures and strain rates. *International journal of Impact Engineering*, 23:365–376, 1999.

[39] C.J. Hayhurst, I.H.G. Livingstone, R.A. Clegg, R. Destefanis, and M. Faraud. Ballistic limit evaluation of advanced shielding using numerical simulations. *International Journal of Impact Engineering*, 26:309–320, 2001.

[40] E.S. Hertel. A comparison of the CTH hydrodynamics code with experimental data. Technical report, Sandia National Laboratories, SAND92-1879, 1992.

[41] S.J. Hiermaier, W. Riedel, C.J. Hayhurst, R.A. Clegg, and C.M. Wentzel. Advanced material models for hypervelocity impact simulations. Technical report, ESTEC Contract 12400/97/NL/PA(SC) Final Report, July, 1999.

[42] R. Hill. *The mathematical theory of plasticity.* Oxford, 1956.

[43] G.R. Johnson, E.H. Petersen, and R.A. Stryk. Incorporation of an SPH option into the EPIC code for a wide range of high velocity impact computations. *International Journal of Impact Engineering*, 14:385–394, 1993.

[44] C.E. Anderson Jr. An overview of the theory of hydrocodes. *International Journal of Impact Engineering*, 5:33–59, 1987.

[45] J.H. Kerr, D.J. Grosch, and E.L. Christiansen. Impact testing of large foam projectiles. In *2004 AIAA Aerospace Sciences Meeting*, AIAA-2004-0939, Reno, Nevada, USA, January 5-8,2004.

[46] M.D. Knudson, C.A. Hall, R. Lemke, C. Deeney, and J.R. Asay. High velocity flyer plate launch capability on the sandia Z accelerator. *International Journal of Impact Engineering*, 29:377–384, 2003.

[47] E. Lara-Curzio, D. Bowers, and M.K. Ferber. The interlaminar tensile and shear behavior of a unidirectional C-C composite. *Journal of Nuclear Materials*, 230:226–232, 1996.

[48] M. Lee and Y.H. Yoo. Assessment of a new dynamic FE-code: application to the impact of a yawed-rod onto nonstationary oblique plate. *International Journal of Impact Engineering*, 29:425–436, 2003.

[49] L.D. Libersky, P.W. Randles, T.C. Carney, and D.L. Dickinson. Recent improvements in SPH modeling of hypervelocity impact. *International Journal of Impact Engineering*, 20:525–532, 1997.

[50] E. Liden, J. Ottosson, and L. Holmberg. WHA rods penetrating stationary and moving oblique steel plates. In *Proceedings of the 16th International Symposium on Ballistics*, pages 711–719, 1996.

[51] W.-Y. Lu, B.R. Antoun, J.S. Korellis, S. Scheffel, M.Y. Lee, R.D. Hardy, and L.S. Costin. Material characterization of shuttle thermal protection system for impact analyses. In *2004 AIAA Aerospace Sciences Meeting*, AIAA-2004-0945, Reno, Nevada, USA, January 5-8,2004.

[52] J. Lubliner. *Plasticity Theory.* Macmillan, 1990.

[53] S.P. Lyon, J.D. Johnson, and editors. SESAME: The Los Alamos National Laboratory equation of state database. Technical report, Los Alamos National Laboratory, LA-UR-92-3407.

[54] F. Lyons, E.L. Christiansen, and J.H. Kerr. Hypervelocity impact testing of Reinforced Carbon-Carbon composites. Technical report, JSC 23898, NASA Johnson Space Center, May 1998.

[55] L.E. Malvern. *Introduction to the Mechanics of a Continuous Medium.* Prentice Hall, Englewood Cliffs, New Jersey, 1969.

[56] J.M. McGlaun, S.L. Thompson, and M.G. Elrick. CTH: A three dimensional shock wave physics code. *International Journal of Impact Engineering*, 10:351–360, 1990.

[57] D.F. Medina and J.K.Chen. Three-dimensional simulations of impact induced damage in composite structures using the parallelized SPH method. *Composites: Part A*, 31:853–860, 2000.

[58] M. Melis, K. Carney, M. Pereira, D. Revilock, and P. Kopfinger. Characterization of BX- 250 ET foam behavior under impact in a 1 psi environment.

In *2004 AIAA Aerospace Sciences Meeting*, AIAA-2004-0943, Reno, Nevada, USA, January 5-8,2004.

[59] D.E. Myers, C.J. Martin, and M.L. Blosser. Parametric weight comparison of advanced metallic, ceramic tile, and ceramic blanket thermal protection systems. Technical report, NASA TM 2000-210289, 2000.

[60] W.F. Noh. Errors for calculations of strong shocks using an artificial viscosity and an artificial heat flux. *Journal of Computational Physics*, 72:78–120, 1978.

[61] G. Oertel. *Polyurethane Handbook*. Hanser/Gardner, New York, 1994.

[62] C.W. Ohlhorst, W.J. Vaughn, P.O. Ransone, and H.T. Tsou. Thermal conductivity database of various structural carbon-carbon composite materials. Technical report, NASA TM 1997-4787, 1997.

[63] J.M. Owen, J.V. Villumsen, P.R. Shapiro, and H. Martel. Adaptive smoothed particle hydrodynamics with application to cosmology: methodology II. *The Astrophysical Journal Supplement Series*, 116:155–209, 1998.

[64] D. Palmieri. ATV pressure module MDPS: Determination of ballistic limit through numerical simulation. Technical report, European Space Agency Report, EWP-2167.

[65] C.G. Papakonstantinou, P. Balaguru, and R.E. Lyon. Comparative study of high temperature composites. *Composites: Part B*, 32:637–649, 2001.

[66] P.W. Randles and L.D. Libersky. Smoothed Particle Hydrodynamics : Some recent improvements and applications. *Computational Methods in Applied Mechanics and Engineering*, 139:375–408, 1996.

[67] D.C. Rapaport. Molecular dynamics simulation using quaternions. *Journal of Computational Physics*, 41:306–314, 1985.

[68] G. Savage. *Carbon-Carbon Composites*. Chapman and Hall, London, 1993.

[69] J.W. Sawyer. Mechanical properties of the shuttle orbiter thermal protection system strain isolator pad. AIAA-1982-0789, 1982.

[70] D.L. Schmidt, K.E. Davidson, and L.S. Theibert. Unique applications of carbon-carbon composite materials (Part one). *SAMPE Journal*, 35:27–39, 1999.

[71] W.P. Schonberg. Protecting spacecraft against orbital debris impact damage using composite materials. *Composites : Part A*, 31:869–878, 2000.

[72] P.R Shapiro, H. Martel, J.V. Villumsen, and J.M. Owen. Adaptive smoothed particle hydrodynamics with application to cosmology: methodology. *The Astrophysical Journal Supplement Series*, 103:269–330, 1996.

[73] K. Shintate and H. Sekine. Numerical simulation of hypervelocity impacts of a projectile on laminated composite plate targets by means of improved SPH method. *Composites: Part A*, 35:683–692, 2004.

[74] R. Shivarama and E.P. Fahrenthold. An ellipsoidal particle-finite element method for hypervelocity impact simulation. *International Journal for Numerical Methods in Engineering*, 59:737–753, 2004.

[75] S.A. Silling. CTH reference manual: Johnson-holmquist ceramic model. Technical report, Sandia National Laboratories, 1992, SAND92-0576.

[76] D.J. Steinberg. Equation of state and strength properties of selected materials. Technical report, Lawrence Livermore National Laboratory, UCRL-MA-106439, 1996.

[77] R.F. Stellingwerf, J.H. Robinson, S. Richardson, S.W. Evans, R. Stallworth, and M. Hovater. Foam-on-tile impact modeling for the STS-107 investigation. In *2004 AIAA Aerospace Sciences Meeting*, AIAA-2004-0938, Reno, Nevada, USA, January 5-8,2004.

[78] R.F. Stellingwerf and C.A. Wingate. Impact modeling with smooth particle hydrodynamics. *International Journal of Impact Engineering*, 14:707–718, 1993.

[79] B.K. Wallin, C. Tong, A.L. Nichols, and E.T. Chow. Large multiphysics simulations in ALE3D. In *the Tenth SIAM Conference on Parallel Processing for Scientific Computing*, Portsmouth, Virginia, March 12-14, 2001.

[80] Y. Wang and Y. Xia. The effects of strain rate on the mechanical behavior of kevlar fibre bundles: An experimental and theoretical study. *Composites Part A*, 29a:1411–1415, 1998.

[81] Y. Wang and Y.M. Xia. Experimental and theoretical study on the strain rate and temperature dependence of mechanical behavior of kevlar fibre. *Composites Part A*, 30:1251–1257, 1999.

[82] T. Windhorst and G. Blount. Carbon-carbon composites: a summary of recent developments and applications. *Materials and Design*, 18:11–15, 1997.

[83] H.H. Yang. *Kevlar Aramid Fiber*. John Wiley and Sons Ltd., 1993.

[84] J.D. Yatteau, G.W. Recht, and K.T. Edquits. Transverse loading and response of long rod penetrators during high velocity plate perforation. *International Journal of Impact Engineering*, 23:967–980, 1999.

[85] J.A Zukas, T. Nicholas, H. Swift, L.B. Greszczuk, and D.R. Curran. *Impact Dynamics.* John Wiley and Sons Ltd., 1982.

Vita

Young-Keun Park was born in Seoul, Korea, on September 7, 1970, the first of two children of Bum-Ho Park and Ok-Young Lee. He completed his high school education in 1989, at Kwang-sung High school, Seoul, Korea. He entered Hong-Ik University from where he graduated with a Bachelor of Engineering in Mechanical Engineering in 1994. He fulfilled obligatory Korean military service as a ROTC officer from March 1994 to June 1996. He then entered the Graduate School of Hong-Ik University where he graduated with a Master of Science in 1998. He then joined doctoral program at the University of Texas at Austin in 1999 to continue his studies in Mechanical Engineering. Throughout the program, he worked as a research assistant for Dr. Eric P. Fahrenthold in the department of Mechanical Engineering. He received the Alex Charters Student Scholarship and Continuing University Tuition Scholarship for his scholastic accomplishments. He is married to Sungsoo Lee on July 21, 2001 and he is going to be a father in December, 2004.

Permanent Address: 1074 Ilsan, Hugok,
Imkwang Apt. #1004-101,
Koyang, Kyung-gi, Korea

This dissertation was typeset with LaTeX 2_ε[1] by the author.

---

[1] LaTeX 2_ε is an extension of LaTeX. LaTeX is a collection of macros for TeX. TeX is a trademark of the American Mathematical Society.